DUBLIN CITY UNIVERSITY

Physico-chemical Characterisation of Hydrogels

From Chemistry to Function

Bing Wu

August 2016

A DISSERTATION SUBMITTED TO
THE SCHOOL OF CHEMICAL SCIENCES
IN PARTIAL FULFILLMENT OF THE REQUIREMENTS
FOR THE DEGREE OF
DOCTOR OF PHILOSOPHY

Supervisor: **Prof. Dr. Dermot F. Brougham (UCD)**
Co-supervisor: **Dr. Kieran Nolan (DCU)**
Prof. Dr. Andreas Heise (RCSI)

Declaration

I hereby certify that this material, which I now submit for assessment on the programme of study leading to the award of PhD is entirely my own work, and that I have exercised reasonable care to ensure that the work is original, and does not to the best of my knowledge breach any law of copyright, and has not been taken from the work of others save and to the extent that such work has been cited and acknowledged within the text of my work.

Signed:

Date:

Bing Wu

PhD Candidate (Dublin City University)

Acknowledgements

Frist of all I would like to express my great thanks to my supervisors: Prof. Dr. Dermot F. Brougham (University College Dublin), Dr. Victor M. Litvinov (DSM Resolve), Prof. Andreas Heise (Royal College of Surgeons in Ireland), Dr. Aylvin A. Dias (DSM AHEAD), for the guidance they offered me through the whole PhD, and for all the encouragement and positive attitude they taught me towards scientific life. Specially, I want to thank Prof. Dr. Brougham and Dr. Litvinov for always having open mind when discussing studies with me, and providing me many valuable advices, in sciences as well as in life, from which I will benefit throughout my entire life and career. I am also grateful to Dr. Kieran Nolan, who took over the role as my academic supervisor when some administrative changes occurred by the end of my PhD. Without his help on facilitating all the necessary paperwork, I could complete my PhD.

I also would like to thank DSM, Geleen, the Netherlands, for its financial support to my program, and also for providing me with their various facilities that allows me to work in this multinational corporation during my PhD, and let me have the first-hand experience on doing research in an industrial environment. Furthermore, I gratefully acknowledge the generous assistances I received from Dr. Christopher J. Duxbury (DSM AHEAD), Dr. Mengmeng Zong (DSM AHEAD) and Dr. Mithun Goswami (DSM Resolve) during my stay in DSM, all the interesting discussions we had helped me to build up my knowledge in the field of polymer chemistry and polymer physics.

As part of my PhD training, I spent considerable amount of time in other universities. Here, I sincerely thank Dr. Walter Chassé, Prof. Dr. Arno M. M. Kentgens of Dutch Solid State NMR Center in Radboud Universiteit Nijmegen, the Netherlands, for their great help on Ultra-high field DQ NMR analyses about the materials I used in my studies. I also would like to express my deep gratitude to Dr. Bart A. J. Noordover, Mr. Chunliang Li, Mr. Hao Liu, Mr. Yanwu Zhou in Technische Universiteit Eindhoven, the Netherlands, from whom I learned about how to perform mechanical analyses on polymeric materials.

Without the contribution from my collaborators, I could not finish all these wonderful studies. Hence, I also would like to show my gratitude to all the people involved in my work: Dr. Michael D. Mantle in University of Cambridge, UK (Chapter V), Dr. Klaus Zick in Bruker Biospin GmbH, Germany (Chapter V), Dr. Sivaramakrishnan Ramadurai and Dr. Tia Keyes in Dublin City University, Ireland (Chapter V), Dr. Meredith E. Wiseman, Dr. Micheal E. Seitz

and Dr. Katerina Tomić in DSM MSC, the Netherlands (Chapter VII), Dr. Ron Peters and Ton Brooijman in DSM Resin, the Netherlands (Chapter IV and Chapter VI), Dr. Mingwen Tian, Dr. Jianjun Xu and Dr. Junyu Li in DSM Resolve, the Netherlands (Morphological analyses of heterogeneity in UV-cured polyacrylate network, though this work was not included in this thesis)

Furthermore, I would like to thank everyone I have worked with during these past years of my PhD: Ms. Fadwa el Haddassi, Dr. Jose M. Hierrezuelo Osorio, Dr. Lionel Maurizi, Dr. Eoin K. Fox, Ms. Cara Moloney, Ms. Sarah Martin, Ms. Orla Carron, Ms. Patricia Monks, Mr. Kevin Behan in Prof. Dr. Brougham's group in University College Dublin, Ireland; Mr. Saltuk Hanay, Mr. Timo Stukenkemper, Dr. Tushar Borase, Dr. Zeliha Ates, Dr. Jin Huang, Dr. Hannah Prydderch. Mr. Fernando O. Salles, Ms. Shona O'Brien, Mr. Seamus Caulfield, Mr. Robert Murphy in Prof. Dr. Andreas Heise's group in Royal College of Surgeon in Ireland, Ireland; Dr. Harry Linssen, Dr. Ard Kolkman, Dr. Claudiu Melian, Ms. Monique Ensinck, Mr. Don Jansen in DSM Resolve, the Netherlands; Dr. Jun Qiu, Ms. Silvana P. Di. Silvestre, Mr. Marcel Houben in DSM AHEAD, the Netherlands.

I would like to thank European Union Framework-Programme-7-People Funding for supporting this Marie Curie EID program, and Dr. Owen Clarkin in Dublin City University for his financial support to me during the last period of my PhD period.

I owe further thanks for the technical support from Mr. John McLoughlin, Mr. Amborse May, Ms. Veronica Dobbyn, Mr. Vincent Hooper, Mr. Damien McGuirk, Ms. Catherine Keogh in Dublin City University.

Last but not least, I would like to give my deepest and sincerest thanks to my parents. Due to the busy schedule of my PhD program, I only went back to my hometown once in the past 4 years. Without their support, understanding and sacrifice, I could never become what I am. I want to thank them for believing in me when I doubt myself, pushing me forward when I want to give in, teaching me on how to find the purpose of my life. Because of them, I could stand still to face every difficulty in my life. I really owe everything to them!

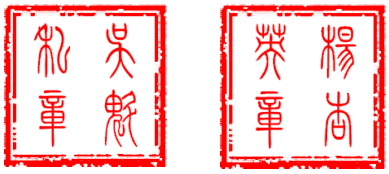

獻給我的父母

Dedicated to my parents

Table of Contents

List of Abbreviations

AIBN	2,2-azo-isobutyronitrile
AFM	atomic force microscopy
BABA (pulse sequence)	Back-to-Back
BACOEA	2-[[(butylamino)carbonyl]oxy]ethyl acrylate
CSA	chemical shift anisotropy
CPMAS	cross polarization magic angle spinning
DDV	drug delivery vehicle
DDS	drug delivery system
DMA (chemical)	dimethylacrylamide
DMA/DMTA (method)	dynamic mechanical thermal analysis
DMPA	2,2-dimethoxy-2-phenylacetophenone
DPTMBPO	diphenyl(2,4,6-trimethylbenzyol) phosphine oxide
DQ	double quantum
DSC	differential scanning calorimetry
EWC	equilibrium water content
FCS	fluorescence correlation spectroscopy
FTIR	Fourier transform Infrared spectroscopy
HA	hexyl acrylate
HBA	4-hydroxybutyl acrylate
HEA	2-hydroxyethyl acrylate
HEMA	hydroxyethylmethacrylate
HMPP	2-hydroxy-2-methylpropiophenone
HRMAS	high resolution magic angle spinning
Hy	hydrogel
IR NMR	inversion recovery NMR
LF NMR	low field NMR
MAS	magic angle spinning
mPDMS	methacryloxypropyl-PDMS-nBu
MQ	multiple quantum

NMR	nuclear magnetic resonances
NOE	nuclear Overhauser effect
PDMS	polydimethylsiloxane
PEG	polyethylene glycol
PEGDA	polyethylene glycol-diacrylate
PETM	pentaerythritol tetrakis(3-mercaptopropionate)
PFG	pulsed field gradients
PMMA	poly(methyl methacrylate)
PNIPAM	poly(N-isopropylacrylamide)
PTMSP	poly[1-(trimethylsilyl)-1-propyne]
RDC	residual dipolar coupling
SAXS	small-angle x-ray scattering
SANS	small-angle neutron scattering
SE/HE	spin echo/Hahn echo
SPE	single pulse excitation
SQ	single quantum
STE	stimulated echo
TEGDMA	triethylene glycol dimethacrylate
TGA	thermogravimetric analysis
TRIS	(3-methacryloxypropyl) tris(trimethylsiloxy) silane
UV	ultra-violet

List of Publication

PUBLICATIONS

"Nanometer Scale Analyses of Microheterogeneity in Polyacrylate Network" (under preparation)

"Spectroscopic Analyses of H-bonding Effect on Drug Diffusion inside Hydrogel Matrices", (under preparation)

"Effect of Hydrogen-bonding on Network Formation and Chain Dynamics in Polyacrylate Systems", (under preparation)

"Oxygen Permeability Study of Silicone-based Hydrogels", (under preparation)

"A Novel Injectable Biocompatible Self-Setting Glass-Alginate Hydrogel Composite for Soft Tissue Engineering Applications", ***Advanced Functional Material*** (submitted)

"Network Structure in Acrylate Systems: the Effect of Junction Topology, Crosslink Density and macroscopic gel properties", ***Macromolecules*** (Accepted)

"Gadolinium-loaded polychelating amphiphilic polymer as an enhanced MRI contrast agent for human multiple myeloma and non Hodgkin's lymphoma (human Burkitt's lymphoma)", ***RSC Adv.***, 2014, **4**, pp. 18007-18016

PRESENTATIONS

"Nanoscale Morphological Analyses of PEG-based Polyacrylate Gel", **EUROMAR 2016**, Aarhus, Denmark, *July 4th – 7th 2016*

"Analyses of H-bonding Effect on Drug Diffusion inside Crosslinked Hydrogel Network via NMR diffusometry", **57th Experimental Nuclear Magnetic Resonance Conference (ENC)**, Wyndham Grand Hotel, Pittsburgh, Pennsylvania, USA, *April 10th – 15th 2016*

"Effect of H-bonding on the Diffusion of Drug Analogue inside Crosslinked Hydrogel", **Practical Application of NMR in Industry Conference (PANIC) 2016**, Houston, Texas, USA, *February 15th – 18th 2016*

"Topological Analyses of UV-cured Polyacrylate Networks through a NMR Approach", **International Society of Magnetic Resonance Conference (ISMAR) 2015**, Shanghai, China, *August 16th – 21st 2015*

"^{1}H NMR Relaxation Analyses of UV-curd Acrylate Hydrogel Network", **56th Experimental Nuclear Magnetic Resonance Conference (ENC)**, Pacific Grove, California, USA, *April 19th – 24th 2015*

"^{1}H Nuclear Magnetic Relaxation Studies of the Water Dynamics inside Magnetic Hydrogels", **27th International Symposium on Polymer Analysis and Characterization (ISPAC)**, Les Diablerets, Switzerland, *June 16th – 18th 2014*

"Investigation into the Dynamics of Water inside Magnetic Hydrogels by ^{1}H Nuclear Magnetic Diffusion Studies", **55th Experimental Nuclear Magnetic Resonance Conference (ENC)**, Boston, Massachusetts, USA, *March 23rd – 28th 2014*

Title: Physico-chemical Characterisation of Hydrogels

Author: Bing Wu

Abstract

Hydrogels in industrial applications have received increased attention due to potential in drug eluting contact lenses and in the pharmaceutical field because of the anticipated biocompatibility of this class of materials. As one of most common commercial hydrogels, Polyethylene glycol (PEG)-based polyacrylate gels are widely used in tissue engineering and coating applications. In many cases photopolymerization is the preferred route to preparing these crosslinked networks. Hence, a thorough understanding of these photo-cured PEG-based polyacrylate network is of great interest in the further understanding of industrial applications of these materials.

In this work, we probed the detailed polymer dynamics inside these photo-cured networks by using a series of analytical tools, like Nuclear Magnetic Resonances (NMR) techniques, while these bulky characters (mechanic properties, thermal properties, etc.) were also measured correspondingly. By correlating these data, several effects caused by microscopic attributes (e.g. topological properties of the network, hydrogen bonding induced clustering, etc.) of these hydrogels on their macroscopic properties (elasticity, O_2 permeability, etc.) will be discussed in this thesis.

The goal of this thesis, is to better understand the connection between structural/dynamic properties of hydrogel materials and their mechanic/thermal behavior, which could be used to further design the new generation of hydrogel materials.

Chapter I

Introduction and Theoretical Background

1.1 Hydrogels

Hydrogels are polymer networks with excellent water absorbing properties. These hydrophilic three-dimensional networks can be created through chemical crosslinking or physical entanglement of polymer chains.[1] They are one of the most promising classes of polymer-based systems that embrace numerous current and potential biomedical and pharmaceutical applications. Their inherent property of biocompatibility makes them the outstanding candidate for drug delivery systems or tissue engineering scaffolds. Due to their hydrophilic, soft and rubbery nature, a minimal tissue irritation and low tendency of cells and proteins to adhere to the hydrogel surface could be expected in relevant applications of hydrogels.

Owing to the progress of polymer sciences, a gradual shift from natural hydrogels (e.g. agarose gel) towards synthetic hydrogels (e.g. polyhydroxyethylmethacrylate (pHEMA gel) could be observed in the polymer industry over the past two decades. These easy-modifiable synthetic hydrogels normally have long service life, high capacity of water absorption, and high gel strength, while they usually also have well-defined structures which can be further modified to yield tailorable degradability and functionality. Hence, numerous studies[2-6] have been focused on designing and characterizing the next-generation synthetic hydrogel materials.

1.1.1 Composition and Structure of Hydrogels

The basic component of hydrogel is its polymer network. As macromolecules constituting a large number of covalently bound repeating units, polymers can be spatially arranged in different ways. Due to their unique spatial arrangement, they can be further divided into linear polymers and branched polymers. Upon forming a hydrogel, branched polymer shows distinctive macroscopic properties (e.g. mechanical properties) compared to linear ones due to its three-dimensional feature, as demonstrated in several other studies[7, 8]. Several approaches are available to connect polymer chain in order to form network structure. All of these methods can be classified into two categories; physical and chemical gelation.[1]

'Reversible' or 'physical' gels are those hydrogels where molecular entanglements and/or secondary forces such as ionic, H-bonding or hydrophobic forces play the main role in forming the network. The whole gelation process in this case is reversible and it is possible to dissolve them by changing environmental conditions, such as pH, and ionic strength of solution or temperature.

The other type of hydrogels are called 'permanent' or 'chemical' gels in which the network of covalent bonds joining different macromolecular chains can be achieved by cross-linking polymers in the dry state or in solution. These gels may be charged or non-charged depending on the nature of functional groups present in their structures. The charged hydrogels usually exhibit changes in swelling upon variations in the external environment such as pH, and it is known that they can undergo changes in their geometry when exposed to an electric field.[9]

In this thesis, we will mainly focus on the physico-chemical characterization of industrially used chemically crosslinked hydrogels.

1.1.2 Hydrogel Crosslinking Reactions

Two common practices are often used in preparing chemical hydrogels: one is called 'three-dimensional polymerization', in which a hydrophilic monomer is polymerized in the presence of a polyfunctional cross-linking agent, the other is by direct cross-linking reaction between polymer chains. In industry, these hydrogels are usually synthesized by free-radical initiated polymerization. By adding free radical generating compounds such as benzoyl peroxide, 2,2-azo-isobutyronitrile (AIBN), and ammonium peroxodisulphate into the formulation, hydrogel network can be produced upon UV-, gamma-, or electron beam-radiation. Here we introduce the free radical polymerization mechanism and two conventional crosslinking reactions that are frequently used during industrial production of hydrogel materials.

1.1.2.1 Photo-initiated Free Radical Polymerization Mechanism

There are 3 reaction stages involved in the photo-initiated free radical polymerization.[10]

<u>Initiation:</u>

At the initiation stage, the photo-initiator splits up into two radical under the influence of UV radiation,

$$A - B + h\nu \longrightarrow A^* + B^*$$

These radicals then react with the monomer M in the formulation,

$$A^*, B^* + M \longrightarrow P_1^*$$

The initiation rate v_i depends on the radical yield per absorbed photon Φ and the number of photons absorbed per second, I_a, and could be calculated through,

$$v_i = \Phi I_a \tag{1.1}$$

Propagation:

In this stage, the radical P_1^* created in the initiation stage further react with other monomer, and results in a chain reaction,

$$P_n^* + M \longrightarrow P_{n+1}^*$$

In the chain propagation, the propagation rate could be determined as following,

$$v_p = \mathrm{k}_p[P_n^*][M] \tag{1.2}$$

Where $[M]$ is the monomer concentration, $[P_n^*]$ the concentration of polymeric radicals, and k_p the propagation rate constant.

Termination:

Chain termination occurs by combination or disproportionation of different polymer radicals.

$$P_n^* + P_m^* \longrightarrow P_{n+m}$$

The termination rate v_t is proportional to the square of the polymer radial concentration $[P_n^*]^2$, with k_t being the termination rate constant.

$$v_t = k_t[P_n^*]^2 \tag{1.3}$$

Other processes also could cause the termination of the chain propagation, for instance, inhibiting reaction.

Since the kinetics of the polymer reaction directly affect the topological and morphological properties of the final network structure, a comprehensive understanding of the kinetics about the interested polymer reaction system is necessary for interpreting the sophisticated topology of the network. Such activity would require detailed physico-chemical analysis of a series of partially

cured samples. That is beyond the scope of the current work; our focus will be on highly cured samples.

1.1.2.2 UV-initiated acrylate polymerization

As the most widely used UV curable free radical-initiated systems, acrylate monomers normally take the form of the general formula H_2C=CR-COOR'. The curing reaction of acrylates is typical of those for vinyl monomers. As illustrated in Figure 1.1, the UV-initiated polyacrylate polymerization follows the conventional free radical polymerization route described above.

The degree of curing is measured by the degree of double bond conversion. The best conversion rate could be achieved via the use of oligomers as crosslinker and monomers as reactive thinners. Polyacrylate materials have been industrially implemented into various applications from tissue-engineering to coatings.[11]

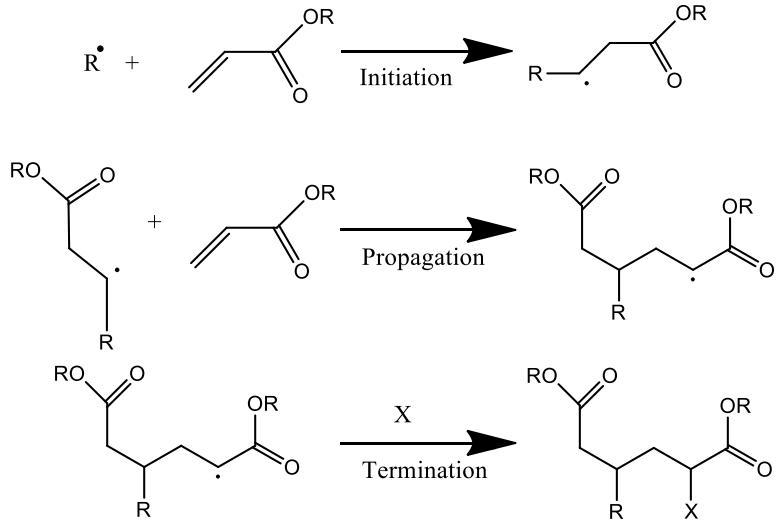

Figure 1.1 Scheme for free radical polyacrylate polymerization.

1.1.2.3 UV-initiated Thiol-ene Reaction

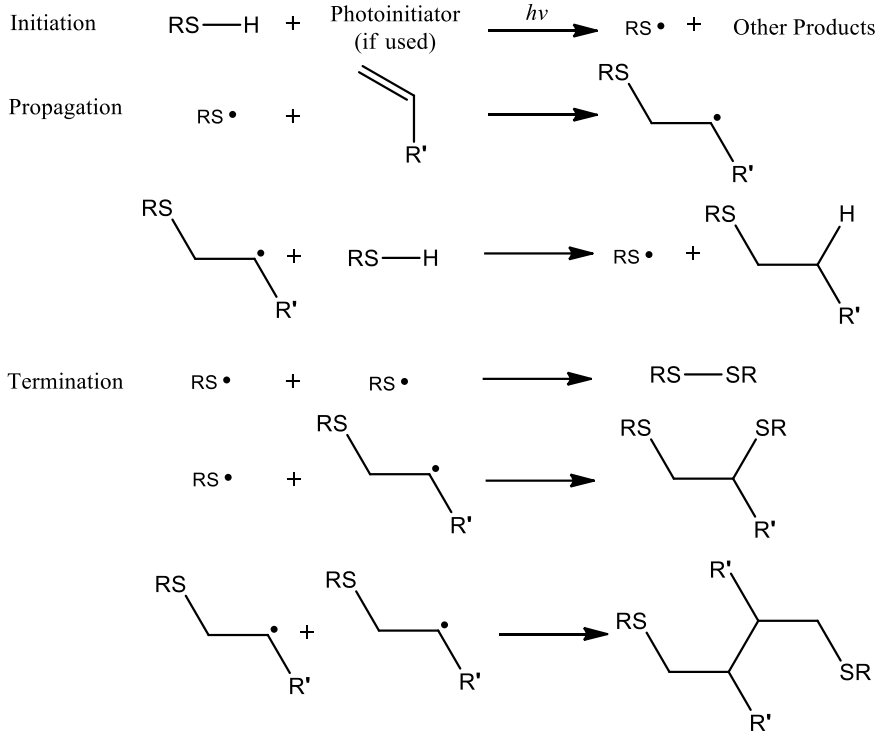

Figure 1.2 Scheme for thiol-ene reaction

Discovered first in 1905[12], the thiol-ene reaction is a photo-initiated reaction between a thiol and an alkene (see Figure 1.2). The advantage of thiol-ene type reactions are high efficiency, high yield in the presence of oxygen, and tolerance of various solvents and functional groups. Since the inception of thiol-ene chemistry, this reaction has been extensively used in different applications[13, 14] again including in coatings, and adhesive technologies. This reaction also follows the free radical polymerization mechanism.

1.1.3 Swelling Properties of Hydrogels

Due to their polymer networks backbone, hydrogels are water insoluble structures. However they are able to swell in water and absorb a large amount of water. The swelling properties of hydrogels depend on many different factors. Three most important parameters for structural characterization of swollen gels are the swelling factor (Q), average molecular weight between crosslinks and permanent entanglement (M_{c+e}) and network mesh-size (ξ). The swelling factor represents the ratio of the volume of swollen gel (V_s) and the polymer volume (V_p). It also equals to the reciprocal of the polymer volume fraction in the swollen gel (v_{2s}):

$$Q = \frac{V_s}{V_p} = \frac{1}{\upsilon_{2s}} \tag{1.4}$$

Highly crosslinked networks have smaller swelling factors than loosely crosslinked networks when same type of crosslink used in the crosslinking reaction.

M_{c+e} represents the molecular weight of polymer chains between neighboring junctions or persistent entanglements. The network mesh or pore size ξ determines the average distance between cross-links points in the gel and thereby, the degree of gel porosity. With respect to their mesh-size, hydrogels can be divided into macroporous, microporous or nonporous gels. The higher the crosslink density, the smaller M_{c+e} and mesh-size should be. The swelling factor can be determined experimentally by swelling measurements and allows the estimation of M_{c+e} and mesh-size.

Because water acts as a plasticizer in the hydrophilic polymer network system, the swelling process of the hydrogel can be considered under rubbery state. According to the Flory-Rehner theory[15, 16] absorption of the solvent by the network leads to the stretching of chains between junctions. The chains will take less probable configurations, which leads to decrease of total entropy. At the same time an increase of entropy occurs due to mixing of solvent with polymer. The Gibbs energy change of a system (ΔG_{system}) can be defined as the sum of two contributions[16]: Gibbs energy of mixing (ΔG_{mix}) and the elastic Gibbs energy ($\Delta G_{elastic}$):

$$\Delta G_{system} = \Delta G_{mix} + \Delta G_{elastic} \tag{1.5}$$

At the beginning of swelling process, the $\Delta G_{mix} \ll 0$, $\Delta G_{elastic} > 0$, $\Delta G_{mix} + \Delta G_{elastic} < 0$, so the swelling is favored and the solvent diffuses into the network. However, with the increase of both ΔG_{mix} and $\Delta G_{elastic}$ during the swelling process, ΔG_{system} would reach an equilibrium point ($\Delta G_{system} = 0$) where $|\Delta G_{mix}| = |\Delta G_{elastic}|$, so that the driving force for swelling is gone; equilibrium swelling is reached and further spontaneous swelling ceases.

1.1.4 Mechanical Properties of Hydrogels

The mechanical behavior of hydrogels is best understood using the theories of rubber elasticity and viscoelasticity. These theories are based on time-independent and time-dependent recovery of

the chain orientation and structure, respectively. By using theories to describe the mechanical behavior, it is possible to analyze the polymer structure and determine the effective M_{c+e} value as well as to elucidate information about the number of elastically active chains and about cyclization versus crosslinking tendencies. It is also possible, and sometimes necessary, to use theories to extrapolate mechanical properties to conditions in which the material may be used, as it may not always be possible to test the hydrogel under the exact application conditions. For these applications, it is of particular importance to use theories to extrapolate properties to the relevant conditions.

1.2 Nuclear Magnetic Resonance

Nuclear Magnetic Resonance, NMR, is a powerful analytical method used in characterizing molecular structure. Along with Mass Spectrometry, NMR has been broadly considered as the ultimate analytical tool by most chemists. Basically, NMR exploits the different behavior of nuclei in the presence of a magnetic field that is caused by the different chemical environment every individual nucleus experienced. Hence, to understand NMR, it is necessary to introduce spin theory.

1.2.1 Fundamental Theory

1.2.1.1 Nuclear Spins

According to quantum mechanics, neutrons and protons, which composes the atomic nucleus, are spin-1/2 particles, so the overall spin quantum number for a certain type of nucleus is the sum of a proper combination of these subatomic particles' nuclear spin quantum number.

Except for those nuclear isotopes with both an even number of protons and neutrons, every nucleus has a non-zero total nuclear spin quantum number, which is associated with a nuclear spin angular moment, and the relationship between them could be expressed as,

$$\|\boldsymbol{I}\| = [I \cdot I]^{1/2} = \sqrt{I(I+1)}\hbar \tag{1.6}$$

Where $\boldsymbol{I}$ is the nuclear spin angular moment, I is nuclear spin quantum number, and $\hbar$ is $h/2\pi$. Since nuclear magnetic moment $\boldsymbol{\mu_I}$ could be written as $\boldsymbol{\mu_I} = \gamma \boldsymbol{I}$ (for deduction see section 1.2.1.2), so $\boldsymbol{\mu_I}$ could be written as,

$$\|\boldsymbol{\mu_I}\| = \gamma\sqrt{I(I+1)}\hbar \tag{1.7}$$

Hence, the magnetic moment of a given nucleus is quantized, and directly related to the spin quantum number of that nucleus. Considering $\boldsymbol{\mu_I}$ and $\boldsymbol{I}$ are both vectors (though they are operators by definition), the quantization of a vector means both its magnitude and direction are quantized, therefore, a projection quantum number, m_I, the magnetic quantum number is created to manifest this. This can take values from $+I$ to $-I$ with an integer increment, so for a certain nucleus, $2I + 1$ values could be obtained for m_I. The magnetic quantum number is directly related the z-component of $\boldsymbol{\mu_I}$ and $\boldsymbol{I}$ (since due to the restrictions of quantum mechanics, only one of the three

Cartesian components of $\boldsymbol{I}$ can be specified simultaneously with $\boldsymbol{I}^2 = \boldsymbol{I} \cdot \boldsymbol{I}$), and could be used to calculate them through,

$$\|\boldsymbol{\mu}_{Iz}\| = \gamma \|\boldsymbol{I}_z\| = \gamma m_I \hbar \tag{1.8}$$

1.2.1.2 Zeeman Effect

Normally, energy states with different magnetic quantum numbers are degenerate, however, if the nucleus in question is placed inside a magnetic field, these energy states will split due to the Zeeman Effect. NMR exploits the Zeeman Effect inside the magnetic field which makes the energy difference between different *m* states detectable through radiofrequency transfer.

For a normal nucleus, its total Hamiltonian in a magnetic field could be expressed as,

$$H = H_0 + V_m \tag{1.9}$$

where H_0 is the unperturbed Hamiltonian of the atom, and V_m is perturbation caused by the presence of the magnetic field. The latter term in the strong magnetic field could be further split into (assuming no coupling between $\boldsymbol{\mu}_I$ and $\boldsymbol{\mu}_J$(the total magnetic moment of electrons and orbitals):

$$V_m = -\boldsymbol{\mu} \cdot \boldsymbol{B} = -\left(\boldsymbol{\mu}_I + \boldsymbol{\mu}_J\right)\boldsymbol{B} \tag{1.10}$$

Since NMR only probes the energy resonance between hyperfine structure sublevels, which has an extremely low energy difference due to $\boldsymbol{\mu}_I \ll \boldsymbol{\mu}_J$, hence, only the energy difference generated by $\boldsymbol{\mu}_I$ is relevant in NMR, and this could be further simplified into

$$\boldsymbol{\mu}_I = \frac{g_n \mu_N}{\hbar} \boldsymbol{I} \tag{1.11}$$

Where, g_n is the g-factor of nucleus, μ_N is the nuclear magneton, since $\gamma_n = g_n \mu_N / \hbar$, then;

$$\boldsymbol{\mu}_I = \gamma_n \boldsymbol{I} \tag{1.12}$$

So the energy of a certain atom in a strong magnetic field (assuming the magnetic field is along z axis, and there is no coupling between $\boldsymbol{\mu}_I$ and $\boldsymbol{\mu}_J$) could be calculated by,

$$E_z = \langle \psi | H | \psi \rangle = \left\langle \psi \middle| H_0 + V_{mJ} - \gamma I B \middle| \psi \right\rangle = E_0 + E_{mJ} - \gamma_n m_I \hbar B \tag{1.13}$$

Therefore, when these nuclei have a nuclear spin angular moment quantum number, $I = 1/2$ for ^{1}H, for example, the energy difference between its two nuclear magnetic resonance states is

$$\Delta E = \gamma_n \hbar B \tag{1.14}$$

Hence, according to the Bohr rules, this energy difference could be quantized,

$$\nu_0 = \gamma_n B / 2\pi \tag{1.15}$$

Where ν_0 is the Larmor frequency, this resonance condition (the excitation wavelength in NMR should be at ν_0) is the fundamental principle of all the nuclear magnetic resonance experiments.

1.2.1.3 Nuclear Shielding

According to equation (1.14), every nucleus from the same species should have the same resonance energy in a certain magnetic field, however, since all the theories described above are based on the perturbation theory approximation[17], in reality the electron sphere interferes with the nuclear spin, so this is normally not this case in an ordinary molecule systems.

Hence, a simplified explanation of this discrepancy could be the existence of various other external magnetic fields, which replace B in equation (1.14) with B_{eff}, therefore, the magnetic field experience by a certain nucleus should be written with a correction factor,

$$B_{eff} = B_0(1 + \sigma) \tag{1.16}$$

Where σ is called shielding constant, and according to the direction of other external magnetic field, it could be further split into

$$\sigma = \sigma_{dia} + \sigma_{para} \tag{1.17}$$

Where σ_{dia} is the sum of the diamagnetic shielding effect (opposite to B_0, negative value), σ_{para} is the sum of the paramagnetic shielding effect (parallel to B_0, positive value).

The major source of discrepancy is the magnetic field induced by the circulation of electrons in the applied field, B_0, normally, the shielding constant caused by this effect is called σ_{loc} and it can be further separated into σ_{loc}^{para} and σ_{loc}^{dia} through the orbital that the electron occupies. (σ_{loc}^{dia} for the electron circulation within an s orbital, σ_{loc}^{para} for one in a p orbital) Beside local field effect,

other prominent effects[18] are the magnetic anisotropy of neighboring group (σ_N), the ring current effect in arenes (σ_R), the electric field effect (σ_e), and effects of intermolecular interaction (σ_i). Hence, the shielding constant σ could also be generally written as,

$$\sigma = \sigma_{loc}^{para} + \sigma_{loc}^{dia} + \sigma_N + \sigma_R + \sigma_e + \sigma_i \tag{1.18}$$

By analyzing the chemical shift pattern of the target molecule through effects described in equation 1.18, the structure information of the molecule can be deduced from an NMR spectrum with the help of spin-spin dipolar coupling effect.

1.2.1.4 Spin-Spin Dipolar Coupling

Although chemical shift offers chemists a great insight into the molecular structure, the largely overlapped chemical shifts by different effects only confuse people instead of helping to resolve the structure. Fortunately, the other phenomenon — spin-spin dipolar coupling's existence gives NMR the ability to provide information on the connectivity of molecules. (Though J-coupling for 1-D NMR spectrum can further complicate assignment, but it helps in 2-D NMR spectrum)

There are generally two different types of spin-spin dipolar coupling between nuclei in NMR. One is called direct dipole-dipole coupling, and the other is indirect dipole-dipole coupling (scalar- or *J*-coupling). Normally, the former (through space) effect is 1000 times larger than the latter (through bond) effect, and it causes significant observation problems in solid state NMR. However, in mobile isotropic solution state NMR, it is totally averaged to zero due to the rapid rotational diffusion of the molecule. Although it is still found in the NOE (Nuclear Overhauser Effect), which is caused by direct dipole-dipole coupling effect during nuclear spin relaxation.

The indirect interaction between nuclear dipoles actually arises from hyperfine interaction between the nuclei and local electrons[19], namely nucleus could perturb the electron spins of bonded nuclei, and this in turn perturbs the energy level of neighboring nuclei, therefore the scalar J-coupling is a through-bond interaction. At the same time, J coupling is also field independent and mutual, which offers great convenience when interpreting the spectrum (especially for first order multiplets). The strength of J coupling decreases rapidly with the increasing of the number of bonds between the two nuclei, and this property has been exploited as a tool to analyze the connectivity information of the molecule in NMR.

1.2.2 NMR Relaxation Mechanisms

Due to the existence of Zeeman splitting, when magnetization equilibrium is established in, for instance, a spin-1/2 spin system in a given magnetic field, according to thermodynamics, the whole system should be in its lowest energy state with a slightly larger number of spins occupying the lower nuclear magnetic energy level. As indicated in equation (2.15), if this kind of system were irradiated by radiofrequency pulse with a certain frequency corresponding to the Larmor frequency ν_0 of the interested nucleus, the equilibrium would be disturbed and the spin population distribution between the two nuclear magnetic energy levels would no longer adhere to the Boltzmann distribution statistics. Hence, if the new excited state of nuclei is not isolated and capable of an energy exchange with the environment, the whole system would undergo a process to return to its equilibrium state. This process is called relaxation.

There are two principal relaxation mechanisms. The first one is called spin-lattice relaxation (or longitudinal relaxation, T_1 relaxation), as indicated in its name, it corresponds to the energy change between excited nuclear spins and the lattice (lattice[20] is a continuum of nuclear magnetic moments (spins) of any sorts which surround the nuclear spins detected in NMR experiments). This T_1 relaxation decreases the total energy of the spin system, and covers it to its equilibrium state, so it is an enthalpy driven phenomenon.

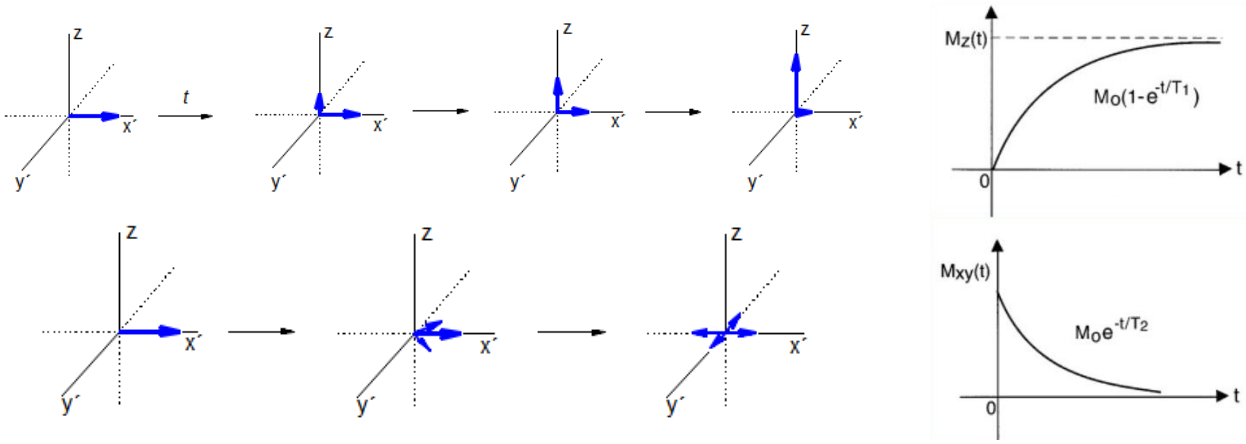

Figure 1.3 Two distinguishable relaxation processes in rotating frame: T_1 relaxation (top), T_2 relaxation (bottom)

In contrast, the second relaxation process has rather an entropic characteristic. The so-called spin-spin relaxation (or transverse relaxation, T_2 relaxation) is an interaction between identical spins with different orientations with respect to the external magnetic field. The total enthalpy of the spin system is actually unchanged during this process, however, the bulk magnetization M_{xy} is reduced, and the spin system therefore relaxes. Hence T_1 relaxation is the process of recovery of the spin system toward to its Boltzmann equilibrium, while the transverse relaxation process represents the loss of the spin coherence.

For the sake of explaining the relaxation process, the autocorrelation function has been introduced. The correlation function is a way of characterizing the time dependence of the random motion in the sample. Normally, the autocorrelation function $G(t,\tau)$ of the random motion in a specified system could be written as

$$G(t,\tau) = \frac{1}{N}\sum_{i=1}^{N} f_i(t) f_i(t+\tau) = \overline{f(t)f(t+\tau)} \tag{1.19}$$

where $f(t)$ is the time-dependent function, and the overbar indicates the ensemble average, namely average over the sample. As shown in equation (1.19), $G(t,\tau)$ depicts the rate of fluctuation of the stochastic process, for instance, the random Brownian motion of molecules. Generally, the exact form of $f(t)$ depends on the details of the interaction between the molecule and the solvent. For example, in the case of random rotational diffusion, $G(t,\tau)$ could be simplified into a single exponential form,

$$G(t,\tau) = \overline{f(t)^2} e^{-i|\tau|/\tau_c} \tag{1.20}$$

where τ_c is the correlation time. In rotational diffusion, the rotational correlation time means the average time it takes for a molecule to end up at an orientation about one radian from its starting position. For stationary random functions like in this case, the correlation function is independent of the time t. Therefore, $G(t,\tau)$ could be rewritten as $G(\tau)$. On the other hand, $G(\tau)$ has its maximum value at τ=0, function (1.20) and so can be rewritten as,

$$G(\tau) = G(0) e^{-i|\tau|/\tau_c} \tag{1.21}$$

The Fourier Transform of equation (1.21) would lead to a Lorentzian function, which provides the information about the proportion of the molecules with a specified rate of fluctuation of the motion. This Lorentzian function is called spectral density function. The spectral density function $J(\omega)$ corresponding to $G(\tau)$ in equation (1.21) is

$$J(\omega) = \int_0^\infty G(\tau) e^{-i\omega\tau} d\tau = G(0) \frac{2\tau_c}{1 + \omega^2 {\tau_c}^2} \tag{1.22}$$

This is the generalized form of spectral density function, and it can be used to calculate relaxation time, since the relaxation rate of a given system depends on its spectral density at the characteristic frequency, w, (in case of NMR, it is Larmor frequency of the nucleus). Despite the variety of relaxation mechanisms and the different origin of nuclear coupling, relaxation rates $1/T_1$ could be expressed as (the pre-factor C is a constant specific for the type of the dominating spin coupling),

$$\frac{1}{T_1} = CJ(\omega_0, \tau_C) \tag{1.23}$$

Meanwhile, in the context of NMR, the local magnetic field fluctuation (the main driving force for relaxation) is due to reorientations of dipolar vectors with respect to the direction of the external magnetic field. When these molecular motions have large amplitudes and random character, then the spectral density function, $J(\omega_0, \tau_C)$, takes the Bloembergen-Purcell-Pound form[21], and the rate of spin-lattice relaxation $1/T_1$ by homonuclear dipole-dipole interactions is:

$$\frac{1}{T_1} = \frac{3\mu_0^2}{160\pi} \frac{\hbar^2 \gamma^4}{r^6} \left[\frac{\tau_c}{1 + {\omega_0}^2 {\tau_c}^2} + \frac{4\tau_c}{1 + 4{\omega_0}^2 {\tau_c}^2} \right] \tag{1.24}$$

where μ_0 is the magnetic permeability of free space, $\hbar$ the reduced Planck constant, γ gyromagnetic ratio, r the distance between the nuclei carrying magnetic dipole moment, ω_0 is Larmor frequency of studying nuclei in corresponding magnetic field, τ_c correlation time of the molecular tumbling motion. The terms in square brackets arise due to the possibility of the dipolar Hamiltonian being modulated by one- or by two-spin flips. By analogy, $1/T_2$ also could be written as,

$$\frac{1}{T_2} = \frac{3\mu_0^2}{320\pi} \frac{\hbar^2 \gamma^4}{r^6} \left[3\tau_c + \frac{5\tau_c}{1 + {\omega_0}^2 {\tau_c}^2} + \frac{2\tau_c}{1 + 4{\omega_0}^2 {\tau_c}^2} \right] \tag{1.25}$$

The first term in square brackets arises from the spectral density at zero frequency (which cannot contribute to T_1), this is the reason for the sensitivity of T_2 to slow motions. Finally, as have been mentioned before, normally there would be more than one relaxation mechanisms play important roles during the relaxation process, these interferences often create the so-called cross-correlation mechanism. However, only independent mechanisms would be discussed, the apparent relaxation rate could be treated as

$$\frac{1}{T_i} = \sum_m \frac{1}{T_i^m} \tag{1.26}$$

In polymeric systems, although T_1 relaxation time is largely affected by the local segmental mobility, it is not very sensitive for networks with low crosslink density due to the reciprocal dependence of T_1 on crosslink density.[22, 23] On the other hand, T_2 is very sensitive to even small differences in the cross-link density because for rubbery materials this relaxation time is largely governed by constraints on large spatial-scale chain mobility imposed by chemical and physical crosslinking.[23]

1.2.3 Magic Angle Spinning (MAS)

Solid state NMR is quite different from its liquid counterpart from the view point of spectral resolution. Its resonance line width is much broader than the corresponding liquid sample. The reason for this large difference is due to the rapid tumbling of the molecules in the solution which averages out the orientation angle used to describing the orientation of the shielding/dipolar tensor with respect to the applied field $\boldsymbol{B_0}$.

In solid state physics, several anisotropic spin interactions could lead to the broadening and overlapping of spectral lines. Among them, three interactions, chemical shift anisotropy (Hz), (heteronuclear and homonuclear) dipolar couplings (kHz), and quadrupolar couplings (MHz) contribute most significantly to these phenomena. In order to efficiently reduce these contributions to the spectra which can mask the information of interest, the magic angle spinning (MAS) technique is often applied in solid state NMR.

The total dipolar (or quadrupolar) Hamiltonian does not commute with the Zeeman Hamiltonian, however, parts of the dipolar Hamiltonian do commute, and are therefore easily observed in the NMR spectra of solids. Most of these commutable terms contain $(3\cos^2\theta - 1)$ angular terms in their corresponding equations. The MAS technique basically exploits the $(3\cos^2\theta - 1)$ dependence of the transition frequencies[24] to make the commutable Hamiltonian terms approach zero on the NMR timescale. In its setup, the sample would be spinning about an axis inclined at an angle θ_R to the applied field, therefore θ, the angle which is describing the orientation of the interaction tensor fixed in a molecule within the sample, varies with time as the molecule rotates with the sample. The average of $(3\cos^2\theta - 1)$ in this circumstance can be illustrated as following:

$$\langle 3\cos^2\theta - 1\rangle = \frac{1}{2}(3\cos^2\theta_R - 1)(3\cos^2\beta - 1)$$

As shown in Fig. 2.4, the angle β is between the principal z-axis of the shielding tensor and the spinning axis; θ_R is the angle between the applied field and the spinning axis; θ is the angle between the principal z-axis of the interaction tensor and the applied field $\boldsymbol{B_0}$. The angle β is fixed for a given nucleus in a rigid solid, but it could be every possible values in a powder samples. However, the angle θ_R is adjusted and controlled in the experiment. In order to make $\langle 3\cos^2\theta - 1\rangle$ equal to zero, θ_R can be adjusted to 54.74°. Provided that the spinning rate is fast enough that θ is averaged rapidly compared with the anisotropy of the interaction, the interaction anisotropy averages to zero.

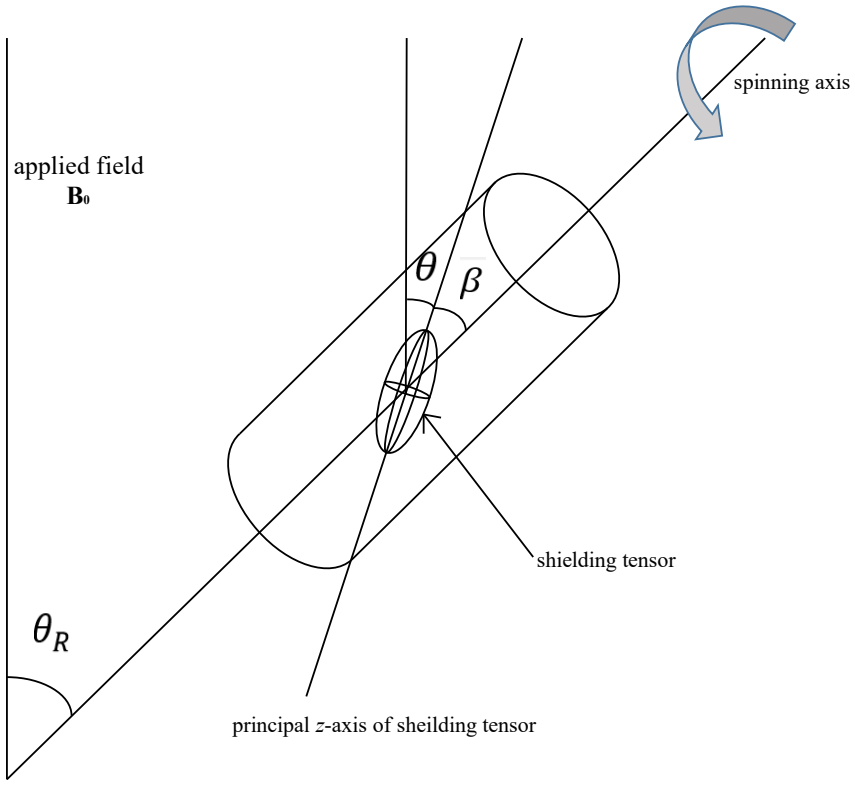

Figure 1.4 The magic angle spinning experiments setup.

MAS could average the anisotropy associated with any interaction which causes a shift in the energies of the Zeeman spin functions, such as chemical shift anisotropy, heteronuclear dipolar coupling, but not mixing between Zeeman functions (e.g. higher order quadrupolar coupling). However, it also has an effect on secular interactions which mix Zeeman functions.[25]

1.3 Polymer Physics Background Theories

In recent decades, polymer science has evolved into a new era with expanded applications of a whole new range of polymeric materials thanks to rapid developments in material sciences. This somehow also posts a huge challenge for polymer physicists to devise methodologies for systematically analyzing this large quantity of new materials. Traditionally, due to their sheer size, polymers are very difficult to analyze by using a deterministic method (e.g. optical spectroscopy). However, with the introduction of several useful theoretical models[26], the implementation of statistical approaches in the field of polymer analysis achieved a great success. Hence, it is necessary to have some basic understanding of these statistical theories before we get further into the analyses.

1.3.1 Statistical Properties of Polymer Chains

In case of an ideal chain system, the fundamental entropy-related properties of macromolecules could be characterized via statistical models for the spatial arrangement of the individual monomeric units of a polymer chain. One of simplest models is the freely jointed chain model. In this model, N+1 equal monomer units are connected through N rigid bonds with effective bond length b (Kuhn length), while these bonds are completely free to rotate and no inter-molecular interactions is considered in this model. Hence, the orientation of inter-monomeric connecting vectors $\overrightarrow{b_i}$ is of purely statistical nature, which results in the conformation of the polymer chain could be described mathematically through a random walk. Therefore the contour length l_0 (the length of a polymer chain at its maximum physically possible extension) could be obtained through the sum over the length of all inter-monomeric connections

$$l_0 = \sum_{i=1}^{N} \left|\overrightarrow{b_i}\right| = bN \tag{1.27}$$

Meanwhile, the root mean square end-to-end distance, $\sqrt{\langle \overrightarrow{r_n}^2 \rangle}$, of the terminal monomers of the polymer chain is another measure of the polymer chain length, in which $\overrightarrow{r_n}$ represents the connecting vector between the two end monomers and is called end-to-end vector. This vector could be calculated through all the N statistically independently oriented vector, namely $\overrightarrow{r_n} =$

$\sum_{t1}^{n} \overrightarrow{b_i}$. Obviously, the average end-to-end vector of an isotropic collection of chains with n backbone atoms is zero. However, its mean square, $\langle \overrightarrow{r_n}^2 \rangle$ has a value of Nb^2 in the freely jointed chain model in which no correlations between the directions of different bond vectors are concerned. Hence,

$$\sqrt{\langle \overrightarrow{r_n}^2 \rangle} = bN^{0.5} \tag{1.28}$$

Normally, the above mentioned distance is significantly smaller than the contour length as a proof of the presence of random chain coil formation. Meanwhile, the distribution of the end-to-end vectors $P_N(\vec{r})$ follows the classical Gaussian description if a sufficient number of Kuhn sections is presented in the polymer chain. Its representation could be drawn as follows[27],

$$P_N(\vec{r}) = \left(\frac{3}{2\pi b^2 N}\right)^{3/2} e^{-\frac{3\overrightarrow{r_n}^2}{2b^2 N}} \tag{1.29}$$

For an ideal chain, since the chain is assumed to be free of inter-molecular interactions (U=0), the Helmholtz free energy could be written as,

$$F(N,\vec{r}) = -T\Delta S - F(N,0) = \frac{3k_B T\overrightarrow{r_n}^2}{2b^2 N} - F(N,0) \tag{1.30}$$

Furthermore, in the case of a small deformation ($\overrightarrow{r_n} \ll Nb$), the elastic response of the material is the first derivative of $F(\vec{r})$, which makes it an entropic property as well,

$$\vec{f} = \frac{3k_B T\overrightarrow{r_n}}{b^2 N} \tag{1.31}$$

This so-called 'entropy elasticity' is often used in the interpretation of the statistical reason for rubber-like elasticity behavior.

In contrast to the ideal chain model mentioned above, inter-monomeric interactions in real chains create an energy barrier when it comes to the free rotation of individual bond. This internal hindrance affects the chain statistics in many ways, however, the fundamental nature of a Gaussian chain, such as its mean square end-to-end distance $\langle \overrightarrow{r_n}^2 \rangle$ remains unchanged, though a correction

constant should be introduced to modify the proportional relationship between $\langle \overrightarrow{r_n}^2 \rangle$ and N. This proportionality constants is call Flory's characteristic ratio[28],

$$C_n = \frac{\langle \overrightarrow{r_n}^2 \rangle}{nb^2} \tag{1.32}$$

Its numerical value depends on the local stiffness of the polymer chain. Normally, a polymer chain with a large characteristic ratio is difficult to bend, and could take an extended conformation along its axis (bulky).

The statistical conformation of a polymer chain could be approximately considered as a sphere which is composed by random coils. The size of this sphere could be defined by the radius of gyration whose square value could be determined by the average square distance between monomers in a given conformation and the polymer's center of mass,

$$r_g{}^2 = \frac{1}{N}\sum_{i=1}^{N}(\vec{r_i} - \overrightarrow{r_{CM}})^2 \tag{1.33}$$

Where $\vec{r_i}$ is the position vector for a monomer in a given conformation, $\overrightarrow{r_{CM}}$ is the position vector for the polymer's center of mass (which could be calculated through $\overrightarrow{r_{CM}} = \frac{1}{N}\sum_{j=1}^{N}\vec{r_i}$

For an ideal linear chain, the mean square radius of gyration is directly related to the end-to-end distance of the corresponding chain,

$$\langle \overrightarrow{r_g}^2 \rangle = \frac{b^2 N}{6} = \frac{\langle \overrightarrow{r_n}^2 \rangle}{6} \tag{1.34}$$

1.3.2 Polymer Dynamics

The first successful molecular model of polymer dynamics was developed by Rouse[29, 30] for non-entangled polymers. In this model, the chain, as shown in Figure 3, is represented as N beads connected by springs with root-mean-square size b. And every individual bead only interacts with each other through the connecting spring. A friction coefficient ζ is used to characterize each bead's own independent friction, since the mobility of the Rouse chain is dominated by the viscous friction forces of the beads with their environment.

The time for the polymer to diffuse the distance of the order of its own size is called Rouse time, τ_R. It is a characteristic value in Rouse model and could be calculated through Einstein diffusivity relation:

$$\tau_R \approx \frac{\langle \overrightarrow{r_n}^2 \rangle}{D_R} = \frac{\zeta}{k_B T} N^2 b^2 \tag{1.35}$$

Where ζ is the friction coefficient mentioned before. Meanwhile, due to the fractal nature of polymer, the relationship between the single Rouse segment relaxation time τ_0 (the shortest relaxation time for a Rouse chain) and the Rouse time τ_R (the longest relaxation time for a Rouse chain) follows a power law dependence on the reciprocal of the fractal dimension of the polymer, which appears as the power index ν,

$$\tau_R \approx \tau_0 N^{2\nu+1} \tag{1.36}$$

The Rouse time has special significance. When probed on time scales smaller than τ_0, the polymer basically does not move and responds to stress elastically. On the other hand, when $t > \tau_R$, the polymer behaves like viscous liquid, and has a fluid response toward to the outside stress. For the intermediate time scale, $\tau_0 < t < \tau_R$, the polymer chain has a complex viscoelastic behavior to the stress since some of the modes (Rouse mode) are not yet relaxed.

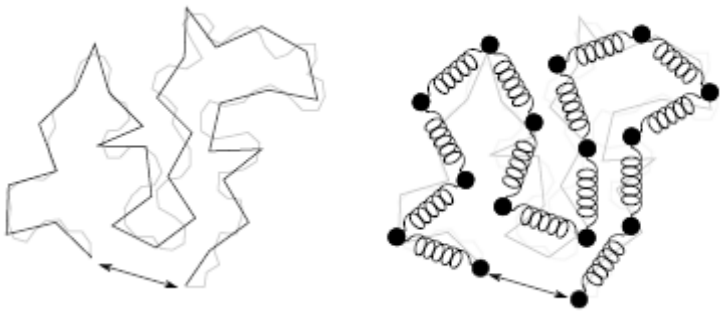

Figure 1.5 (left) Kuhn Segment representation of chain conformation; (Right) Rouse Model representation.

In the treatment applied above, the relaxation is not restricted by topological constraints, therefore it is referred as Free Rouse relaxation. However, when the length of polymer chain reaches a certain level, chain entanglement starts to occur, which applies a topological restriction on the polymer dynamics. This phenomenon causes the dramatic increase in the viscosity of the polymer

melt. In this case, the influence of the entanglements on the polymer dynamics and the center of mass diffusion is described by the Edwards tube model [31]. In this model, the collective effect of all the surrounding polymer chains on a given strand is described by a quadratic constraining potential acting on every monomer of the strand. The minima of these constraining potentials lies along the primitive path, which is the shortest way to connect the two ends of the tube-like region subject to topological constraints. Each monomer is constrained to close to the primitive path with some limited thermal fluctuation. The width of the tube is defined by strand excursions that have free energy kT above the minimum at the primitive path. This tube diameter a can be interpreted as the end-to-end distance of an entanglement strand of N_e monomer,

$$a \approx bN_e^{\nu} \tag{1.37}$$

Furthermore, the entanglement molar mass of the entangled strand could be defined as $M_e = N_e M_0$. And it could be calculated through the rubbery plateau modulus (G_e) as,

$$M_e = \frac{\rho RT}{G_e} \tag{1.38}$$

This demonstrates the large influence of chain entanglement (topological properties) on the viscoelastic behavior of polymer material as it affects the network modulus.

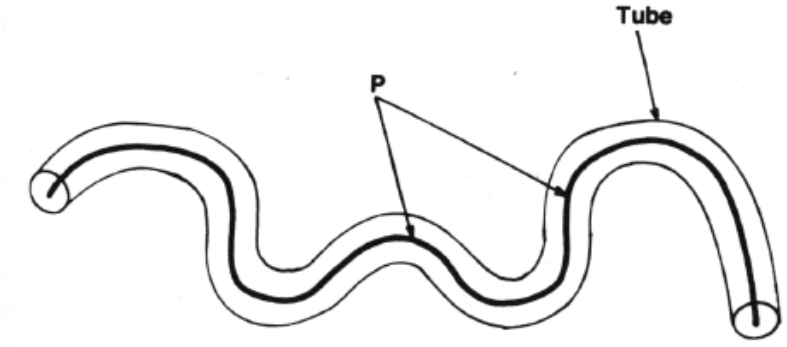

Figure 1.6 Simple representation of tube model.

Meanwhile, there is an analogy between free Rouse dynamics and tube dynamics due to the finite expansion of the tube. The entanglement time τ_e (also called equilibration time), which is the time when the influence of the entanglement project on the relaxation of the entangled strand, also

corresponds to the time an entanglement strand requires to diffuse over half of the tube diameter distance. It also could be shown as,

$$\tau_e \approx \frac{a^2}{D_e} = \frac{\zeta}{kT} N_e a^2 \tag{1.39}$$

Similar to $\tau_R \sim N^2$, in the case of ideal linear polymer chains, τ_e is also proportional to ${N_e}^2$. This similarity could be explained as τ_e is the Rouse relaxation time of a chain of length equal to one tube segment.

Finally, the time required by the main chain to move a whole contour length l_0 is denoted as the reptation disentanglement time τ_d,

$$\tau_d \approx \frac{{l_0}^2}{D_d} = \frac{\zeta}{kT} N {l_0}^2 \tag{1.40}$$

By inserting equation (1.27) into the above, the relation $\tau_d \sim N^3$ can be obtained. This disentanglement time τ_d represents the longest relaxation time in an entangled polymer system, over which the whole diffuses out of the constraint tube.

For an entangled polymer, there are four relaxation times involved instead of two, as in the case of un-entangled polymers. The additional two relaxation times further divided the dynamics in tube model into 5 dynamic regimes, due to the dominant influence of different relaxation mechanisms and topological restrictions on the chain dynamics on different time scales. The new dynamic regime at the time scale $\tau_e < t < \tau_R$ represents a transitional regime in which the Rouse dynamics is restricted to one dimension. While at $\tau_R < t < \tau_d$, the polymer follows reptation dynamics[32].

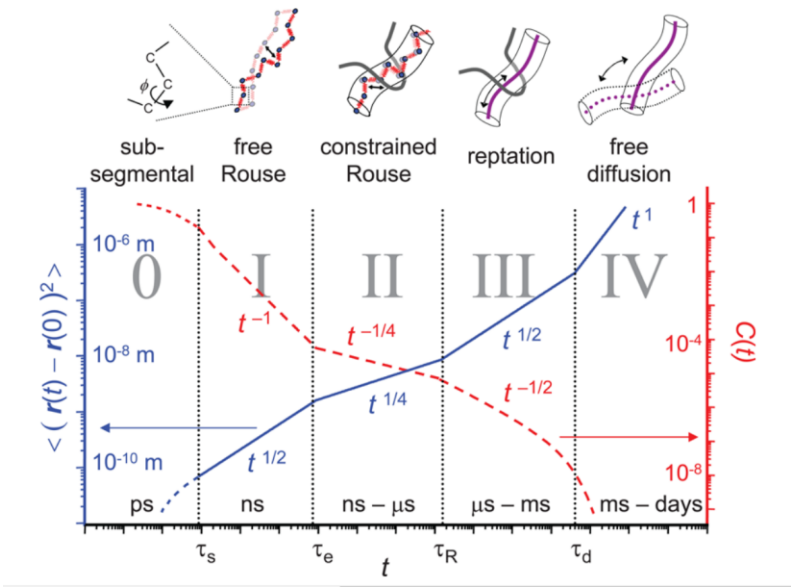

Figure 1.7 Dynamic regimes and the crossover times as predicted by the tube model, shown for the mean-square displacement $\langle [r(t) - r(0)]^2 \rangle$ of a tagged monomer (solid line), and the normalized segmental OACF $C(t)$ (dashed line). The transitions between the regimes occur at the segmental (τ_s), entanglement (τ_e), Rouse (τ_R), and disentanglement (τ_d) times. Reused from Chavez's 2011 paper.[33]

Despite the strong assumptions involved the Rouse model as well as the tube model shows a good agreement with experiments[34] and simulations[35]. Therefore, they have been widely applied in the study of various different polymer materials due to the applicable beyond material-specific chain length and relaxation time scale issues.

1.4 Introduction to the thesis

As the most promising polymeric material for its biomedical application in industry, hydrogels have attracted huge attention in recent years. Among all the applications, hydrogel-derived drug delivery systems (DDS) are the most prominent ones. By tailoring the physico-chemical properties of these hydrogels, one can realize the release of therapeutic agents from the matrix in a controlled manner. The other frequently mentioned industrial application of hydrogels is hydrogel contact lenses (for Si-based hydrogels especially). In this thesis, we will study the relationship between the microscopic structure of hydrogel and its macroscopic properties (e.g. mechanical properties), particularly for the materials used in industry for DDS and contact lenses applications.

Chapter 1 presents a concise introduction about hydrogel materials, and the mechanism for photo-initiated free radical polymerization – the most frequently used polymerization reaction in industry. Subsequently, the relevant theories about the Nuclear Magnetic Resonances (NMR) analysis of polymers will be summarised, since NMR is the main technique used in this project. Finally, a brief illustration about the polymer chain dynamics will be offered in order to facilitate understanding of these theoretical models used in this thesis.

The main experimental methodologies used in this thesis will be described in Chapter 2, including the key NMR techniques; NMR relaxomtery, NMR diffusometry and NMR Multiple Quantum (MQ) analyses. Thermal analysis has been used across the thesis as a routine method for polymer analyses, hence a succinct description of Differential Scanning Calorimetry (DSC) and Dynamic Mechanical Analyses (DMA) will also be provided.

Chapter 3 is a published work focusing on the effect of the network's topological properties on its physico-chemical properties. Through crosslink density analyses of a series of polyacrylate network by DMA, NMR relaxometry and NMR Double Quantum (DQ) analyses, it was found the topological properties (e.g. point-like junction network and zip-like junction network) affect the applicability of the classical rubber elasticity model. This is important for designing the next generation DDS, since modifying crosslink density has been used extensively in controlling the drug release rate in DDS.

Chapter 4 is a work discussing the effect of H-bonding on the network's macroscopic properties. An alternative approach to crosslink density for controlling drug release rate in DDS is to adjust

the interaction between the solute molecule and the hydrogel matrices. One way to achieve this is to add hydrogen bonding into the system. However, the pre-organization phenomenon induced by H-bonding during the curing process, largely alters the morphological and topological properties of the network. In this study, a series of network with different H-bonding groups were analysed by thermal and NMR methods; the pre-organization phenomenon was found to be affected by the nature of the hydrogen bonding group in the side chain of the monoacrylates used in the network synthesis. It was also found that the crosslink density of the network could also be altered due to the presence of the hydrogen bonding.

Application of NMR diffusometry is the main topic of Chapter 5, which is closely related to Chapter 4. This study examines the diffusion process of small drug mimics inside several different gel matrices with and without hydrogen bonding capability. The difference in the diffusion coefficient of Eosin-Y in these gel matrices is discussed in relation to the mesh size of these networks, the morphological difference presented in Chapter 5 and the position of the hydrogen bonding group.

Finally, as mentioned above, the other major application of hydrogels is contact lenses. Although they have been commercialized for quite some time, Si-based hydrogels are still interesting materials to study due to their complicated morphological properties. In Chapter 6, the oxygen permeability inside several commercialized gels was investigated by transient measurements and NMR. By comparing these two data sets, the difference between oxygen solubility values generated by these methods were explained under the influence of heterogeneous morphology of these networks.

References

1. E. Calo, V. V. Khutoryanskiy, Biomedical applications of hydrogels: A review of patents and commercial products. *Eur Polym J* **65**, 252 (Apr, 2015).
2. L. Klouda, A. G. Mikos, Thermoresponsive hydrogels in biomedical applications. *Eur J Pharm Biopharm* **68**, 34 (Jan, 2008).
3. R. Barbucci, *Hydrogels biological properties and applications*. (Springer Italia, Milano, 2009), pp. 197 S.
4. D. B. Stein, *Handbook of hydrogels properties, preparation & applications*. Chemical engineering methods and technology series (Nova Science Publishers, New York, 2009), pp. xx, 750 p.
5. N. A. Peppas, *Hydrogels in medicine and pharmacy*. (CRC Press, Boca Raton, Florida, 1986), pp. 3 vol.
6. S. Rimmer, *Biomedical hydrogels Biochemistry, manufacture and medical applications*. Woodhead publishing in materials (Woodhead Publishing, Oxford, 2011), pp. 269 S.
7. K. B. Keys, F. M. Andreopoulos, N. A. Peppas, Poly(ethylene glycol) star polymer hydrogels. *Macromolecules* **31**, 8149 (Nov 17, 1998).
8. M. J. Yaszemski, *Tissue engineering and novel delivery systems*. (Dekker, New York, 2004), pp. 645 S.
9. S. Y. Kim, H. S. Shin, Y. M. Lee, C. N. Jeong, Properties of electroresponsive poly(vinyl alcohol)/poly(acrylic acid) IPN hydrogels under an electric stimulus. *J Appl Polym Sci* **73**, 1675 (Aug 29, 1999).
10. C. S. Bagdasarjan, *Theory of free-radical polymerization*. (IPST, Jerusalem, 1968), pp. 317 S.
11. S. Jonsson, P. E. Sundell, J. Hultgren, D. Sheng, C. E. Hoyle, Radiation chemistry aspects of polymerization and crosslinking. A review and future environmental trends in 'non-acrylate' chemistry. *Prog Org Coat* **27**, 107 (Jan-Apr, 1996).
12. M. J. Kade, D. J. Burke, C. J. Hawker, The Power of Thiol-ene Chemistry. *J Polym Sci Pol Chem* **48**, 743 (Feb 15, 2010).
13. K. Matsukawa, T. Fukuda, S. Watase, H. Goda, Preparation of Photo-curable Thiol-Ene Hybrids and Their Application for Optical Materials. *J Photopolym Sci Tec* **23**, 115 (2010).
14. K. Y. Tan, M. Ramstedt, B. Colak, W. T. S. Huck, J. E. Gautrot, Study of thiol-ene chemistry on polymer brushes and application to surface patterning and protein adsorption. *Polym Chem-Uk* **7**, 979 (2016).
15. P. J. Flory, J. Rehner, Statistical Mechanics of Cross‐Linked Polymer Networks II. Swelling. *The Journal of Chemical Physics* **11**, 521 (1943).
16. P. J. Flory, *Principles of polymer chemistry*. George Fisher Baker non-resident lectureship in chemistry at Cornell University (Cornell University Press, Ithaca etc., ed. [Tenth printing], 1978), pp. XVI, 672 S.
17. J. Mason, Interpretation of Carbon Nuclear Magnetic-Resonance Shifts .3. Variation of Local Diamagnetic Shielding Term in C-13 Nmr as Determined by Calculation and by X-Ray Photoelectron-Spectroscopy. *Org Magn Resonance* **10**, 188 (1977).
18. H. Friebolin, *Basic one- and two-dimensional NMR spectroscopy*. (WILEY-VCH, Weinheim ;, ed. 5th completely rev. and enlarged, 2011), pp. xxiv, 418 p.
19. E. L. Hahn, D. E. Maxwell, Spin Echo Measurements of Nuclear Spin Coupling in Molecules. *Phys Rev* **88**, 1070 (1952).
20. J. Keeler, *Understanding NMR spectroscopy*. (John Wiley and Sons, Chichester, U.K., ed. 2nd, 2010), pp. xiii, 511 p.
21. N. Bloembergen, E. M. Purcell, R. V. Pound, Relaxation Effects in Nuclear Magnetic Resonance Absorption. *Phys Rev* **73**, 679 (1948).

22. J. P. C. Addad, L. Pellicioli, J. J. H. Nusselder, End-linked calibrated polypropylene-oxide chains. NMR approach to segmental fluctuations. *Polym Gels Netw* **5**, 201 (1997/04/01, 1997).
23. J. P. C. Addad, NMR and fractal properties of polymeric liquids and gels. *Prog Nucl Mag Res Sp* **25**, 1 (1993/01/01, 1993).
24. A. E. McDermott, T. Polenova, *Solid-state NMR studies of biopolymers*. (John Wiley & Sons, Chichester, West Sussex, 2010), pp. xx, 572 p.
25. H. Saitô, I. Ando, A. Naito, *Solid state NMR spectroscopy for biopolymers : principles and applications*. (Springer, Dordrecht, 2006), pp. xiii, 464 p.
26. M. Rubinstein, R. H. Colby, *Polymer physics*. (Oxford University Press, Oxford ; New York, 2003), pp. xi, 440 p.
27. H. B. Bohidar, *Fundamentals of polymer physics and molecular biophysics*. pp. 1 online resource.
28. P. J. Flory, *Statistical mechanics of chain molecules*. (Hanser etc., Munich etc., ed. Reprinted, 1989), pp. XXV, 432 S.
29. P. E. Rouse, A Theory of the Linear Viscoelastic Properties of Dilute Solutions of Coiling Polymers. *J Chem Phys* **21**, 1272 (1953).
30. P. E. Rouse, A theory of the linear viscoelastic properties of dilute solutions of coiling polymers. II. A first-order mechanical thermodynamic property. *J Chem Phys* **108**, 4628 (Mar 15, 1998).
31. S. F. Edwards, Statistical Mechanics of Polymerized Material. *P Phys Soc Lond* **92**, 9 (1967).
32. P. G. Degennes, Reptation of a Polymer Chain in Presence of Fixed Obstacles. *J Chem Phys* **55**, 572 (1971).
33. F. V. Chavez, K. Saalwachter, Time-Domain NMR Observation of Entangled Polymer Dynamics: Universal Behavior of Flexible Homopolymers and Applicability of the Tube Model. *Macromolecules* **44**, 1549 (Mar 22, 2011).
34. V. A. Harmandaris *et al.*, Crossover from the rouse to the entangled polymer melt regime: Signals from long, detailed atomistic molecular dynamics simulations, supported by rheological experiments. *Macromolecules* **36**, 1376 (Feb 25, 2003).
35. A. Baumgartner, U. Ebert, L. Schafer, Segment motion in the reptation model of polymer dynamics. II. Simulations. *J Stat Phys* **90**, 1375 (Mar, 1998).

Chapter II

Experiment Methods

2.1 Nuclear Magnetic Resonance

Due to its great sensitivity to chemical structure and dynamics, NMR is one of the most frequently used techniques to analyzing novel materials. Since its inception, several different NMR methodologies with their specialties on understanding different aspects of properties in interested materials have been devised to suit various needs of scientists.[1-5] In this study, besides routine NMR spectroscopy, we mainly implemented NMR relaxometry, NMR diffusometry and Double Quantum (DQ) NMR analyses – these three methodologies to investigate the structural and dynamic information of our hydrogel materials.

2.1.1 NMR relaxometry

As mentioned in the previous chapter, relaxation phenomenon in NMR is of great interest in probing quadrupolar and paramagnetic interactions, and exchange dynamics.

(a) Hahn Echo (Spin Echo) pulse sequence

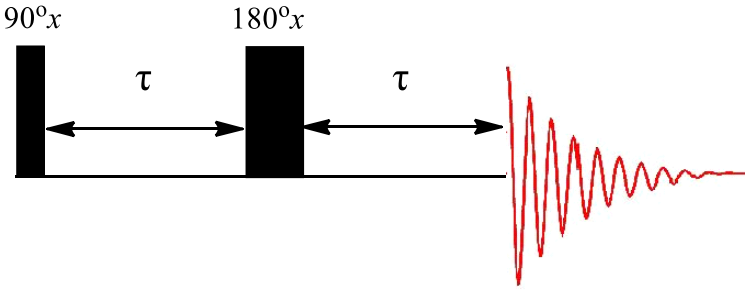

Figure 2.1 Simple illustration of Hahn Echo (spin echo) pulse sequence.

Hahn echo (spin echo), is named after Erwin Hahn who discovered it in 1950[6], can be counted as the most important development in the history of NMR. In this pulse sequence, the first 90° tips all the spins into the transvers x-y plane. Due to the local field effect (local magnetic field 'inhomogeneity') every spin experiences a different magnetic field, and hence precesses at a different frequency. This results in gradual spreading out, of the magnetization in the transverse x-y plane (coherence dephasing). However the 180° pulse reverses each spin orientation, so that after the flip, the faster precessing spin lags behind its slower counterparts. With the evolution continuing, the faster spins eventually catch up with the slower ones. This happens by the end of the Hahn Echo (coherence refocusing).

Hence in the Hahn echo experiment, spin phase information, which is apparently 'lost' due to the decay of the FID, is 'regenerated' after the echo.[6] The reason behind this regeneration is because precession arising due to inhomogeneities, contributing to T_2^* that gave rise to the original decay of the FID can be reversed, if diffusion is minimal. In fact, the attenuation of the FID signal is merely due to the disorganization of spin order because the individual spins comprising FID signal have lost their phase coherence. The system is said to possess a 'hidden order' or 'atomic memory'[7] which can be recovered.

(b) Solid Echo pulse sequence

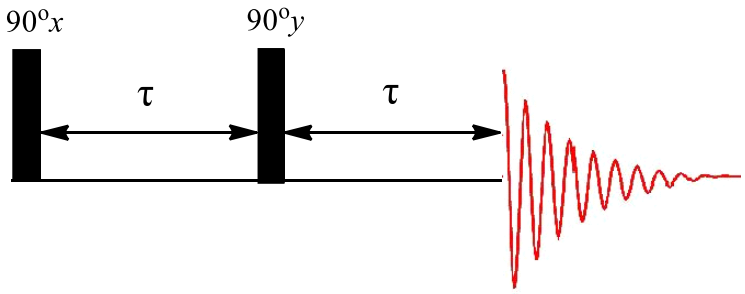

Figure 2.2 Simple illustration of Solid Echo pulse sequence.

Rapidly decaying FID can be difficult to be completely record, due to probe ringing. Rapid decays, common in solid state NMR signal for rigid crystalline materials, give rise to extremely broad line-shapes. This can result in the loss of signal intensity as well as spectral distortion. In part to overcome these problems the solid-echo pulse sequence was devised to refocus the dipolar (also quadrupolar) couplings. This refocusing effect is generated by the second 90° pulse (see Figure 2.2) at a time 2τ after the initial 90° pulse. Unlike the Hahn echo, the two 90° pulses in solid echo must be 90° out of phase relative to each other. As in every echo experiment, the echo maximum is at time τ after the second pulse. Since this pulse sequence is used to refocus the dipolar coupling, the echo delay τ should be smaller than the inverse coupling constant of the interest spin system.

(c) Inversion Recovery (IR) pulse sequence

Unlike the two pulse sequences introduced before, which are used to measure T_2, the Inversion Recovery pulse sequence is used to measure the longitudinal relaxation time, T_1.

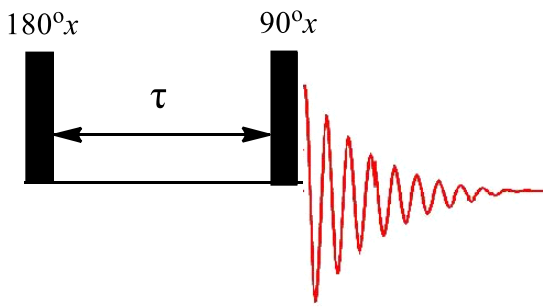

Figure 2.3 Simple illustration of Inversion Recovery (IR) pulse sequence.

As shown in the Figure 2.3, this pulse sequence starts with a 180° pulse that inverts the population to the $-\boldsymbol{I}_z$ (the opposite direction to the magnetic field). During the delay time τ that follows the spins are allowed to relax until another 90° pulse creates the observable transverse magnetization in the x-y plane, the resulted FID is then recorded. The magnitude and sign of the peaks in the spectrum depends on the longitudinal relaxation rate of each spin. By systematically varying τ, individual peak's intensity can be acquired as a function of τ, and it is related to the z-magnetisation just before the second pulse, by.

$$M_z = M_0\left(1 - 2e^{-t/T_1}\right) \tag{2.1}$$

Hence, through fitting the curve with the above equation one can extract the T_1 value for individual resonances.

2.1.2 NMR Diffusometry

Due to the recent development in the field of Pulsed Field Gradients (PFG)[8], translational diffusion-related properties with chemical shift specification can be characterized by NMR spectroscopy. Translational diffusion is the random Brownian motion of molecules or ions that is driven by internal thermal energy.[9] The mathematics of the translational diffusion process has been verified for systems in which an initial concentration gradient is established. Fick's first law postulates that the flux of molecules across a given plane is proportional to the concentration gradient across the plane,

$$J = -D\frac{\partial C(x,t)}{\partial x} \tag{2.2}$$

Where J is the flux, D is the diffusion constant for the molecule that is diffusing in the specific solvent, and $(\partial C(x,t))/\partial x$ is the concentration gradient. The diffusion constant of a substance is expressed in units of m^2/s. The negative sign of the right side of the equation indicates that the solute molecules are flowing in the direction of lower concentration. Fick's First Law does not take into account the fact that the gradient and local concentration of the solutes in a material decreases with time, which is an important aspect to diffusion processes.

On the other hand, Fick's Second Law states that the change in the concentration over time is equal to the change in local diffusion flux, or

$$\frac{\partial C(x,t)}{\partial t} = -\frac{\partial J}{\partial x} \tag{2.3}$$

Or in a from derived from the Fick's First Law,

$$\frac{\partial C(x,t)}{\partial t} = D\frac{\partial^2 C(x,t)}{\partial x^2} \tag{2.4}$$

Where it is supposed that the diffusion coefficient is independent of position.

In an isotropic system, without thermal or concentration gradients, the average molecule displacement in all three directions is zero but the mean square displacement is non-zero and is given by

$$\langle r^2 \rangle = 6Dt \tag{2.5}$$

Following Stokes' Law, the force needed to move a small sphere of radius R through a continuous medium of viscosity η with a velocity V is

$$F = 6\pi\eta RV \tag{2.6}$$

The Stokes-Einstein equation then describes how the diffusion coefficient increases in proportion to temperature, and in inverse proportional to the frictional force experienced by a molecule

$$D = \frac{k_B T}{f} \tag{2.7}$$

Where f is given by the Stoke's Law, $f = 6\pi\eta R$. Combining the above two equations leads to the well-known relation

$$D = \frac{k_B T}{6\pi\eta R} \tag{2.8}$$

Typical self-diffusion coefficients in liquids at room temperature range from 10^{-9} m^2s^{-1} (small molecules in non-viscous solution) to 10^{-12} m^2s^{-1} (polymers with high M_w in solution).

The PFG NMR method for studying diffusion procedure was first theoretically and experimentally demonstrated by Stejskal and Tanner. In their seminal paper[10], these authors introduced the pulsed field gradients into the classical Hahn Echo (Spin Echo) pulse sequence, which resulted in much improved sensitivity to diffusion in comparison tosteady state gradients used previous. They solved the Bloch-Torry partial differential equations[11] for a symmetric pair of pulsed gradients and obtained the well-known Stejskal-Tanner formula.

$$S(t) = S(0)exp\left[-D\gamma^2 g^2 \delta^2 \left(\Delta - \frac{\delta}{3}\right)\right] \tag{2.9}$$

Where D is the self-diffusion coefficient of the solute, γ is the magnetogyric ratio of the targeting nucleus, g is the gradient strength, δ is the applied gradient duration and Δ is the total diffusion time. By varying one of the experimental parameter (e.g. Δ or g) during the PFE-SE tests, the recorded signal intensity of individual NMR peaks could fitted using Equation 2.9, and the corresponding self-diffusion coefficient of the solute could be extracted. Here we also introduce two PFG pulse sequences which are frequently used in NMR diffusometry.

(a) PFG-SE

The most common PFG NMR diffusion experiment is a spin echo pulse sequence with pulse field gradient (PEG-SE) which is also used in Stejskal and Tanner's study. Monitoring of the self-diffusion in a sample is accomplished by the application of the pulsed field gradients during the dephasing and rephasing periods of a conventional Spin Echo experiment. In Figure 2.4 as a schematic picture of this pulse sequence is shown, with two field gradients of identical duration δ and strength g applied between the two RF pulses and after 180° pulse.

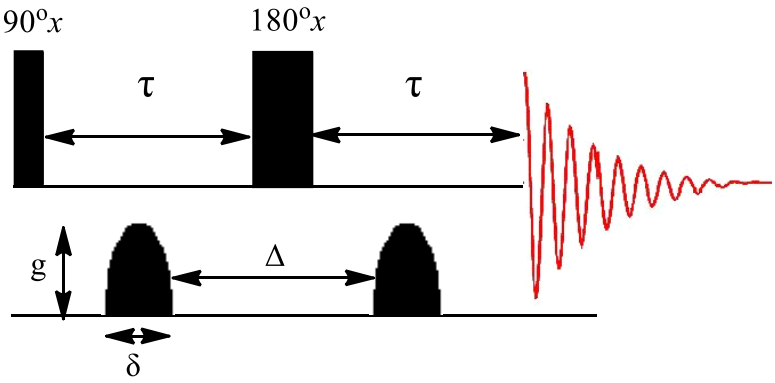

Figure 2.4 Simple illustration of PFG-SE pulse sequence.

As mentioned in the previous section, the whole diffusion process probed by the PFG-SE pulse sequence could be illustrated by Equation 2.9. However, the presence of T_2 relaxation should be properly taken into account. Therefore, Equation 2.9 should be further modified into

$$S(t) = S(0)exp\left(-\frac{2\tau}{T_2}\right)exp\left[-D\gamma^2 g^2 \delta^2 \left(\Delta - \frac{\delta}{3}\right)\right] \quad (2.10)$$

Where $exp\left(-\frac{2\tau}{T_2}\right)$ represents the spin-spin relaxation time of the interested spin systems. This term implies a limitation of PFG-SE when applied to systems with short T_2 relaxation times (e.g. polymers), since the intensity of the signal is too weak to generate a reasonable fit to the data after the diffusion period. Therefore, the PFG Stimulated Echo pulse sequence was subsequently devised to resolve this issue.

(b) PFG-STE

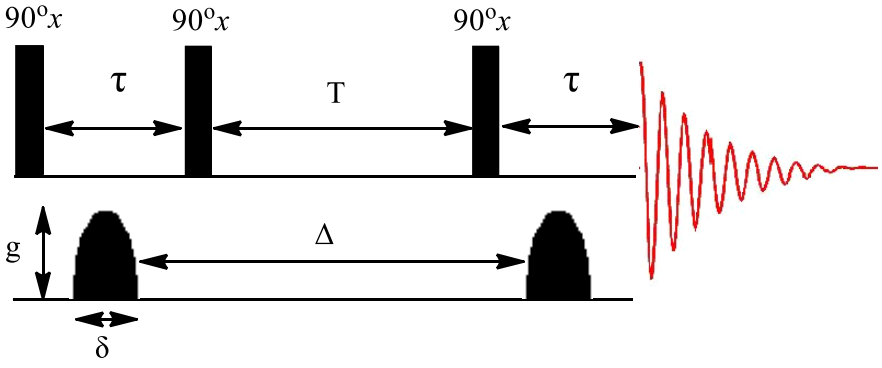

Figure 2.5 Simple illustration of PFG-STE pulse sequence.

The combination of a pulse magnetic field gradient and a sequence called stimulated echo (PFG-STE) is shown in Figure 2.5. In this case, the corresponding equation for the echo signal intensity is

$$S(t) = \frac{1}{2}S(0)exp\left(-\frac{T}{T_1}\right)exp\left(-\frac{2\tau}{T_2}\right)exp\left[-D\gamma^2 g^2\delta^2\left(\Delta - \frac{\delta}{3}\right)\right] \quad (2.11)$$

The advantage with the stimulated pulse sequence is that the effective time for T_2 relaxation, 2τ, can be made short. After the second 90° pulse and during the time T, the magnetization is along the –z, and therefore there is no T_2 relaxation. An additional advantage is that T_1 is often considerably longer in macromolecules system.[12]

2.1.3 ^{1}H Multiple-Quantum NMR Analyses

In contrast to liquids, the positions of the nuclei in solids are relatively fixed in space which leads to a static dipolar coupling constant, D_{stat}. In the case of polymers, topological restrictions of polymer networks make them behave partially solid-like, which in turn leads to a partially averaged dipolar interaction. The magnitude of these residual dipolar coupling, D_{res}, directly reflects the motion averaging of the dipolar coupling constant through conformational changes of the polymer strands. Meanwhile, the ratio between the D_{res} and D_{stat} is defined as S_b, the dynamic backbone tensor order parameter of the segments of a polymer chain[13],

$$S_b = k\frac{D_{res}}{D_{stat}} = \frac{3r^2}{5c} \quad (2.12)$$

Where r^2 is the square of the average inter-nuclear distance, and c is the network strand length. The pre-factor k takes into account that the coupling constant can also be pre-averaged by properties of the local intra-segmental spin system which are not related to conformational changes of the polymer chains.

A reliable quantitative method for the determination of homonuclear residual dipolar coupling, D_{res} in polymer networks is static ^{1}H multiple-quantum (MQ) NMR[14]. In the experiment, the coherences between two or more dipolar coupled spins are excited by RF pulses as in the normal NMR. However, only the coherences between spin states that differ by more than one unit in the magnetic quantum number are recorded. Since these coherences cannot induce a FID, they have

to be detected indirectly. There are three stages in a typical static MQ experiment, which are excitation, reconversion and acquisition. In the acquisition period the intensity related to the different MQ coherences is detected selectively by appropriate phase-cycling.

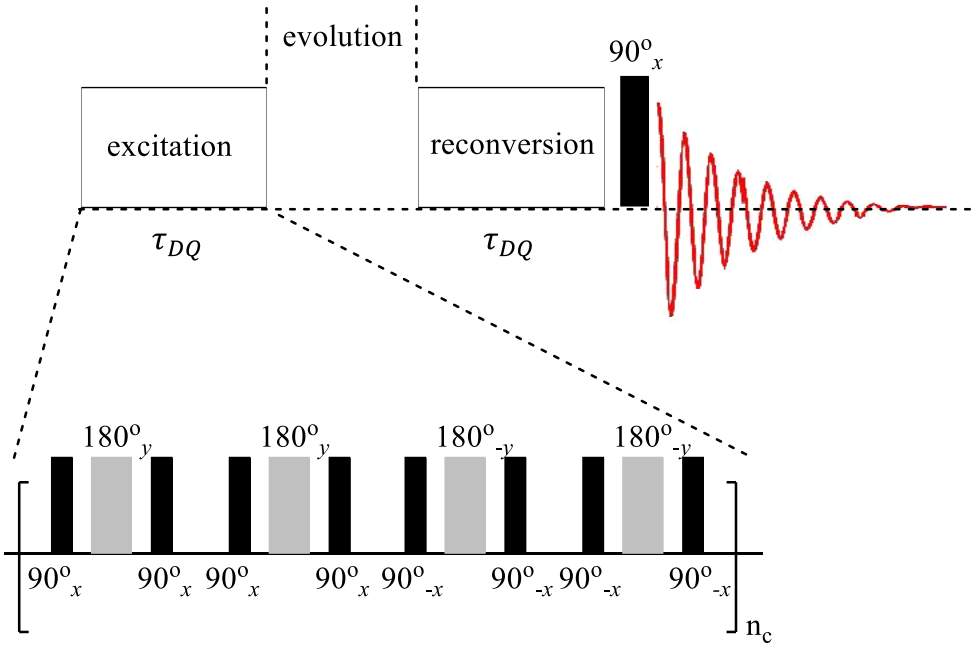

Figure. 2.6 Schematic Representation of a MQ experiment with BP MQ pulse sequence

In the case of Baum-Pines MQ pulse sequence (Figure 2.6)[15], the applied 4-step phase-cycling induces a FID containing two signal functions – the DQ buildup function $\boldsymbol{I}_{DQ}(\tau_{DQ})$ and a reference intensity function $\boldsymbol{I}_{ref}(\tau_{DQ})$. Although the former comprises all the signal from every $4n + 2$ quantum order. However, the initial slop of the curve of the DQ buildup function $\boldsymbol{I}_{DQ}(\tau_{DQ})$ is dominated by DQ coherence[15, 16]. The reference intensity, $\boldsymbol{I}_{ref}(\tau_{DQ})$ on the other hand, comprises all the contribution from every $4n$ quantum order and all the signals that were not evolved into MQ coherence.

The sum intensity, $\boldsymbol{I}_{\sum \mathrm{MQ}}(\tau_{DQ}) = \boldsymbol{I}_{ref}(\tau_{DQ}) + \boldsymbol{I}_{DQ}(\tau_{DQ})$, as well as $\boldsymbol{I}_{DQ}(\tau_{DQ})$ is subject to incoherent processes (molecular motions, e.g.). Hence, they decay over the experiment due to the apparent relaxation effect caused by incoherent processes. To remove this effect, a normalization procedure for the raw data should be carried out before the analysis. It is performed simply through a point by point division of the $\boldsymbol{I}_{DQ}(\tau_{DQ})$ by $\boldsymbol{I'}_{\sum MQ}(\tau_{DQ})$, which is $\boldsymbol{I}_{\sum MQ}(\tau_{DQ})$ after subtraction of the contribution of the isotropically mobile network components $\boldsymbol{I}_{defect}(\tau_{DQ})$. The normalized

double quantum intensity, $\boldsymbol{I}_{nDQ}(\tau_{DQ})$, is dominated by pure dipolar spin-pair interactions that are only related to the network structure.

$$\boldsymbol{I}_{nDQ}(\tau_{DQ}) = \frac{\boldsymbol{I}_{DQ}(\tau_{DQ})}{\boldsymbol{I'}_{\sum MQ}(\tau_{DQ})} = \frac{\boldsymbol{I}_{DQ}(\tau_{DQ})}{\boldsymbol{I}_{ref}(\tau_{DQ}) + \boldsymbol{I}_{DQ}(\tau_{DQ}) - \boldsymbol{I}_{defect}(\tau_{DQ})} \tag{2.13}$$

The residual dipolar coupling D_{res} is obtained by fitting the normalized buildup curve to appropriate functions. The commonly used fitting function based on a static second-order moment approximation yields an average $\overline{D_{res}}$ and is limited to the initial part of the buildup curve [13],

$$\boldsymbol{I}_{nDQ}(D_{res}, \tau_{DQ}) = 0.5\left\{1 - exp\left(-\frac{2}{5}D_{res}^2\tau_{DQ}^2\right)\right\} \tag{2.14}$$

Hence, by analyzing the $\overline{D_{res}}$ and its corresponding distribution which is encoded in the curve of the buildup function, one can determine the structural properties of the polymer networks

2.1.4 Solid State Cross Polarization Magic Angle Spinning (CP-MAS) NMR Analyses

The majority of the techniques mentioned above are used to detect ^{1}H. When it comes to observing dilute spins (e.g. ^{13}C), a number of problems occur. Most notable are poor signal-to-noise ratio and long T_1 relaxation times (which in turn means long measurement times). Polarization transfer techniques were developed for solid state NMR to counter these problems. In these experiments, a increased spin polarization for detection is created by the flow of spin order from a source reservoir of spins I (e.g. ^{1}H) which can be easily polarized, to a target reservoir of spins X (dilute spins). The best known example for polarization transfer experiment is the cross polarization (CP) technique established by Pines et al.[17]. As shown in Figure 2.7, CP technique uses a spin locking pulse sequence to transform the Zeeman spin order of an ensemble of abundant spins into a Zeeman order in the rotating frame and, afterwards initiates a rapid 'thermodynamic exchange' between this spin order and the dilute spins. This exchange is achieved by matching the energy quanta involved in spin flip-flop transitions which fulfills the Hartmann-Hahn condition for the B_1 field strengths [18]:

$$\gamma^{1H} B_1^{1H} = \gamma^X B_1^X \tag{2.15}$$

The magnitude of the resulting dilute spin X magnetization is proportional to that of the ^{1}H reservoir that polarized it. Therefore, dilute spins coupled to more ^{1}H nuclei are more strongly

enhanced. The gain of magnetization by CP technique relative to that of the single pulse excitation can be estimated as γ^{1H}/γ^{X}. The other advantage of using CP technique is that the recycle delays, and thus the measuring times, are reduced due to the shorter T_1 relaxation times of ^{1}H. This is the direct consequence of the ^{1}H spin diffusion which transfer its relaxation time to the rest of the system.

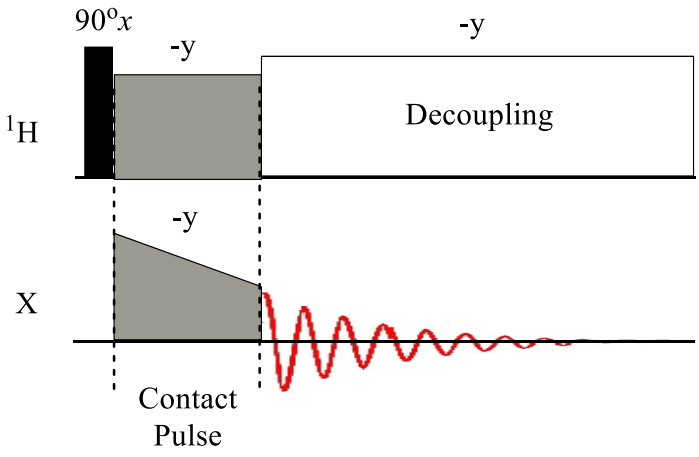

Figure 2.7 Simple illustration of cross polarization pulse sequence.

The major difficulty for achieving good results with the CP technique is the precise amplitude adjustment of the two *RF* fields which have to fulfill the Hartmann-Hahn condition. This problem becomes more severe when the difference between the gyromagnetic ratios of the two nuclei increases.

2.2 Thermal Analyses

As one of the oldest analytical techniques, thermal analysis has been applied into the characterization of various materials ranging from synthetic polymers[19] to food products[20]. It comprises a family of measuring techniques including differential scanning calorimetry (DSC), thermogravimetric analysis (TGA), dynamic mechanical analysis (DMA) and others. A common feature for all these techniques is that they measure a material's response to being heated or cooled. The purpose of these thermal studies is to establish a connection between temperature and specific physical properties of materials. In the field of polymer science thermal analyses is used not only for measuring the actual physical properties of materials but also for clarifying their thermal and mechanical histories. In this thesis, two thermal analysis techniques – DSC and DMA are used to determine the glass transition temperature (T_g) and crosslink density (M_c).

2.2.1 Differential Scanning Calorimetry

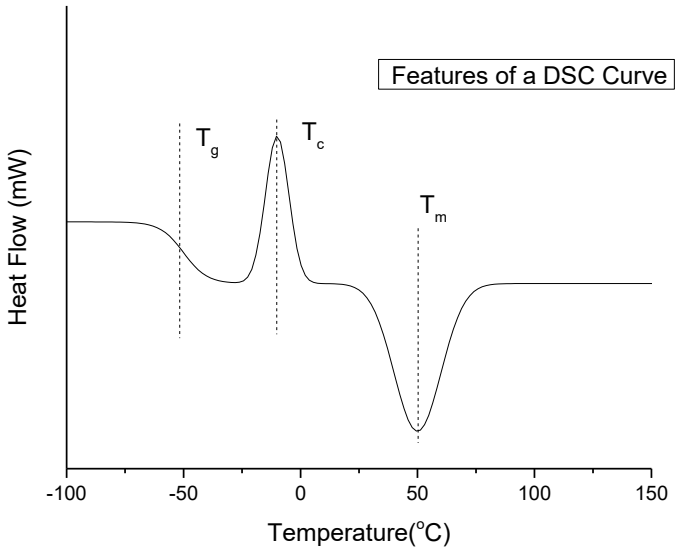

Figure. 2.8 Typical features of a DSC thermogram.

In DSC, the heat flow rate difference between a substance and a reference is measured as a function of temperature, while the sample as well as the reference is subjected to a controlled temperature program. Although it could be further divided into *power compensation DSC*, and *heat flux DSC*[21], the shared feature is that they can both be used to determine a range of characteristic temperatures,

the heat capacity, and the heat fusion as well as the various thermal parameters of chemical reactions. The DSC measurement signal is the energy absorbed or released by the sample in milliwatts.

A typical heating thermogram (see Figure 2.8) for a polymer material shows 3 major features. The small step in the left hand side indicates the glass transition process, where T_g is defined as the point of inflexion. With increasing temperature the polymer undergoes crystallization which is an endothermic process. This results in a positive peak in the thermogram with T_c (crystallization point) as its maximum. Finally, when the polymer reaches its melting point (T_m), an exothermic peak appears in the thermogram.

2.2.2 Dynamic Mechanical Analyses

Due to their unusual viscoelasticity, polymeric materials often display mechanical behavior with both solid and liquid characteristics. Among all the different methods for viscoelastic properties characterization, dynamic mechanical analysis (DMA) is the most popular due to its applicability in both polymer solids and liquids.

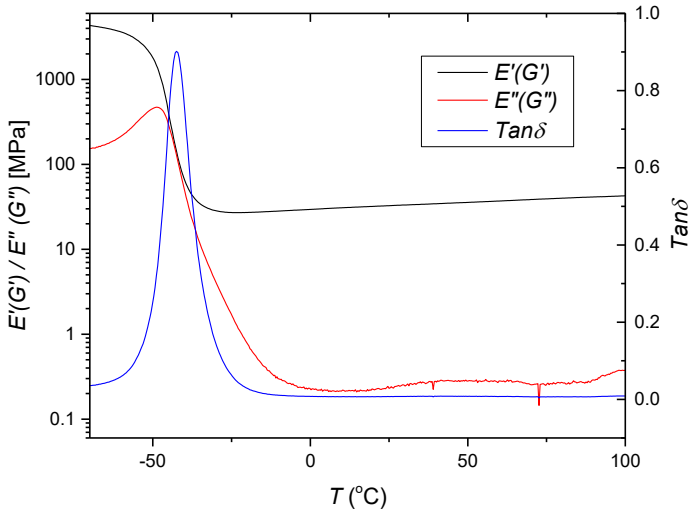

Figure. 2.9 Typical features of a DMA thermogram.

In DMA, the sample is subjected to a sinusoidal mechanical stress. The force amplitude, displacement (deformation) amplitude, and phase shift are determined as a function of temperature or frequency. DMA allows you to detect thermal effects based on changes in the modulus or

damping behavior. The most important results are temperatures that characterize a thermal effect, the loss angle (the phase shift), the mechanical loss factor (the tangent of the phase shift), the elastic modulus or its components (the storage and loss moduli), and the shear modulus or its components (the storage and loss moduli).

References

1. G. n. t. María, P. S. Belton, G. A. Webb, Royal Society of Chemistry (Great Britain), *Magnetic resonance in food science : challenges in a changing world*. Special publication (Royal Society of Chemistry, Cambridge, UK, 2009), pp. ix, 260 p.
2. J. A. Iggo, *NMR spectroscopy in inorganic chemistry*. Oxford chemistry primers (Oxford University Press, Oxford ; New York, 1999), pp. 87 p.
3. C. A. Schalley, *Analytical methods in supramolecular chemistry*. (Wiley-VCH, Weinheim, ed. 2nd completely rev. and enlarged, 2012).
4. P. Miâeville, Tháese Ecole polytechnique fâedâerale de Lausanne EPFL, no 5229 (2011), Programme doctoral Chimie et Gâenie chimique, Facultâe des sciences de base SB, Institut des sciences et ingâenierie chimiques ISIC (Laboratoire de râesonance magnâetique biomolâeculaire LRMB) Dir Geoffrey Bodenhausen, Sandrine Gerber, EPFL (2011).
5. P. Hunkeler, Masterarbeit, ETH Zurich, 2009, ETH (2009).
6. E. L. Hahn, Spin Echoes. *Phys Rev* **77**, 746 (1950).
7. F. J. Sevilla, V. M. Kenkre, Theory of the spin echo signal in NMR microscopy: analytic solutions of a generalized Torrey-Bloch equation. *J Phys-Condens Mat* **19**, (Feb 14, 2007).
8. G. H. Sørland, *Dynamic pulsed-field-gradient NMR*. Springer Series in Chemical Physics, , pp. 1 online resource (xiii, 354 pages), 2014.
9. D. I. Kopelevich, H. C. Chang, Non-equilibrium transport in and on condensed matters: Effects of lattice vibration and deterministic chaos. *Mol Simulat* **30**, 159 (Feb-Mar, 2004).
10. E. O. Stejskal, J. E. Tanner, Spin Diffusion Measurements: Spin Echoes in the Presence of a Time-Dependent Field Gradient. *J Chem Phys* **42**, 288 (1965).
11. H. C. Torrey, Bloch Equations with Diffusion Terms. *Phys Rev* **104**, 563 (1956).
12. V. I. Bakhmutov, *Practical NMR relaxation for chemists*. (Wiley, Chichester, West Sussex, England ; Hoboken, NJ, 2004), pp. xiv, 202 p.
13. K. Saalwachter, Proton multiple-quantum NMR for the study of chain dynamics and structural constraints in polymeric soft materials. *Prog Nucl Mag Res Sp* **51**, 1 (Aug 30, 2007).
14. K. Saalwachter, Robust NMR Approaches for the Determination of Homonuclear Dipole-Dipole Coupling Constants in Studies of Solid Materials and Biomolecules. *Chemphyschem : a European journal of chemical physics and physical chemistry* **14**, 3000 (Sep 16, 2013).
15. J. Baum, A. Pines, Nmr-Studies of Clustering in Solids. *J Am Chem Soc* **108**, 7447 (Nov 26, 1986).
16. K. Saalwachter *et al.*, H-1 multiple-quantum nuclear magnetic resonance investigations of molecular order distributions in poly(dimethylsiloxane) networks: Evidence for a linear mixing law in bimodal systems. *J Chem Phys* **119**, 3468 (Aug 8, 2003).
17. A. Pines, J. S. Waugh, M. G. Gibby, Proton-Enhanced Nuclear Induction Spectroscopy - Method for High-Resolution Nmr of Dilute Spins in Solids. *J Chem Phys* **56**, 1776 (1972).
18. S. R. Hartmann, E. L. Hahn, Nuclear Double Resonance in the Rotating Frame. *Phys Rev* **128**, 2042 (1962).
19. J. D. Menczel, R. B. Prime, *Thermal analysis of polymers : fundamentals and applications*. (John Wiley, Hoboken, N.J., 2009), pp. x, 688 p.
20. V. R. Harwalkar, C. Y. Ma, *Thermal analysis of foods*. Elsevier applied food science series (Elsevier Applied Science; Sole distributor in USA and Canada, Elsevier Science Pub. Co., London ; New York, 1990), pp. xi, 362 p.
21. M. E. Brown, *Introduction to thermal analysis : techniques and applications*. Hot topics in thermal analysis and calorimetry (Kluwer Academic Publishers, Dordrecht ; Boston, ed. 2nd, 2001), pp. xi, 264 p.

Chapter III

Network structure in acrylate systems: the effect of junction topology on crosslink density and macroscopic gel properties

3.1 INTRODUCTION

It is well established that the microscopic network structure and dynamics of hydrated polymer hydrogels largely determine their key properties for biomedical applications, namely water permeability, elasticity, strength and lifetime.[1] However, efforts over several decades to develop generally applicable models for microscale polymer dynamics have produced mixed results; in many cases they are only applicable to the simplest homopolymers. Hence the factors determining how bulk properties emerge from the nanoscale order in applications-relevant polymer systems remains unclear, and this represents a significant barrier to rational design of next-generation hydrogels.

From an industrial perspective, UV-curing is an ideal approach to on-demand crosslinking/polymerization, which can be implemented into various material-processing procedures at production scale.[2] It offers significant advantages over other alternatives, including being mainly solvent-free, rapid and easy to implement into new processes. However, materials generated by this technique are often intrinsically heterogeneous, which renders the direct application of rubber elasticity models impossible. Detailed studies of UV-cured co-polymerized hydrogls, which offer some control over the type and number of network junctions, are relevant to understanding and tuning the formulation of responsive biocompatible systems for tissue engineering. They are also of fundamental relevance as they provide a more realistic system for the development and testing of network models.

A wide range of techniques have been used to characterize network structures.[3] Among them, mechanical analyses and equilibrium swelling tests are the most frequently used methods to determine volume average network density. These approaches can provide average network strand lengths for deficit-free networks, through application of an appropriate model. Several rubber elasticity theories have been developed[4], which differ in the description of the response of network junctions to applied macroscopic strain. In the affine model proposed by Flory, it is assumed that the deformation of each individual polymer chain in the network is the same as the macroscopic deformation, and all the network junctions do not fluctuate around their position upon deformation.[5] On the other hand, in the phantom model the crosslinks are considered to fluctuate freely about an average position with restrictions imposed by their neighboring chains.[6] In this

picture, the macroscopic modulus depends on the chemical functionality of network junctions. Note that both models are based on Gaussian chain statistics, and hence are only applicable to network chains containing more than 50-100 rotatable back-bone bonds. In recent decades some progress has been made in developing improved models. For example, the slip-link model, which suggests restricted fluctuation of network junctions,[7, 8] predicts modulus values that are intermediate between those from the affine and phantom models.

However, these approaches cannot provide information about the distribution of the length of network chains, which is essential to characterize the heterogeneities of the network, or about network defects or temporary physical junctions (the role of chain entanglements in the elasticity is often an unresolved key issue). Hence, direct application of these models to heterogeneous networks or to networks with various types of network defects is still under discussion, in which microscopic properties of local chain motions are playing an important role.

Experimentally it has been found that the nature of network junctions also affects network elasticity as was shown for the polyacrylate network.[9, 10] In the case of polyethylene glycol (PEG)-based acrylate co-polymer network[10], the interpretation of DMA and ^{1}H NMR T_2 relaxation experiments, with the assumption of Gaussian chain statistics, predicted a molecular mass of network chains, M_c, less than half of that of the oligomers used for network synthesis.[10] In equilibrium swelling studies of similar networks, interpretation using the Flory-Rehner relation provided smaller M_c values with larger deviation for shorter diacrylate chain length[9]. Small-angle X-ray scattering (SAXS)[11] and atomic force microscopy (AFM)[12] studies suggested the presence of rod-like crosslink clusters, or 'microgel domains' which may contribute to large network heterogeneity, and give rise to non-Gaussian behavior of the network chains. A recent small-angle neutron scattering (SANS) study[13] even went further to propose a star-like chain arrangement in order to explain the complicated heterogeneity inside this kind of networks.

UV-cured acrylate networks formed upon photo-initiated crosslinking polymerization of diacrylates, exhibit substantially different topology from other types of networks, with long acrylic chains forming zip-like network junctions and network chains connected to each tertiary carbon atom of the acrylic chain. Interconnectivity of each acrylic chain with the neighboring ones by PEG-chains significantly decreases both the number of chain conformations that can be adopted,

and the rates of rotational and translational dynamics. In essence the multi-functional junctions can be considered as largely immobilized rods (vertical strands shown in black in the inset to Figure 3.1a) interpenetrating through network chains, with the conformational freedom of the latter potentially restricted. Despite numerous studies into acrylic networks and their wide application areas, there is not enough understanding of the role of their particular topology on functional properties or indeed of their network structure, as was shown by previous studies.[9, 10]

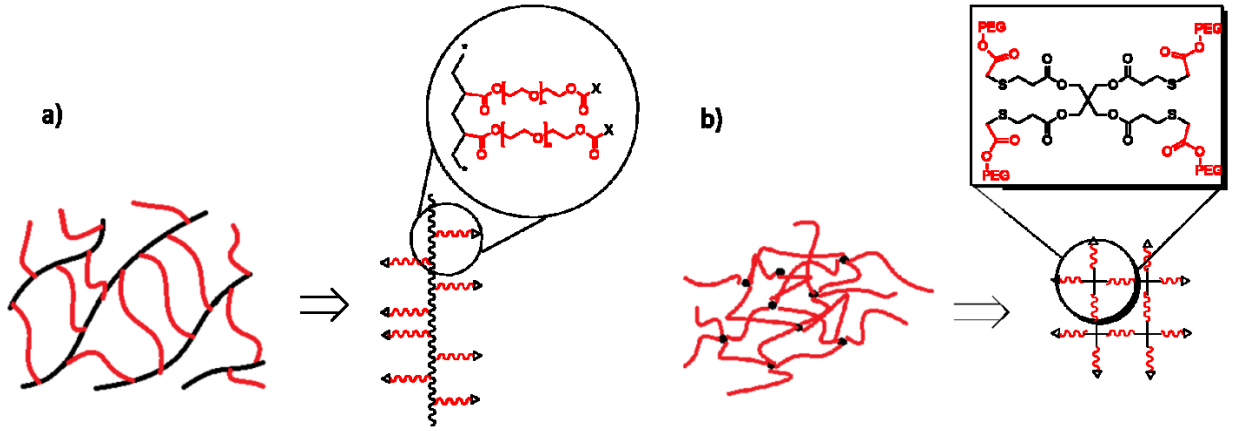

Figure 3.1. Suggested molecular structure of the networks; a) zip-like junction network (PEGDA-HA); b) point-like junction network (PEGDA-PETM).

To investigate the origin of the unusual behavior of diacrylate networks, a series of hydrogels was prepared by varying the weight fraction of hexylacrylate (ω_{HA}) to PEG-700-diacrylate (ω_{PEGDA}). In addition, samples with point-like network junctions[14] were prepared using a tetra-functional thiol via free-radical thiol-ene reaction. Primary characterization of these networks involved; (i) chemistry of the crosslinked state analysed by solid state NMR and FTIR; (ii) solution state NMR characterization of the residual sol fractions of synthesized networks; (iii) average molar mass analysis of acrylate chains by chromatography; (iv) dynamic mechanical thermal analysis (DMA) of the mechanical properties of these networks; (v) ^{1}H NMR T_2 relaxometry analysis of the network dynamics; (vi) DQ NMR characterization of the detailed network dynamics. This work is based on a collaboration with Dr, Walter Chassé from the Group of Prof. Arno Kentgens in Nijmegen University. All the DQ analyses were performed by Dr, Walter Chassé , he also made a considerable contribution to the discussion part.

Key aspects of this study include the application of the chemical-shift-specific Double Quantum NMR analysis[15] into the study of UV-cured PEG-DA systems for the first time. This approach allows determination of the effect of the mono-functional acrylate on PEGDA network dynamics. By relating the extracted residual dipolar coupling constant, D_{res}, to the mean molecular weight, M_w, of hydrolyzed polyacrylic acid backbone, obtained from chromatographic analysis, new insights into the network local chain dynamic can be obtained as compared to conventional volume average technique like DMA. Finally, with the additional analysis of networks with point-like junctions, the discrepancy between the theoretically predicted mean crosslink density and that calculated from the experimental data is discussed in relation to the influence of the type of network junctions on viscoelasticity of diacrylate networks.

3.2 EXPERIMENTAL PART

Sample Preparation: Polyethylene glycol-700-diacrylate (PEGDA), Hexyl acrylate (HA), Pentaerythritol tetrakis(3-mercaptopropionate) (PETM), Photo-initiator: 2-Hydroxy-2-methylpropiophenone (HMPP), Diphenyl(2,4,6-trimethylbenzyol) phosphine oxide (DPTMBPO) were used for synthesis of networks. All the chemicals were obtained from Sigma Aldrich, and used without any further purification.

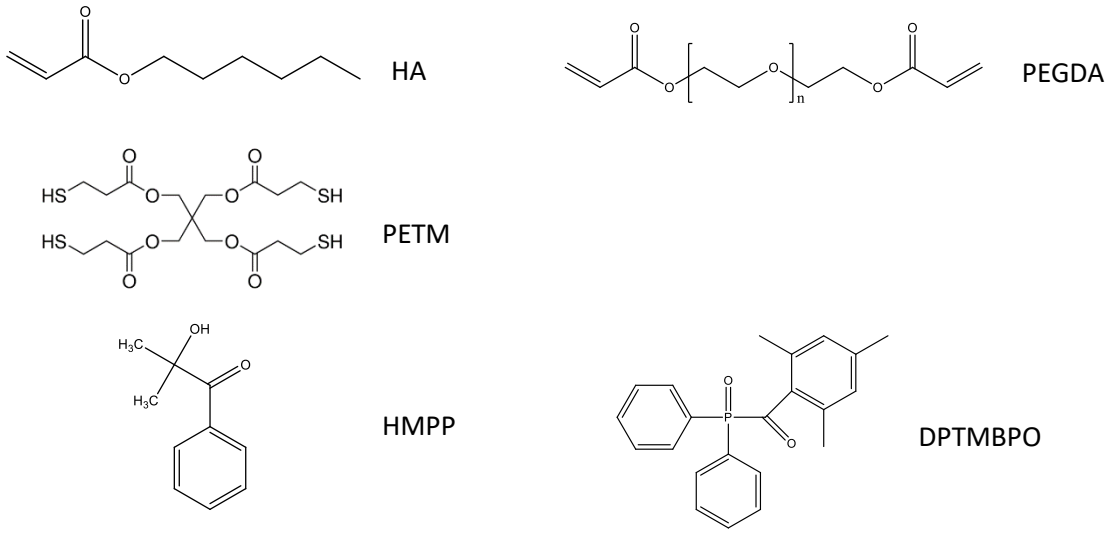

Figure 3.2 Chemical structures of monomers/crosslinkers used in the study.

Networks were prepared by UV-curing of the chemicals with the proportion described in Table 3.1. (Photo initiator: 20 µL 2-Hydroxy-2-methylpropiophenone, and 10-20 mg Dipheyl(2,4,6-

trimethylbenzyol) phosphine oxide in 5 g mixture). The formulation was poured into a petri dish, and then the petri dish was passed through the UV-rig (Heraeus Noblelight Fusion UV Inc.'s F300S model, with I300MB irradiator which has a lamp power of 300w/in (120w/cm), 1800 watts total) 30 times. Afterwards the cured film was inverted, and was then passed through the UV-rig a further 30 times. The rim of the resulting film was cut off, and the remaining part with a thickness around 1mm was used for all the tests. All the films have been found no further change in IR spectra after passing through the UV-rig for multiply times. One side curing also was performed, no distinguishable feature could be found in IR after films been passing through UV-rig over 30 times.

The double bond conversions of the films (which describes the completeness of crosslinking reaction) was measured by FTIR, and molecular weight of the hydrolyzed acrylate backbone chains was determined by chromatographic analyses. Results of network characterization are summarized in Table 3.1.

Solid State NMR. ^{13}C NMR spectra were recorded on a Bruker Avance III 600 MHz spectrometer equipped with a solid standard-bore Magic Angle Spinning (MAS) probe. A 4 mm rotor was used at a MAS rate of 12 kHz. Single pulse excitation (SPE) and cross-polarization (CP) pulse sequences were used in this study. The 90° pulse length was calibrated to 2 μs. The spectra were recorded with two different cross-polarization time (τ_{cp}) of 0.5 ms and 10 ms, in order to distinguish between the least and the most mobile chain segments, respectively.

The ^{1}H double-quantum (DQ) NMR experiments were carried out on a VNMRS 850 operating at a ^{1}H Larmor frequency of 849.71 MHz equipped with a 1.6 mm triple resonance probe. The MAS frequency was set to 40 kHz and the sample temperature to 50°C. The 90° pulse length was calibrated to 2 μs. The data for all network samples was acquired using a recently published improved version of the Back-to-Back (BaBa) sequence, BaBa-xy16, for broadband homonuclear DQ recoupling.[16] This work was done by Dr. Walter Chassé in Prof. Dr. Arno Kentgens' group in Nijmegen in the Netherlands.

The ^{1}H transverse magnetization relaxation (T_2 relaxation) times of these networks were measured on a Bruker Minispec MQ20 spectrometer operating at 20 MHz. The T_2 relaxation decay was measured at 50°C with the Hahn-echo (HE) pulse sequence, $90_x^o - \tau_{HE} - 180_y^o - \tau_{HE} -$

(acquisition), where $\tau_{HE} \geq 35$ µs. An echo signal is formed after the second pulse in the HE with a maximum at time $t = 2\tau_{HE}$ after the first 90° pulse. By varying τ_{HE}, the amplitude of the transverse magnetization, $A(t)$, is measured as a function of time t. The decay curves are analyzed in terms of the population average transverse relaxation time $T_{2,av}$.

Mechanical Measurements. The glass transition temperature and the storage modulus were measured with TA DMA Q800 Analyzer at a frequency of 1 Hz. Test samples with 5 mm width and 15 mm length were cut out from the cured films. The thickness of the test bar was measured with a calibrated micrometer. The DMA test were started from -90 ºC and the temperature was gradually increased to 150 ºC with a ramp speed of 3 ºC/min.

3.3 RESULTS:

Network Structure Analysis. To ensure that the expected network structures was formed during the polymerization reactions, ^{13}C solid state NMR spectra and IR spectra were recorded for all the samples, and ^{1}H solution state NMR analysis of the same samples was used for chemical structure characterization of the sol fraction in the network.

(a) PEGDA-HA network

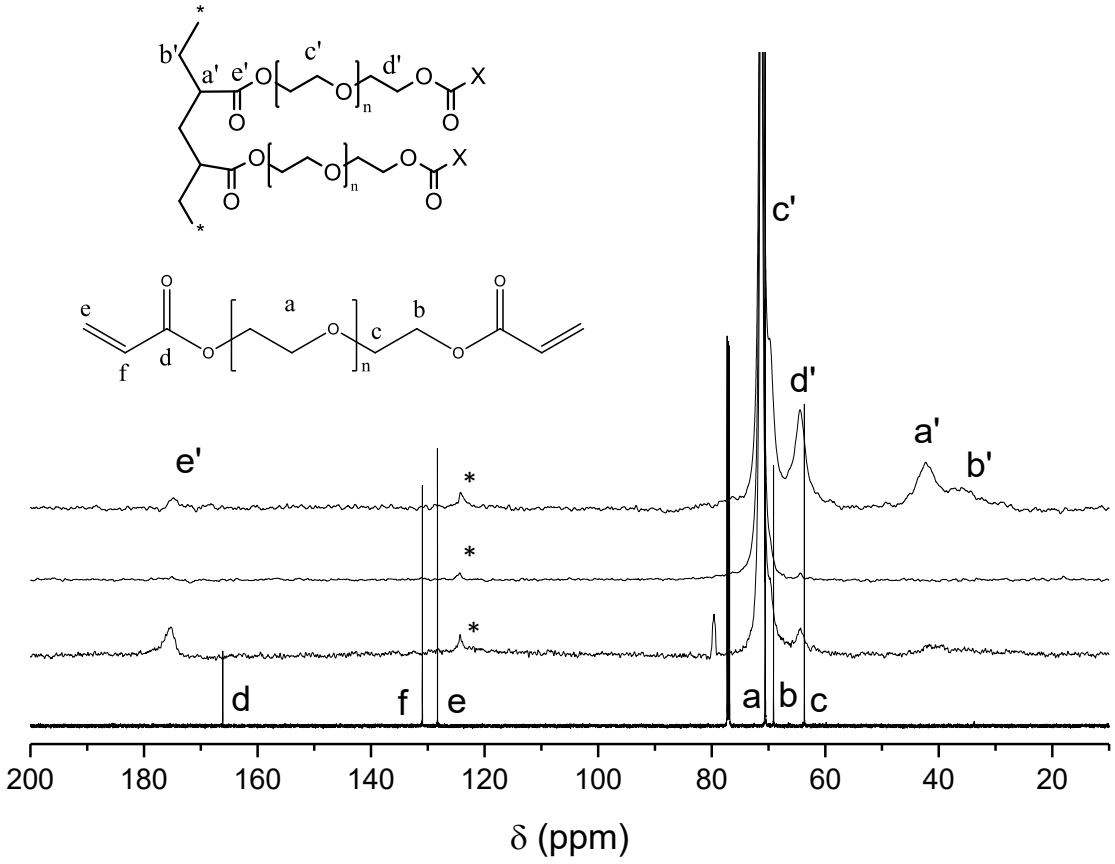

Figure 3.3: ^{13}C MAS spectrum for uncured (bottom) and ^{13}C solution state spectrum of cured (second from bottom) sample 1 network (100% PEGDA-700), and ^{13}C CP-MAS spectrum for sample 1 with cross-polarization time τ_{cp} at 10ms (third), and 0.5ms (top). Assignments: **Bottom:** 166.5 ppm: carbonyl carbon in PEGDA; 131.2 ppm: =CH-C(O)-; 128.5ppm: CH_2=CH-; 79.5 ppm: $CDCl_3$; 71.5 ppm: -OCH_2 from PEG; 69.8 ppm and 65.5 ppm: -OCH_2- carbons in α and β positions to carbonyl carbon atom at PEGDA chain ends respectively; **Second:** 176.7 ppm: carbonyl carbon in polyacrylate; 79.5 ppm: $CDCl_3$; 71.5 ppm: -OCH_2 from PEG; 69.8 ppm and 65.5 ppm: -OCH_2- carbons in α and β positions to carbonyl carbon atom at PEGDA chain ends respectively; **Third**: 71.5 ppm: -OCH_2 from PEG; 69.8 ppm and 65.5 ppm: -OCH_2- carbons in α and β positions to carbonyl carbon atom at PEGDA chain ends respectively. (14.6 T, 8 kHz rotor spinning speed, * represents spinning side band)

IR characterization and deconvolution of the acrylate C-H deformation band at 810 cm^{-1} for both cured and uncured samples have confirmed high conversion rates. [see Figure 3.4 and Table 3.1]

The chemical structure of all the samples was analyzed by ^{13}C solid state NMR to ensure that no side reactions occurred during the curing procedure (Figure 3.3). All the ^{13}C resonances of the network are broadened due to restricted chain mobility. The shift of the resonance at 165 - 178 ppm upon curing is due to the polyacrylate radical polymerization which breaks the conjugated acrylate double bond system. The residual peak observed at 126 ppm, which is originated from spinning side band of PEG main chain peak (-OCH_2: 71.5 ppm), confirmed high conversion of the acrylate double bond in cured networks. The broad resonance at 32-48 ppm originates from CH_2 and CH carbon atoms of the polyacrylate chains.

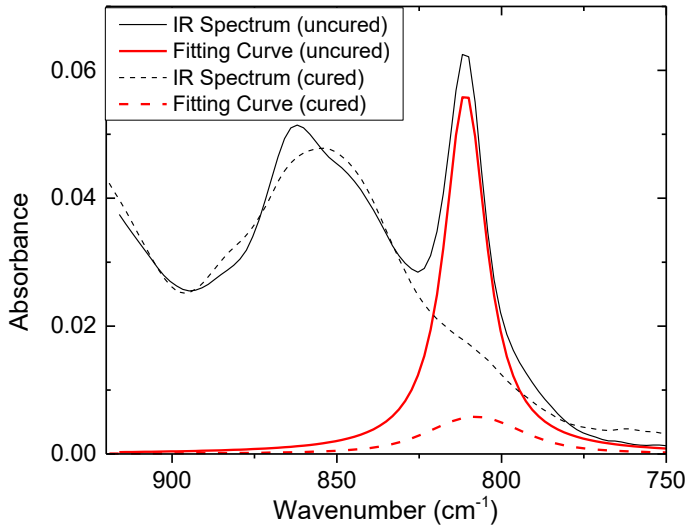

Figure 3.4 IR spectrum of acrylate C-H deformation band at 810 cm^{-1} for uncured and cured sample 1 (PEGDA:HA=100:0)

In order to determine possible side reactions during curing, ^{13}C CP-MAS with varied cross-polarization time (τ_{CP}) were recorded. At long τ_{CP}, the resonances' intensities of the more mobile chain segments are enhanced, while at short τ_{CP}, the integral intensity of the least mobile chain segments at crosslinked junction dominate the spectrum, see Figure 3.3. This is the case for instance for the two broader peaks at 36 and 44 ppm that are more prominent for shorter cp-contact. This proves that these resonances come from the polyacrylate backbone bonds which form the less mobile network junctions.

With similar analyses, it was found that the double bond conversion is high for all the PEGDA-HA samples. Any side reactions are minor, if they occur at all.

(b) PEGDA-PETM (point-like junction) networks

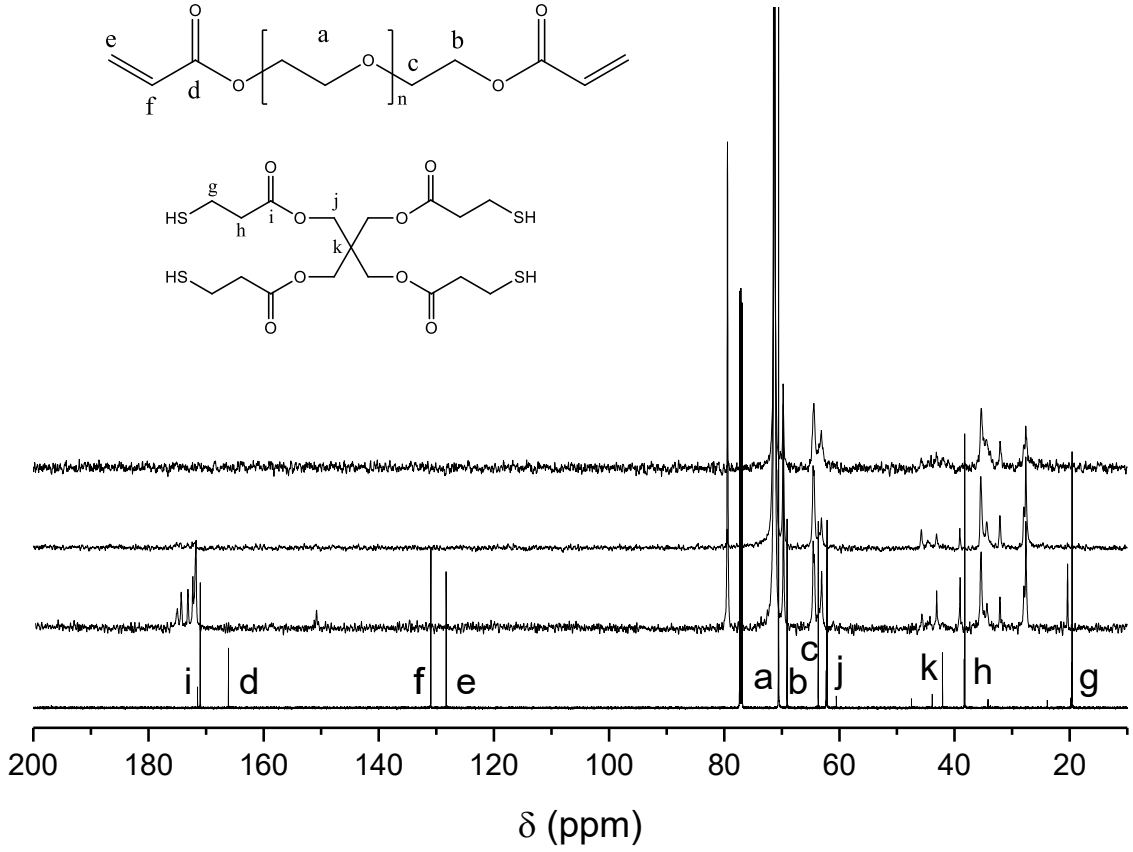

Figure 3.5. ^{13}C MAS spectrum for uncured (bottom) and ^{13}C solution state spectrum of cured (second from bottom) sample 7 (PEGDA+PETM) network, and ^{13}C CP-MAS spectrum for cured sample 7 network with cross-polarization time τ_{cp} at 10ms (third), and 0.5ms (top).Assignments: **Bottom:** 171.8 ppm: carbonyl carbon in PETM; 166.5 ppm: carbonyl carbon in PEGDA; 131.2 ppm: =CH-C(O)- in PEGDA; 128.5ppm: CH_2=CH- in PEGDA; 79.5 ppm: $CDCl_3$; 71.5 ppm: -OCH_2 from PEG; 69.8 ppm and 65.5 ppm: -OCH_2- carbons in α and β positions to carbonyl carbon atom at PEGDA chain ends respectively; 63.8 ppm: -OCH_2 in PETM; 42.3 ppm: quaternary carbon in PETM; 38.5ppm: -CH_2-CH_2-SH; 19.8 ppm: -CH_2-SH; **Top:** 35.8 ppm: -CH-CH_2-S- of newly formed bond between PEGDA and PETM; 28.8 ppm: -CH_2-S- of newly formed bond between PEGDA and PETM. (14.6 T, 8 kHz rotor spinning speed)

^{13}C MAS NMR analyses for these samples were performed in a similar way (Figure 3.5). The double bond conversion of this network is very high, since no chemical shift around 130 ppm is observed in the spectrum of the cured sample. Newly formed thiol-ene bonds give rise to two new peaks at 35.8 ppm and 28.8 ppm which are corresponding to -CH_2CHS- and $CH(S)CH_2$- carbon atoms respectively. However due to the complex nature of free-radical thiol-ene reaction, different termination mechanisms results in several branched by-products with similar chemical shifts[17] at around 30 ppm. ^{13}C CP-MAS analysis shows two broad resonances at around 36 and 44 ppm arising from the polyacrylate backbone for which the intensity is not significantly higher at reduced τ_{CP}. This strongly suggests the absence of zip-like topology in the PEGDA-PETM network. High acrylate double bond conversion is observed for this network by FTIR analysis too (Figure 3.6). However, the complicated nature of thiol-ene reaction[18] again precludes quantitative analysis.

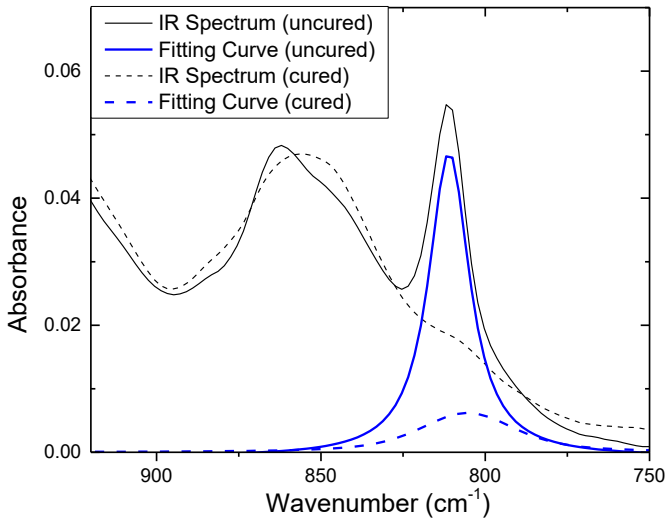

Figure 3.6 IR spectrum (with its deconvolution) of acrylate C-H deformation band at 810 cm^{-1} for uncured and cured sample 7 (PEGDA:PETM=74:26)

Solution State NMR Analyses of Hydrogel Extractable. As shown in the spectrum of the extracts, Fig. 3.7, the solution state ^1H NMR analysis shows that no detectable amount of extractable residual presented in the network. Meanwhile, due to the hydrophilic nature of PEG, the gel network absorbs water (1.56 ppm) and EtOH (1.25 ppm, t; 3.72 ppm, q, impurity in the $CHCl_3$), meanwhile, the presence of the photoinitiators (2-Hydroxy-2-methylpropiophenone, 1.42ppm;

Dipheyl(2,4,6-trimethylbenzyol) phosphine oxide, 2.18ppm) to certain extent demonstrate that only insignificant oxygen inhibition reaction happened if there is any at all. The peak at 3.68 ppm belongs to the main chain of the residual amount of PEGDA oligomer. However, with increasing mono-acrylate fraction, an increase in the amount (5 w%) of oligomers in the extract is observed. Since the PEGDA main chain peak (3.68 ppm) is considerably weaker than those assigned to HA (0.91 ppm: $-CH_3$; 1.33 ppm: $-(CH_2)_3-$; 1.64 ppm $-CH_2-CH_2-O$; 1.91 ppm: $-CH_2-$(backbone); 2.31 ppm: -C(C)H-; 4.08 ppm: $-CH_2-O$), as shown in Fig. 3.7, hence the oligomers are predominantly composed of HA. The presence of some HA outside the network structure, as oligomeric loop or chains, is consistent with the formation of defects during UV-curing procedure.

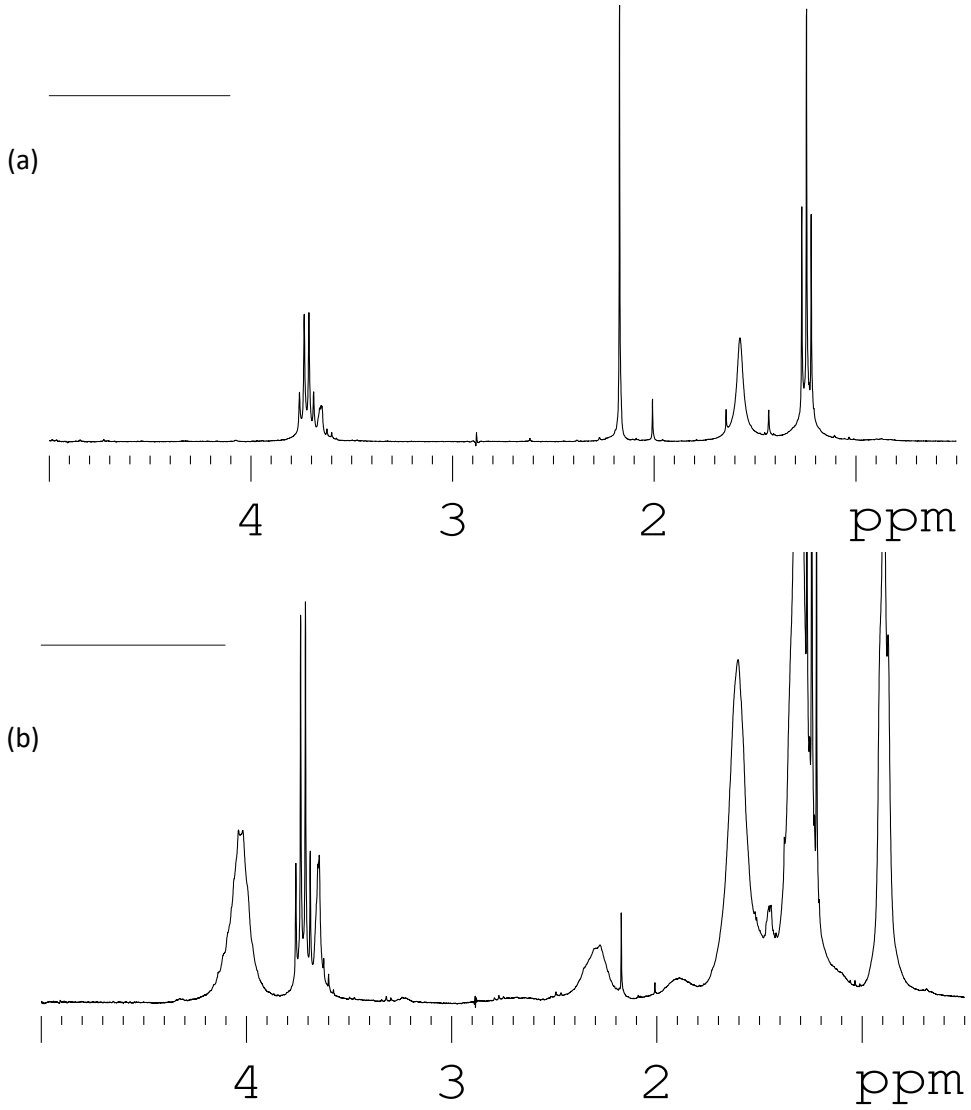

Figure 3.7. ^1H NMR spectrum of the extracts from (a) sample 1 (HA/PEGDA=0/100) and (b) sample 6 (HA/PEGDA=90/10).

Chromatographic analysis of hydrolyzed networks. The molecular weight distribution (M_w, M_n) of the acrylate backbone chains is a characteristic parameter of UV-cured PEGDA-HA networks.[19] The PAA component of the different hydrolysates were characterized to provide the M_w, M_n and PDI values shown in Table 3.1. PEG was measured with MS detection, assuming equal MS sensitivity; PEG has a M_n value of 488 Da.

Sample No.	w_{HA} %	PEGDA:HA (molar ratio)	Conversion (%)	PAA			T_2 relaxometery		DMA	
				M_n (Da)	PDI	n(PAA)	$T_{2,av}$ [µs]	$T_{2,av}^{sw}$ [µs]	T_g[K]	$E'[MPa]$
1	0	1 : 0	94±5	10.8	2.3	150	137.5	156.5	241.5	32.54
2	10	1 : 0.5	94±5	9.7	2.6	135	138.3	170.7	238.2	26.88
3	30	1 : 1.02	97±5	11.1	2.2	154	139.7	194.7	236.6	19.23
4	50	1 : 4.48	91±5	12.3	2.0	171	181.5	254.2	233.2	12.21
5	70	1 : 10.5	94±5	10.2	2.3	142	252.1	396.0	228.3	5.07
6	90	1 : 40.3	93±5	10.6	2.2	147	605.7	916.1	227.5	1.31

Sample No.	ω_{PETM} %	PEGDA:PETM (molar ratio)	Conversion (%)	T_2 relaxometery		DMA	
				$T_{2,av}$ [µs]	$T_{2,av}^{sw}$ [µs]	T_g[K]	$E'[MPa]$
7	25.9	1 : 0.5	91±5	378.5	394.1	237.8	7.90

Table 3.1. Sample formulation and results of network characterization by FTIR, chromatography, T_2 relaxometry and mechanical analyses.

The M_w and M_n of the PAA backbone chains appear to be independent of the concentration of di-functional monomer. In general, these value depend on the polymerization rate and on the bimolecular termination rate[20], which is probably similar for the different samples.

Network Density Analyses by Mechanical Experiments. By measuring the strain response to the application of an oscillating stress to the sample, dynamic mechanical analysis (DMA) can provide knowledge about the relationship between the various different viscoelastic parameters, *e.g.* storage and loss moduli, and the mechanical damping parameter ($tan\,\delta$).

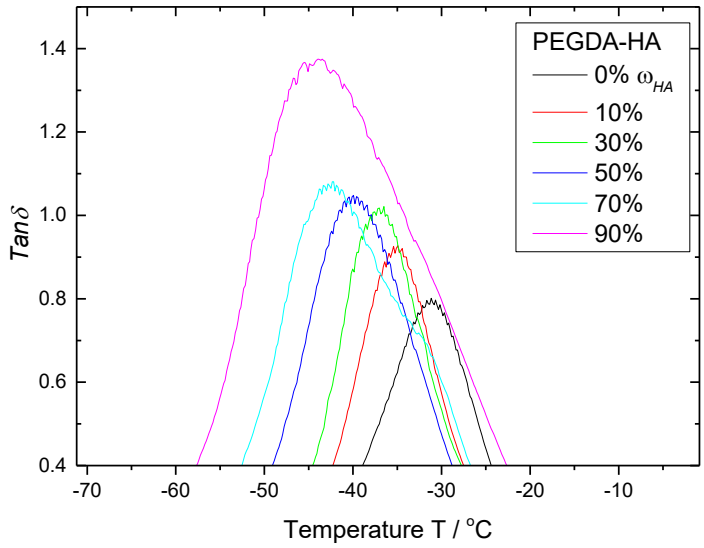

Figure 3.8 Tanδ curves of PEGDA-HA networks from DMA analyses

In this study, the glass transition temperature T_g of the network was determined from the temperature at the maximum of $tan\,\delta$. (See Figure 3.8) Since T_g mainly reflects local chain dynamics of the polymeric system, the Fox-Loshaek relation (a modification of Flory-Fox equation)[21] predicts that, the T_g of the PEG-HA networks should increase linearly with increasing PEGDA fraction. In the case of a classical homogeneous polymer system, the Fox-Loshaek equation is given as,

$$T_g = T_g^{\infty} - K/M_c \tag{3.1}$$

where T_g^{∞} is the T_g of a polymer of infinite molecular weight and K is a material constant, M_c is molecular weight of network chain. It should be mentioned that this model does not take into account the '*copolymer effect*' of network junctions and the effect of dangling chains[22]. However, we find that indeed this relationship is valid for the PEGDA-HA networks, Figure 3.9 suggesting that this series of networks show behavior which is typical for polymer networks.

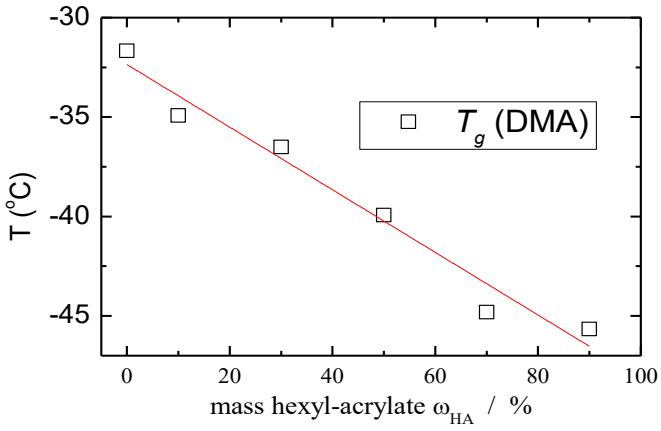

Figure 3.9. T_g of the cured PEGDA-HA samples, determined from DMA analysis, as a function of the weight ratio of HA (ω_{HA}). The straight line fit gives: intercept = -32.36, slope = -0.16, R^2 = 0.96.

The temperature dependence of the storage modulus is shown in Figure 3.10. For all the samples, the rubber-elastic plateau was found above -20 °C. The storage modulus, E' was found to decrease with increasing mass ratio of HA. This change corresponds to a decrease in the crosslink density and will be discussed below.

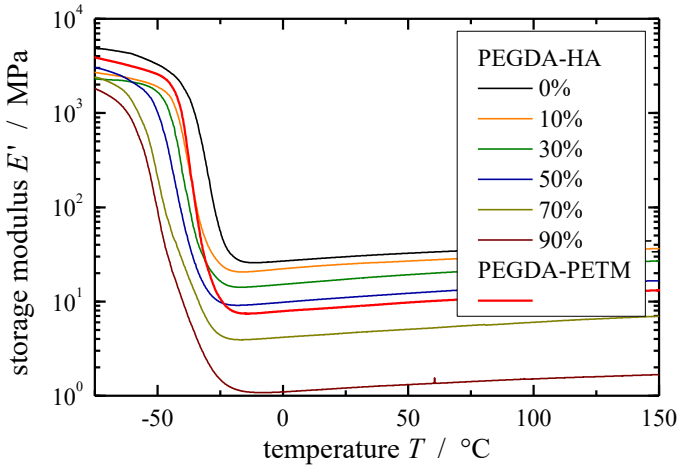

Figure 3.10. Storage modulus, E', of cured acrylate networks, measured by DMA with increasing ω_{HA}.

The storage modulus E' in the rubbery plateau region at temperatures above T_g can be used to determine M_{c+e}, the mean molar mass of network chains between chemical crosslinks and trapped chain entanglements[23], by using the predictions from rubber elasticity theory:

$$M_{c+e} = 3\rho RT/E' \tag{3.2}$$

where ρ is the specific density (in kg/m^3), R is the gas constant (8.4 J/(mol·K)), T is the absolute temperature, E' is the value of the storage modulus at temperature T in the high temperature plateau (in Pa). The results obtained by using this approach will be discussed below. However, as noted above, the statistical theory of rubber elasticity assumes that the individual network chains obey Gaussian statistics[24], which may not be applicable in this case. Furthermore, the effective number of elastically active network chains would be reduced in networks with spatial clustering of crosslinks[25], as a result, the M_{c+e} calculated from Eqn. (3.2) could be underestimated in the case of heterogeneous networks. On the other hand, the M_{c+e} value used can be overestimated in the presence of network defects like dangling chain fragments, as in PEG-HA networks, chain loops and chains which are not attached to the network.

T_2 relaxation analyses. Another way to probe the polymer dynamics in crosslinked gel systems is by ^{1}H NMR T_2 relaxation analysis, which is very sensitive to even small differences in the crosslink density due to the large influence of anisotropy of segmental motions on T_2 relaxation at temperatures well above T_g. Figure 3.11 shows the T_2 relaxation decay of the PEGDA-HA samples. As expected, by increasing the weight ratio of HA (ω_{HA}), the transverse relaxation of the system becomes longer. This is usually attributed to the decrease in crosslink density, since T_2 at high temperature is proportional to the molar mass of network chains.[26] With the addition of deuterated solvent $C_2D_2Cl_4$, it is found that the $T_{2,av}$ values of PEGDA-HA gels reach their maximum value at a swelling degree of $Q \approx 1.55$. This increase is mainly due to the release of temporary chain entanglements[10], and to a smaller extent due to a decrease in inter-chain dipole-dipole interaction.

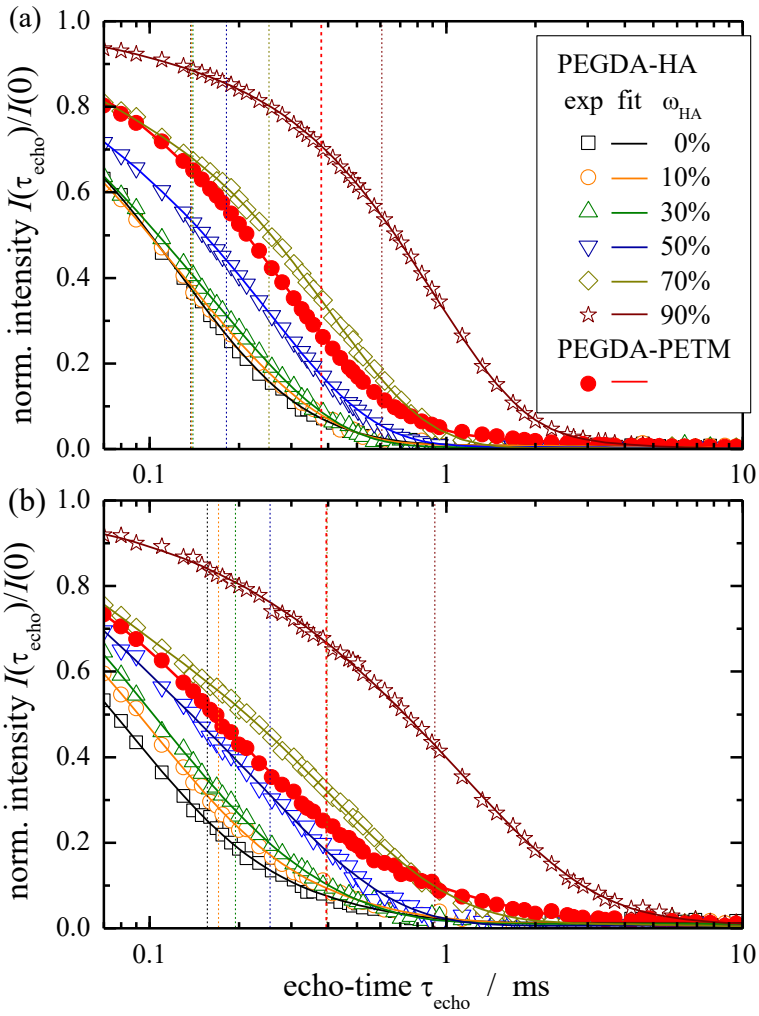

Figure 3.11. Normalized T_2 relaxation decay of PEGDA-HA gels measured using Hahn echo pulse sequence. The points represent the measured data and the lines are the corresponding fitting. (a) Dry state; (b) Swollen state (solvent: $C_2D_2Cl_4$, Q ≈ 1.55) (vertical lines indicate the $T_{2,av}$ value)

A number of methods can be used to extract M_{c+e} values of crosslinked gels from T_2 relaxation analyses. In this study, we use Gotlib's theory for the calculation of M_{c+e}.[26] This method is based on Kuhn and Grün model of freely joined chains, and assumes that the network chains consist of Z statistical segments between network junctions. T_2 value at the high temperature plateau, T_2^p, has been quantitatively related to the number of statistical segments in network chains[26, 27]. For a Gaussian chain, in which the average squared distance between network junctions is much shorter

than the contour chain length, the T_2^p value is related to Z statistical segments between the network junctions, and can be represented by the following relationship:[26]

$$Z = T_2^p / \left(\alpha T_2^{rl}\right) \tag{3.3}$$

Where α is a theoretical coefficient which depends on the angle between the segment axis and the inter-nuclear vector of the nearest nuclear spins on the main chain. For polymers containing aliphatic protons in the main chain, the coefficient α is close to 6.223. The T_2^{rl} value is related to the strength of intra-chain ^{1}H-^{1}H interactions in the rigid lattice, and could be measured for swollen samples below T_g. Depending on the testing temperature, there are several values in the literature for T_2^{rl}[10, 28, 29], however these values do not vary significantly (<5%) when testing temperature is 100 K below T_g of the material. Here we use 8.5 μs corresponding to the value measured at 108 K which is 120 K below T_gs of PEGDA-HA networks. Using the Z value calculated in this way, the M_{c+e} value can be calculated from:

$$M_{c+e} = ZC_\infty M_u / n \tag{3.4}$$

Where M_u is the molar mass per elementary chain unit, and n is the number of backbone bonds in an elementary chain unit. C_∞ is the number of backbone bonds in the statistical segment, a mean value of 5.0 is used in this study.[10]

The measured population average relaxation times of dry samples and of samples swollen to $Q \approx 1.55$, $T_{2,av}(dry)$ and $T_{2,av}(55\%sw)$, respectively, were used to calculate the M_{c+e} of the PEGDA-HA samples as well as PEGDA-PETM. Note that the M_{c+e} values obtained from this calculation are assumed to have a considerably high relative error of ~ 35% due to the uncertainty in C_∞ for PEGDA-HA networks, this issue will be discussed below.[10]

^{1}H DQ NMR Analysis To obtain further detailed insight into the network structure, *i.e.*, the chain dynamics and crosslink density, ^{1}H DQ NMR analyses were performed on the PEGDA-HA networks. The combination of fast MAS and high magnetic field strength provides spectral resolution permitting the acquisition of site-specific, chemical shift resolved DQ build-up curves for all chemical groups. The ^{1}H spectra are shown in Figure 3.12.

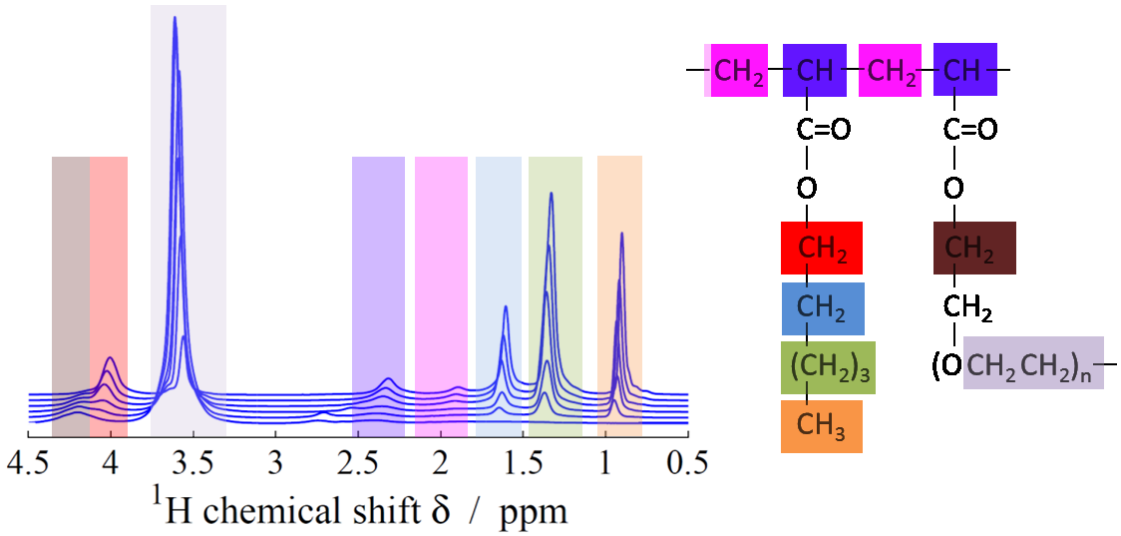

Figure 3.12: High-resolution ^{1}H spectra of PEGDA/HA networks and assignment of resonances. From back to front w_{HA} is decreasing.

Figure 3.13a shows the normalized DQ build-up curves of the PEG chains as a function of the DQ evolution time, $I_{\mathrm{nDQ}}(\tau_{DQ})$. The latter were obtained by evaluation of the resonance at a chemical shift of $\delta(^1H) = 3.56$ ppm which contains the ^{1}H signals of all CH_2 groups of PEG except for the CH_2 next to the carboxyl group of the acrylic backbone, the α-methine for which $\delta = 4.2$ ppm. With decreasing ω_{HA} the build-up of I_{nDQ} becomes faster. This corresponds to a higher dipolar coupling strength reflecting reduced conformational freedom of the polymer chains.

Figure 3.13b shows the corresponding coupling constant distributions obtained by the evaluation of the normalized build-up curves with normalization program *ftikreg*.[30] The average coupling constants, D_{avg}, of the distributions are indicated by the vertical dotted lines. The accuracy of the extracted values is supported by the rather good agreement of the experimental and the calculated build-up curves in Figure 3.13a. At high concentrations of HA co-monomers ($\omega_{HA} = 90\%$) the PEG chains are characterized by a narrow, Gaussian-like Residual Dipolar Coupling (RDC) distribution with a small shoulder towards higher values. The network could be considered as quite homogeneous. With decreasing ω_{HA}, the overall coupling constant distribution is significantly widened towards higher coupling constants. However, the maximum of the distributions shows a less significant dependence on ω_{HA} as compared to the average value of the distributions, since the Gaussian-like part of the distribution declines while the shoulder becomes more prominent.

Thus, the span of covered coupling constants increases rather than the distributions being shifted towards higher values. The distributions of networks with low or zero HA co-monomers exhibit RDCs ranging from 0.25-5 kHz. The rather broad distributions are usually attributed to heterogeneous network structure, as will be discussed below in detail.

The average RDC constants, D_{avg}, of PEG chains increase almost linearly with decreasing ω_{HA}. In general this observation is directly related to an increase of topological constraints on observed chain segments, *i.e.*, reduction of chain length between obstacles and/or formation of (trapped-) entanglements during curing which leads to increased crosslink density. However, these two factors do not fully explain the behavior observed here. All PEGDA-HA networks were prepared from the same PEGDA pre-polymers and only the fraction of the mono-functional HA monomers was varied. Furthermore, the molecular weight of the PEGDA precursor chains, $M_n = 488$ Da, is rather low and is significantly below the entanglement molecular weight, $M_e \approx 1.6$ kg/mol, of PEG/PEO[31]. This renders the formation of trapped PEG chain entanglements during the curing process highly unlikely. A possible explanation for the observed dependence of the molecular weight on the co-monomer weight fraction will be discussed below.

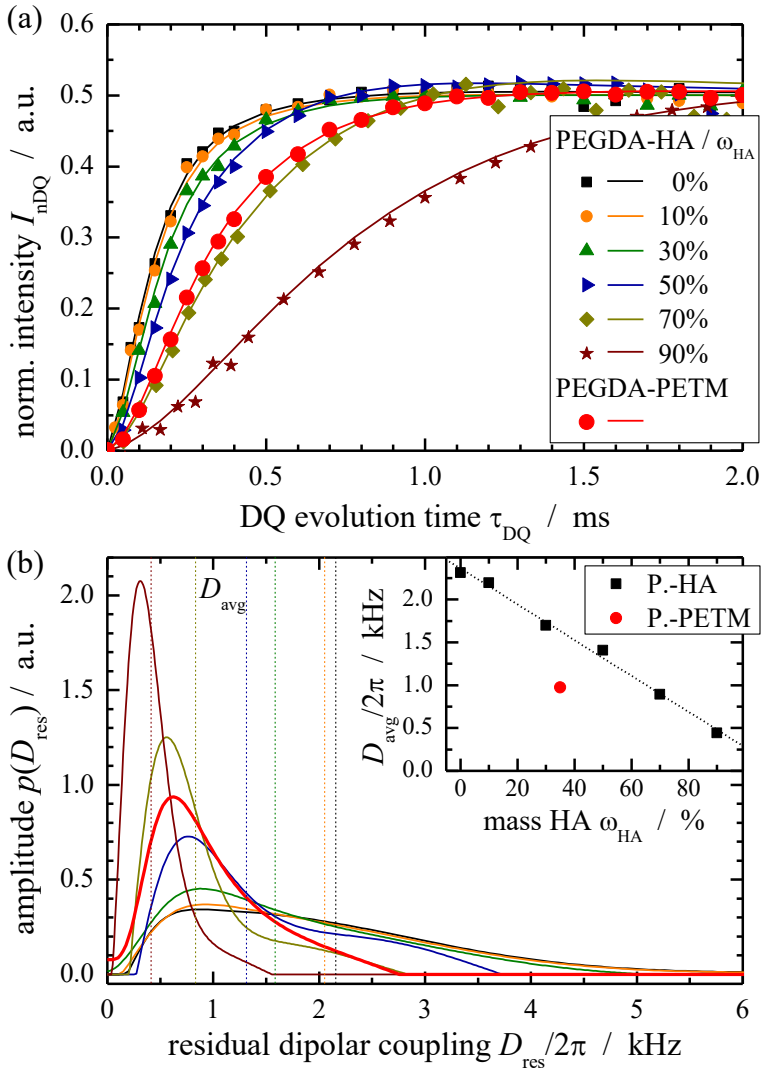

Figure 3.13. (a) Normalized DQ build-up intensities of PEG chains (3.56 ppm). Points represent experimental data and solid lines are results of the numerical regularization fit using *ftikreg* and (b) the corresponding coupling constant distributions. Vertical doted lines indicated the average coupling constant, D_{avg}, of the distributions. Insert shows D_{avg} as function of the HA co-monomer weight fraction, ω_{HA}, and the D_{avg} value for the for PEGDA-PETM network.

Figure 3.14a summarizes the average RDCs of all chemical groups which were clearly distinguishable due to a unique chemical shift (see Figure 3.12). The RDCs are found to have a

linear dependence on ω_{HA}, while deviations are only observed for the hexyl side-chains in networks with low concentration of HA co-monomers. In particular, the two resonances of the polyacrylate backbone; -CH- and -CH_2-, reveal a rather strong increase of D_{avg} up to 6.8 and 9.8 kHz, respectively, indicating a rather stiff, almost immobilized backbone at low or zero ω_{HA}.The chemical groups of PEGDA-HA possess distinctly different local spin systems, as is apparent from their different chemical shifts, rendering complicated any direct comparison of the absolute D_{avg} values. Therefore, the individual coupling constants have been normalized with respect to the coupling constants obtained for the PEGDA-HA network with ω_{HA}= 90% for further discussion. The fact that the coupling constants of the two resonances of the acrylic backbone are almost identical following this normalization demonstrates that it is at least internally consistent.

The normalized D_{avg} values are presented in Figure 3.14b and can be summarized in two main observations, (i) the anisotropy of acrylic chain motion are the most affected by ω_{HA}, and (ii) there is a gradual decrease in the anisotropy of HA and PEG chain segment motions with increasing ω_{HA}. The RDC constant of the acrylic backbone increases by a factor of 13 on reducing ω_{HA} from 90% to 0%, while the RDC constant of the PEG chains only increases by factor of 6. The molecular weight of acrylic chains is nearly the same for all networks (Table 3.1). Therefore, the large increase in RDCs of acrylic chains is caused by the increased stiffness of the acrylic chains on decreasing the HA content. For the $\omega_{HA} = 0\%$ network, each second carbon atom of the acrylic chain is connected to a PEG chain which is attached to another neighboring acrylic chain. Due to the high molar mass of the acrylic chains, PEG chains largely hinder translational mobility of zip-like acrylic multi-functional network junctions. This network topology also imposes significant constraints on translational dynamics of PEG chains. Hexyl-acrylate chains increase the average distance between PEG network chains and that in turn reduces the anisotropy of both PEG and acrylic chains motions.

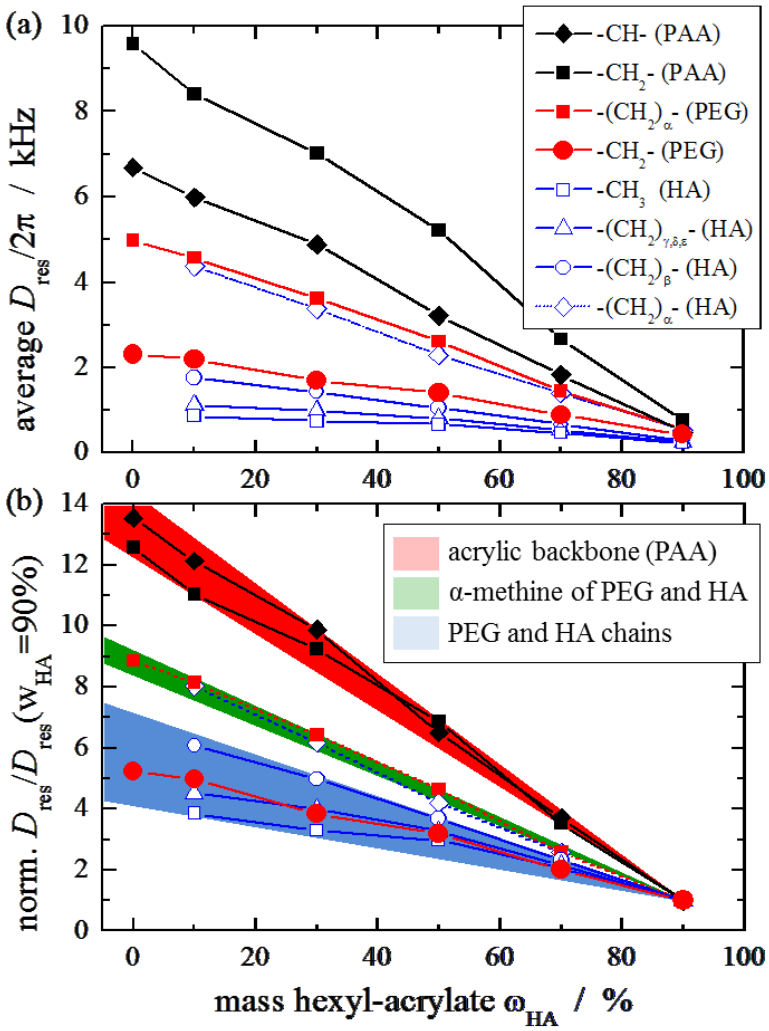

Figure 3.14. (a) Residual dipolar coupling, D_{avg}, of all chemical shift specified network segments as a function of HA co-monomer weight fraction, ω_{HA}, and (b) the same D_{avg} normalized with respect to the coupling constant obtained for the network with $\omega_{HA} = 90\%$.

3.4 DISCUSSION:

Dynamics of acrylic zip-like network junctions. The two types of networks studied were synthesized using di-functional PEGDA with narrow molecular mass distribution and largely differ in the type of network junctions. PEG chains in PEGDA-PETM networks are connected by point-like network junctions (Figure. 3.1). The evaluation of the conversion of acrylate double bonds (Table 3.1) for the latter, yields an average effective functionality f_{eff} ≈3.6.

PEGDA-HA networks have largely different network topology which is highly dependent on the monoacrylate (HA) weight fraction, ω_{HA}. For $\omega_{HA} = 0$ network, each monomeric unit of an acrylic chain is connected to one end of a PEG chain. The other chain end of the PEG chain is connected to a neighboring acrylic chain. Thus, each acrylic chain is an extended multifunctional zip-like network junction with densely packed PEG chains. This network topology results in largely restricted translational and rotational dynamics of the acrylic backbone as well as the PEG network chains, as demonstrated by the rather high RDC of the backbone resonances. However, acrylic chains still retain some flexibility as is apparent from comparison of their RDC value ($D_{avg} = 9.8$ kHz for PEGDA network) with the static dipolar coupling of CH_2-units ($D_{stat} \approx 21$ kHz).

The overall stiffness of the acrylic chain changes with ω_{HA} value. The average distance between PEG network chains increases with increasing ω_{HA}, since both share the same acrylate backbone. 2D Double Quantum – Single Quantum (DQ-SQ) correlation experiments for PEGDA-HA networks (data not shown) demonstrate that the HA co-monomers are statistically distributed between PEG chains. At high ω_{HA} the networks can be considered bimodal. One type of network chain originates from PEG chains which interconnect acrylic chains, the other type is brush-like acrylic chains bearing pendent HA chains and PEG chains.

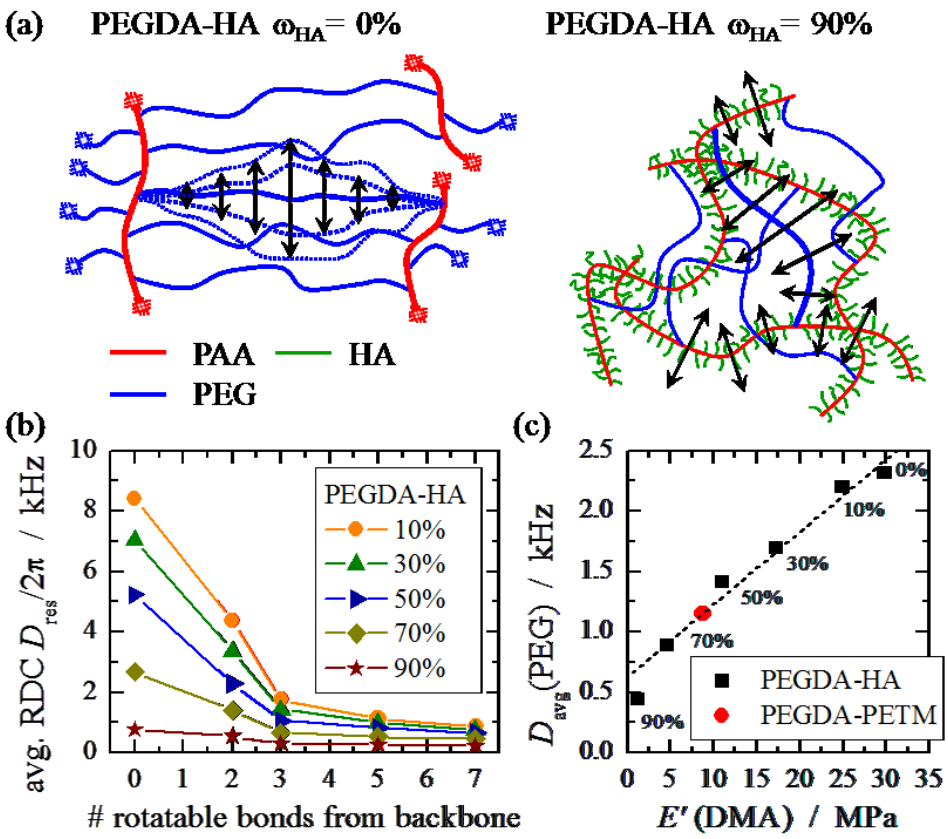

Figure 3.15. (a) Illustration of network dynamics for PEGDA-HA in dependence of HA co-monomer weight fraction. (b) D_{avg} values of chemical groups along the HA side-chains. (standard deviation (SD) is *c.*10%) (c) The comparison between the elastic storage modulus E' and the average RDC D_{avg} of PEG chains. (SD *c.*20%)

The length of the acrylic backbone is not significantly affected by the HA co-monomer weight fraction as demonstrated by the results of the hydrolysis. M_n of the acrylic backbone is found to be in the range of 9700 – 12300 g/mol which corresponds to approximately 135 – 175 acrylic chain units. For PEG network chains the same molecular weight, $M_n \approx 488$ Da, is obtained for all investigated networks. Basically the HA units increase flexibility of acrylic chains which causes a decrease in RDC of all chain units with increasing HA content (Figure 3.15a). At the same time the topological constraints imposed by the acrylic backbone on the PEG chains are reduced upon increasing the HA content.

The influence of the acrylic backbone mobility on grafted chains is apparent from the HA side chain dynamics. Figure 3.15b shows the D_{avg} values of the different chain units of HA side chains

with respect to their bond index. For all networks, D_{avg} of HA chain units decreases on increasing the distance from acrylic chains, due to higher conformational freedom moving away from the grafting points. This behavior is commonly observed for short chains attached to longer chains[32] or to the surface of solids[33]. Similarly, the D_{avg} for the CH_2 groups of PEG chains in the α-position is larger than that for the other PEG units. The normalized coupling constants are almost identical for CH_2 units in the α-position for PEG and HA chains (Figure 3.14b). It is suggested that the rather broad coupling constant distribution of PEG chains at low ω_{HA} (Figure 3.13b) is caused by differences in dipolar coupling along PEG chains rather than by network heterogeneity. The less-mobile acrylic chains restrict conformational freedom of densely attached PEG network chains (Figure. 3.15a). The extent of motional freedom of all chain units is larger for network containing a higher amount of HA. The largest impact of chain dynamics is observed for acrylic network junctions and the lowest one for HA side groups (Figure 3.14). Thus overall molecular mobility is largely determined by the mobility of the acrylic backbone.

Network junction functionality. The change in network topology, as described above, strongly affects the crosslink functionality. In principle, the latter is determined by the number of directly adjacent acrylate backbone monomers bearing PEG chains, N_{PEG}. For PEGDA-HA with ω_{HA}=0, the functionality is theoretically equivalent to the backbone length which is obtained from the result of hydrolysis, and yields a value of $f \approx 150$. Mono-functional HA monomers interrupt the elongated acrylic crosslinks and thus the functionality is significantly reduced with increasing HA weight fraction. Assuming the HA strands align themselves along the PEG chain, the crosslink functionality is $f = N_{PEG} + 1$ (or 2, depending on the position of the crosslink PEG at the acrylic backbone; non-terminal or terminal). Therefore, for PEGDA-HA (ω_{HA} = 90%) with a clear bimodal network structure, the effective functionality is at most $f_{eff} \approx 3$.

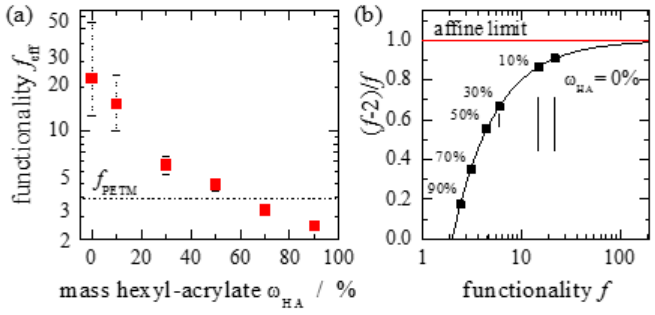

Figure 3.16. (a) Effective functionality of acrylic crosslinks in PEGDA-HA networks derived from DQ-NMR analysis. (b) Comparison of phantom and affine model pre-factors of PEGDA-HA networks as a function of crosslink functionality.

Detailed information about the functionality of acrylic network junctions in PEGDA-HA networks can be obtained by analyzing DQ-NMR results for PEG chains using the PEGDA-PETM network as reference. Based on these considerations, the D_{avg} and M_{c+e} values of PEG chains can be related by:[16, 34]

$$M_{c+e}^{NMR} = \frac{f-2}{f}\frac{d_{ref}}{D_{avg}/2\pi} \tag{3.5}$$

Where d_{ref} is the polymer specific reference coupling. For the PEGDA-PETM network, f is known from conversion of double bonds, $f = 3.64 \pm 0.2$. Thus Eqn. 3.5 could yield a well-defined value for M_{c+e}, if d_{ref} is known. This parameter depends on the specific dynamics within and beyond a monomer (*e.g.* effective chain stiffness)[35]. Under the assumption that d_{ref} is unchanged (which is justified in part by the fact that both network types comprise PEG chains of the same length), an apparent functionality can be calculated for the PEGDA-HA series. The results are shown in Figure 3.16a: the value for the acrylate junctions is considerably reduced with increasing HA content, from $f \approx 25$ for $\omega_{HA} = 0$, to $f \approx 2.5$ for $\omega_{HA} = 90$. The deviation of the apparent effective functionality for $\omega_{HA} = 0$ from the expected value of ~150 may be attributed to the residual mobility of the elongated acrylic crosslinks. Hence the values obtained from Eqn. 3.5 must be treated with some caution.

As shown in Figure 3.15c, a linear correlation could be found between the elastic modulus E' from DMA and the D_{avg} value of PEG chains from DQ NMR. While E' is determined by the response

of the entire network, it is interesting to find that the above mentioned correlation persists up to rather high ω_{HA} values, a range in which the contributions of more flexible HA strands to E' become significant, eventually leading to a deviation between the two values. Hence, this observed correlation suggests that both the macroscopic response, seen in E', and the local dynamics, seen in RDC, have similar dependence on functionality

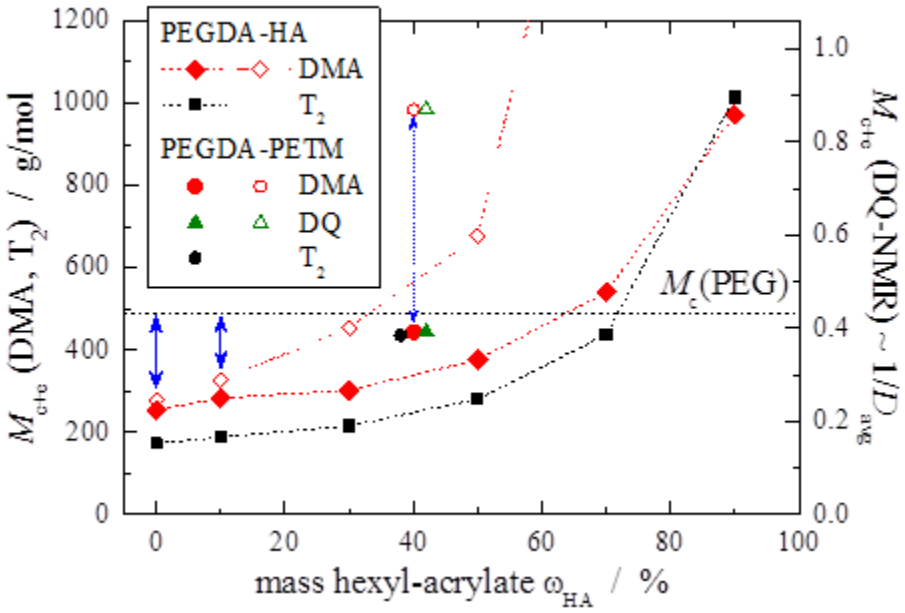

Figure 3.17. Mean molar mass between crosslinks and trapped entanglements, M_{c+e}, as a function of HA weight fraction, ω_{HA}, obtained by evaluation of experimental results using phantom model (closed symbols), by applying the NMR-derived effective crosslink functionality, and the affine model (open symbols).

Molecular mass of network chains. As described above, the mean molar mass of network chains between chemical crosslinks and trapped chain entanglements, M_{c+e} can be calculated from DMA data, $T_{2,av}$, as measured by LF NMR relaxometry, and $1/D_{avg}$ which is measured for PEG chains by DQ NMR. The results of these methods are summarized in Figure. 3.17. DQ-NMR results are only shown for PEGDA-PETM network, as in this case the values only reflect the molecular weight of PEG chains. This is not the case for PEGDA-HA networks which comprise PEG network chains, HA short dangling chains and polyacrylate multifunctional network junctions.

For the PEGDA-PETM network with point-like junctions, M_{c+e} values of 436 and 443 g/mol were calculated from T_2 relaxometry and DMA respectively (see Figure 3.17). Effective functionality was employed for DMA analysis. The results are close to the known molar mass of the PEG chains.

The rather good agreement between these two values suggests that a phantom-model-like approach is applicable for these networks rather than the affine-model-like approach. This is supported by the fact that using the affine-model-like approach evaluation of DMA results yields a M_{c+e} two times higher than expected. Contrary to the above observation, the evaluation of DMA data for the PEGDA-HA network with lower ω_{HA} provide rather low M_{c+e} values, approximately 2.2 times lower than the molar mass of PEG chains. In particular, this observation is independent of the applied network model for low or zero concentration of HA. Since the phantom model converges towards the limit of the affine model for high crosslink functionality (f >10), evaluation using either approach yields almost identical M_{c+e} values, as expected. On the other hand, M_{c+e} values obtained using the phantom-model-like analysis of DMA data is in good agreement with that calculated from T_2 relaxometry. In combination with the fact that results of the T_2 measurements are independent of considerations regarding the network model, *i.e.* crosslink functionality, the observed tendencies strongly suggest an advantage in implementing phantom-model-like evaluation for PEGDA-HA networks. As this was also the outcome for PEGDA-PETM networks, it is likely that this is more generally the case. The overall difference in M_{c+e} from DMA and NMR methods is due to smaller time scale of chain dynamics as probed by NMR, *i.e.*, in the range of milliseconds, whereas DMA measures equilibrium modulus corresponding to zero frequency.

3.5 CONCLUSIONS:

Two types of polyacrylate networks were studied using different methods. The networks were synthesized using di-functional PEGDA with narrow molecular mass distributions, which largely differ in the type of network junctions. In PEGDA-HA networks, with zip-like junction topology, the mobility of acrylic backbones acting as multifunctional junctions is largely hindered leading to rather strong topological constraints on the attached PEG chains. While in the case of the PEGDA-PETM network, with point-like junction topology, the classical phantom-model-like behavior is found to dominate the network dynamics.

Chemical shift resolved ^{1}H double-quantum (DQ) NMR experiments performed on PEGDA networks yield detailed information about the dynamics of individual network components. The combination of fast magic angle spinning and high magnetic field strength provides spectral resolution making it possible to record well-defined DQ build-up curves for the resonances of the polyacrylic backbone, PEG and HA chains, and time resolution to reliably determine RDCs up to 10 kHz.

The analysis shows that mechanical properties of the PEGDA networks studied are mainly governed by the junction mobility and crosslink functionality. The influence of these two aspects cannot be treated separately, since they are interdependent for these networks. With increasing effective functionality, mobility of junctions is reduced as shown by the increase of acrylic backbone RDCs. At low HA content, the acrylic backbone is almost immobilized. This gives rise to rather strong topological constraints on the ends of the attached PEG chains and explains the observed increase of average RDC of PEG chains. However, acrylic backbone mobility is more affected by variation of ω_{HA} than overall mobility of PEG chains. On decreasing ω_{HA}, from 90% to 0%, the backbone RDCs increase by a factor of 13; while the D_{avg} values of the PEG chains only increase by a factor of ~5. This indicates a strong mobility anisotropy in PEGDA-HA networks which is manifested by the observed decrease of RDCs along the HA side chains. In the same way, segments of the PEG network chains close to acrylic backbone experience a significantly stronger mobility restriction compared to those away from the backbone, giving rise to the broad RDC distributions observed for PEG in the networks with lower ω_{HA}. The addition of mono-acrylate into the network increases the mobility of acrylic backbone. Hence, the mobility

heterogeneity between acrylic backbone and PEG chains becomes less prominent in the network with higher ω_{HA}, as demonstrated by the much narrower RDC distribution of PEG chains, which indicates a considerable reduction in mobility anisotropy along the PEG chains.

Considerably lower M_{c+e} values as determined by two different methods for the networks with zip-like network junctions, suggests the following: Low mobility acrylic backbones with densely attached PEG network chains largely restrict the number of possible conformations of PEG chains. This causes significantly larger network modulus and larger anisotropy of chain motions as measured by DMA and NMR, respectively. This effect should be taken into account in the analysis of polymer networks with zip-like network junctions and for heterogeneous networks in general. Our conclusion is in good agreement with previous studies,[25, 27, 36-39] which highlight the significant contribution of topological constraints on crosslink density determined by NMR and mechanical experiments for heterogeneous networks.[36, 39, 40] The topological constraints restrain the chains from adopting some conformations, which has the same effect as increasing effective crosslink density leading to lower M_{c+e} values calculated using classical rubber elasticity theory. Finally, while a number of possible corrections to classical rubber elasticity theory have been proposed, for instance by Charlesworth,[41] our results highlight the need for such corrections to be based on the physical demands of the real network structures, as identified using NMR techniques, for them to be properly applied to largely heterogeneous networks.

References:

1. T. Billiet, M. Vandenhaute, J. Schelfhout, S. Van Vlierberghe, P. Dubruel, A review of trends and limitations in hydrogel-rapid prototyping for tissue engineering. *Biomaterials* **33**, 6020 (2012).
2. X. J. Liao, G. S. Chen, M. Jiang, Hydrogels locked by molecular recognition aiming at responsiveness and functionality. *Polym Chem-Uk* **4**, 1733 (2013).
3. M. Moeller, K. Matyjaszewski. (Elsevier Science, Amsterdam ; London, 2012), pp. 1 online resource (10 v. (7750 p.)).
4. M. Rubinstein, R. H. Colby, *Polymer physics*. (Oxford University Press, Oxford ; New York, 2003), pp. xi, 440 p.
5. F. T. Wall, P. J. Flory, Statistical Thermodynamics of Rubber Elasticity. *J Chem Phys* **19**, 1435 (1951).
6. H. M. James, E. Guth, Theory of the Increase in Rigidity of Rubber during Cure. *Phys Rev* **72**, 537 (1947).
7. M. T. J. Doi, Molecular modeling of entanglement. *Philosophical Transactions of the Royal Society Ser. A*, 641 (2003).
8. M. G. Brereton, P. G. Klein, Analysis of the Rubber Elasticity of Polyethylene Networks Based on the Slip Link Model of Edwards,S.F. *Polymer* **29**, 970 (1988).
9. S. A. Dubrovskii, M. A. Lagutina, V. V. Vasiljev, Swelling, elasticity and structure of hydrogels prepared via bis-macromonomers of poly(ethylene oxide). *Macromol Symp* **200**, 147 (2003).
10. V. M. Litvinov, A. A. Dias, Analysis of network structure of UV-cured acrylates by H-1 NMR relaxation, C-13 NMR spectroscopy, and dynamic mechanical experiments. *Macromolecules* **34**, 4051 (2001).
11. D. J. Waters *et al.*, Morphology of Photopolymerized End-Linked Poly(ethylene glycol) Hydrogels by Small-Angle X-ray Scattering. *Macromolecules* **43**, 6861 (2010).
12. M. Krzeminski, M. Molinari, M. Troyon, X. Coqueret, Characterization by Atomic Force Microscopy of the Nanoheterogeneities Produced by the Radiation-Induced Cross-Linking Polymerization of Aromatic Diacrylates. *Macromolecules* **43**, 8121 (2010).
13. P. M. de Molina, S. Lad, M. E. Helgeson, Heterogeneity and its Influence on the Properties of Difunctional Poly(ethylene glycol) Hydrogels: Structure and Mechanics. *Macromolecules* **48**, 5402 (2015).
14. Y. J. Jiang, J. Chen, C. Deng, E. J. Suuronen, Z. Y. Zhong, Click hydrogels, microgels and nanogels: Emerging platforms for drug delivery and tissue engineering. *Biomaterials* **35**, 4969 (2014).
15. K. Saalwachter, Robust NMR Approaches for the Determination of Homonuclear Dipole-Dipole Coupling Constants in Studies of Solid Materials and Biomolecules. *Chemphyschem : a European journal of chemical physics and physical chemistry* **14**, 3000 (2013).
16. W. Chasse, M. Lang, J. U. Sommer, K. Saalwachter, Cross-Link Density Estimation of PDMS Networks with Precise Consideration of Networks Defects. *Macromolecules* **45**, 899 (2012).
17. M. P. Stevens, *Polymer chemistry : an introduction*. (Oxford University Press, New York, ed. 3rd, 1999), pp. xix, 551 p.
18. A. B. Lowe, Thiol-ene "click" reactions and recent applications in polymer and materials synthesis. *Polym Chem-Uk* **1**, 17 (2010).
19. R. Peters *et al.*, Characterisation of UV-cured acrylate networks by means of hydrolysis followed by aqueous size-exclusion combined with reversed-phase chromatography. *Journal of Chromatography A* **1156**, 111 (2007).
20. J. A. Burdick, T. M. Lovestead, K. S. Anseth, Kinetic chain lengths in highly cross-linked networks formed by the photoinitiated polymerization of divinyl monomers: A gel permeation chromatography investigation. *Biomacromolecules* **4**, 149 (2003).

21. T. G. Fox, S. Loshaek, Influence of Molecular Weight and Degree of Crosslinking on the Specific Volume and Glass Temperature of Polymers. *J Polym Sci* **15**, 371 (1955).
22. A. L. Andrady, M. D. Sefcik, Glass-Transition in Poly(Propylene Glycol) Networks. *J Polym Sci Pol Phys* **21**, 2453 (1983).
23. P. J. Flory, *Principles of polymer chemistry*. George Fisher Baker non-resident lectureship in chemistry at Cornell University (Cornell University Press, Ithaca,, 1953), pp. 672 p.
24. L. R. G. Treloar, *The physics of rubber elasticity*. Monographs on the physics and chemistry of materials (Clarendon Press, Oxford,, ed. 3d, 1975), pp. xii, 310 p.
25. T. A. Vilgis, G. Heinrich, Statics and Dynamics of Heterogeneous Polymer Networks. *Macromol Theor Simul* **3**, 271 (1994).
26. Y. Y. Gotlib, M. I. Lifshits, V. A. Shevelev, I. S. Lishanskii, I. V. Balanina, Influence of Chemical Cross-Links Network on Spin-Spin Relaxation in Cross-Linked Swollen Polymer Systems. *Vysokomol Soedin a+* **18**, 2299 (1976).
27. C. G. Fry, A. C. Lind, Determination of Cross-Link Density in Thermoset Polymers by Use of Solid-State H-1-Nmr Techniques. *Macromolecules* **21**, 1292 (1988).
28. V. M. Litvinov, W. Barendswaard, M. van Duin, The density of chemical crosslinks and chain entanglements in unfilled EPDM vulcanizates as studied with low resolution, solid state H-1 NMR. *Rubber Chem Technol* **71**, 105 (1998).
29. P. Diehl, E. Fluck, R. Kosfeld, in *NMR Basic Principles and Progress / NMR Grundlagen und Fortschritte, 0170-5989 4*. (Springer Berlin Heidelberg,, Berlin, Heidelberg, 1971), pp. 1 online resource.
30. W. Chasse, J. L. Valentin, G. D. Genesky, C. Cohen, K. Saalwachter, Precise dipolar coupling constant distribution analysis in proton multiple-quantum NMR of elastomers. *J Chem Phys* **134**, (2011).
31. J. E. Mark, *Physical properties of polymers handbook*. AIP series in polymers and complex materials (AIP Press, Woodbury, N.Y., 1996), pp. xv, 723 p.
32. M. K. Parkinson, K.; Spiess, H. W.; Wilhelm, M., Effect of Branch Length on ^{13}C NMR Relaxation Properties in Molten Poly[ethylene-co-(α-olefin)] Model Systems. *Macromol Chem Phys* **288**, 2128 (October 24, 2007, 2007).
33. V. M. Litvinov, H. Barthel, J. Weis, Structure of a PDMS layer grafted onto a silica surface studied by means of DSC and solid-state NMR. *Macromolecules* **35**, 4356 (2002).
34. S. Schlogl *et al.*, Photo-vulcanization using thiol-ene chemistry: Film formation, morphology and network characteristics of UV crosslinked rubber latices. *Polymer* **55**, 5584 (2014).
35. S. Schlogl, M. L. Trutschel, W. Chasse, G. Riess, K. Saalwachter, Entanglement Effects in Elastomers: Macroscopic vs Microscopic Properties. *Macromolecules* **47**, 2759 (2014).
36. M. G. Brereton, I. M. Ward, N. Boden, P. Wright, Nature of the Proton Nmr Transverse Relaxation Function of Polyethylene Melts .1. Monodispersed Polyethylenes. *Macromolecules* **24**, 2068 (1991).
37. R. Kimmich, M. Kopf, P. Callaghan, Components of Transverse Nmr Relaxation in Polymer Melts - Influence of Chain-End Dynamics. *J Polym Sci Pol Phys* **29**, 1025 (1991).
38. M. G. Brereton, Nmr Transverse Relaxation Function Calculated for Constrained Polymer-Chains - Application to Entanglements and Networks. *Macromolecules* **23**, 1119 (1990).
39. V. M. Litvinov, M. E. Ries, T. W. Baughman, A. Henke, P. P. Madoka, Chain Entanglements in Polyethylene Melts. Why Is It Studied Again? *Macromolecules* **46**, 541 (2013).
40. D. Frich, K. Goranov, L. Schneggenburger, J. Economy, Novel high-temperature aromatic copolyester thermosets: Synthesis, characterization, and physical properties. *Macromolecules* **29**, 7734 (1996).

41. J. M. Charlesworth, Effect of Crosslink Density on Molecular Relaxations in Diepoxide-Diamine Network Polymers .2. The Rubbery Plateau Region. *Polym Eng Sci* **28**, 230 (1988).

Chapter IV

Effect of Hydrogen-bonding on network formation and chain dynamics in polyacrylate system

4.1 INTRODUCTION

Hydrogels have been used for various biological application from tissue engineering to drug delivery vehicle (DDV) because of their resemblance to soft tissue in several aspects (e.g. mechanical properties)[1] As three dimensional, cross-linked networks, hydrogels can be formed literally by any water-soluble polymer. This renders the tailoring of hydrogel's macroscopic properties via the modification of their microscopic chemical structure possible.

In the past two decades much work have been done to improve the performance of hydrogels. One way to modify the chemical structure of hydrogels is to introduce additional functional groups into the polymer precursor before the crosslinking reaction. By using a Si-based monomer, Gaylord[2, 3] and scientists at Dow Corning [4, 5] successfully developed new generation contact lenses with higher O_2 permeability. While Weissman et al. incorporated poly(N-isopropylacrylamide) (PNIPAM) into the network to create a thermally switchable hydrogel.[6] For drug delivery applications, these structures with large mesh size could be tuned by varying the crosslink density of the network or by changing the affinity of gel matrix to the aqueous environment (e.g. by introducing hydrogen bonding). These modifications result in controlled diffusion rate of small molecules inside the gel matrix,[7] which is of current interest in designing DDVs.

On the other hand, as one of the most widely used methods for producing hydrogel networks in industry, UV-curing has been implemented into various material-processing procedures on the manufacturing scale.[8] As noted in Chapter IV, UV-curing is a process which induces chemical and physical changes in the material (e.g. crosslinking, polymerization) by irradiating oligomers with UV light. It offers several advantages, for instance, solvent-free, fast curing time and easy application, over other curing methods. However, materials generated by this technique are often intrinsically heterogeneous, which renders direct analysis/characterization difficult. Hence for industrial application of hydrogels, it is necessary to understand the impact of chemical structure changes on heterogeneous gels' properties in order for us to better design the next generation smart hydrogels.

Some studies[9-11] carried out by Decker et al. in the 1990s investigated the relationship between the monomer structure and the kinetics of the photoinitiated polymerization by varying the structure of the monomer. An increase in the reactivity of the monoacrylate was observed for monomer with large side chain groups. A study by Jansen et al. suggested a pre-organization of monoacrylates (Figure 4.1) before the start of photo-initiated polymerization for systems in which hydrogen bonding groups were present in the side chain.[12, 13] This effect was inferred from the observation that a rather large maximum rate of polymerization (R_p) was measured for the hydrogen bond containing system in comparison to its non-hydrogen bond containing counterpart, presumably due to the reduced average spatial distance between individual chains. Similar phenomena were also found in other studies[14, 15]. However, no direct observation of the pre-organization of monoacrylate has been found in the literature beside the indication from some kinetic studies[12, 14], which may be due to the rather complicated nature of photo-initiated polymerization reactions. To investigate this putative effect, one could probe cluster formation in gel matrices produced by similar photo-initiated polymerization but containing more than one monomer.

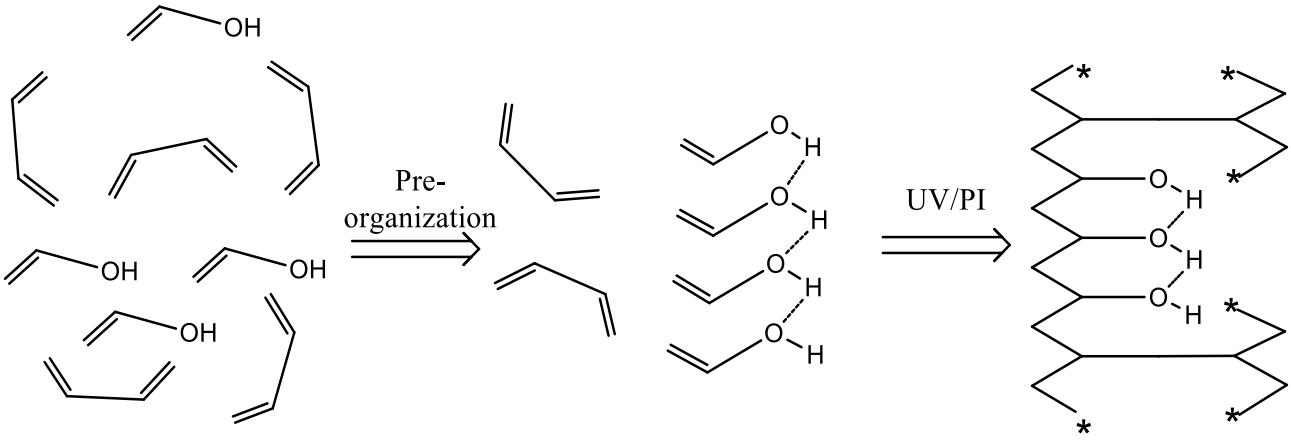

Figure 4.1. Schematic picture about the pre-organization of monoacrylate induced by hydrogen bonding during photo-initiated polymerization.

Currently, several different techniques (e.g. Dynamic Mechanical Analyses (DMA)) are frequently used to extract information about the chain dynamics of gel matrices. Among them, Nuclear Magnetic Resonances (NMR), as one of the most informative method on studying polymers, has its advantages over other techniques due to high selectivity to dynamics of different chain segment. Solid state NMR spectroscopy has been used for monitoring the conversion of the various acrylates undergoing radical curing, while ^{13}C NMR T_1 relaxometry also has been applied to the study of

polymer chain dynamics.[16] However, due to its much higher sensitivity toward to the small difference in crosslink density, NMR T_2 relaxometry, rather than T_1 relaxometry, is a better approach to probe the molecular mobility of polymer chains inside the network.[17, 18] Litvinov et al. used NMR ^{1}H T_2 relaxometry to analyze the crosslink density of PEG-DA based UV-cured network.[19] Meanwhile, with the development[20, 21] in the application of high resolution MQ NMR technique for polymeric material by Spiess' group in 1990s, it is possible to directly probe chemical shift-specified residual dipolar coupling constants, R_{res} value for each individual functional group. This makes the explicit analyses of crosslink density feasible as shown in Chapter III.

In this study, a series of PEGDA-based hydrogels were synthesized via UV-initiated polymerization. Two different hydrogen bonding containing monoacrylates with different hydrogen bonding positions (terminal or non-terminal) on their side chain were used in this study. The hydrogen bonding strength in these hydrogels was tailored by varying the mass ratio of the crosslinker (PEGDA) in the curing formulation. After confirming high double bond conversion by FTIR, these networks were studied by DMA, low field ^{1}H NMR relaxometry. DQ-SQ correlation NMR was used to analyze the cluster formation in the network. M_{e+c} values for these networks were also determined and compared to these networks described in Chapter III. This work is a collaboration work with Dr. Walter Chassé from Prof. Arno Kentgens' group in Radboud University of Nijmegen. Dr. Chassé performed the DQ-SQ NMR analyses for this study.

4.2 EXPERIMENT PART:

Sample Preparation: Polyethylene glycol-700-diacrylate (PEGDA-700), Hexyl acrylate (HA), 2-Hydroxyethyl acrylate (HEA), 2-[[(butylamino)carbonyl]oxy]ethyl acrylate (BACOEA), Photo-initiator: 2,2-Dimethoxy-2-phenylacetophenone (DMPA) was used for syntheses of networks. All the chemicals were obtained from Sigma Aldrich, and used without any further purification.

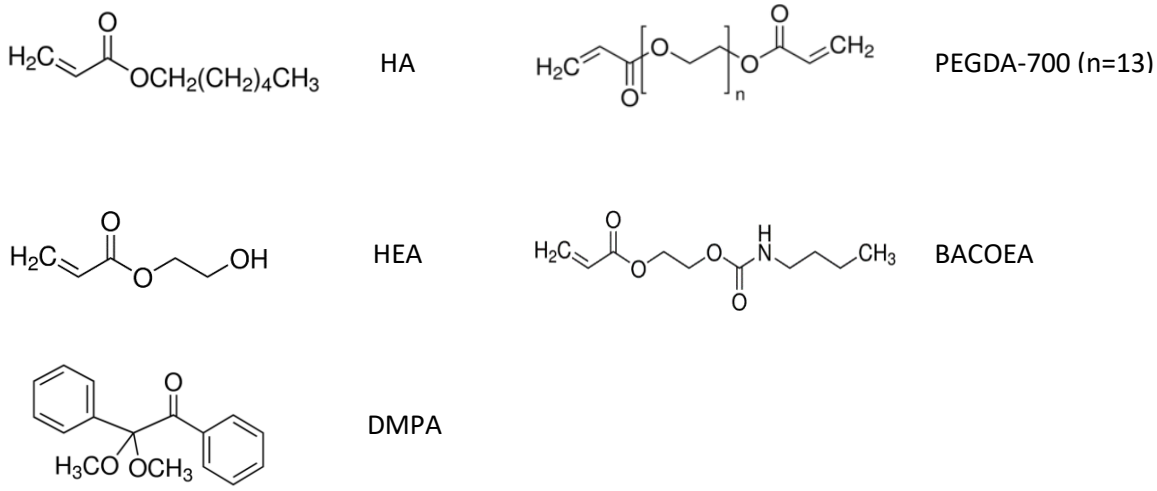

Figure 4.2 Chemical structures of monomers/crosslinks used in the study.

Networks were prepared by UV-curing of the chemicals with the proportion described in Table 4.1. (Photo initiator: 10-20 mg 2,2-Dimethoxy-2-phenylacetophenone (DMPA)). The formulation was poured into a petri dish, and then the petri dish was passed through the UV-rig (Heraeus Noblelight Fusion UV Inc.'s F300S model, with I300MB irradiator which has a lamp power of 300w/in (120w/cm), 1800 watts total) 30 times. Afterwards the cured film was inverted, and was then passed through the UV-rig a further 30 times. The rim of the resulting film was cut off, and the remaining part with a thickness around 1mm was used for all the tests. All the networks were put into oven, and heated to above 100 ^{o}C for 24 hours before measurement. Neither solution state NMR nor solid state MAS NMR analyses of these suggested the presence of any trace of H_2O.

The double bond conversions of the films (which describes the completeness of crosslinking reaction) was measured by FTIR, and molecular weight of the hydrolyzed acrylate backbone chains was determined by chromatographic analyses. Results of network characterization are summarized in Table 4.1.

Mechanical Analyses. The glass transition temperature and the storage modulus were measured with TA DMA Q800 Analyzer at a frequency of 1 Hz. Test samples with 5 mm width and 15 mm length were cut out from the cured films. The thickness of the test bar was measured with a calibrated micrometer. The DMA test were started from -90 ºC and the temperature was gradually increased to 150 ºC with a ramp speed of 3 ºC/min.

Solid State NMR Analyses of Network Structure. Solid-state magic angle spinning (MAS) ^{13}C NMR spectra were recorded on a Bruker Avance III 600 MHz spectrometer equipped with a solid standard-bore Magic Angel Spinning (SBMAS) probe. 4 mm MAS rotor (80 μL) was used at a spinning rate of 12 kHz. Single pulse excitation (SPE) and cross-polarization (CP) pulse sequences were used in this study. The 90º pulse length was calibrated to 2 μs. The spectra were recorded with two different cross-polarization time (τ_{cp}) of 0.5 ms and 10 ms, in order to distinguish between rigid and soft part of the material.

^{1}H NMR T_2 Relaxation Test. The ^{1}H transverse magnetization relaxation (T_2 relaxation) times of these networks were measured on Bruker Minispec MQ20 spectrometer operating at 20 MHz. The T_2 relaxation decay was measured with the Hahn-echo (HE) pulse sequence, 90^o_x—τ_{HE}—180^o_y—τ_{HE}—(acquisition), where $\tau_{HE} \geq 35$ µs and Single pulse excitation (SPE). In the HE experiment, an echo signal is formed after the second pulse in the HE with a maximum at time $t = 2\tau_{HE}$ after the first 90º pulse. By varying τ_{HE}, the amplitude of the transverse magnetization, $A(t)$, is measured as a function of time t. The ^{1}H NMR T_2 relaxation experiments in this study were performed at 50ºC, well above the T_g value of the gels.

Homonuclear ^{1}H-^{1}H Double Quantum-Single Quantum (DQ-SQ) Correlation NMR. The 2D ^{1}H double-quantum (DQ) correlation experiments were carried out on a VNMRS 850 operating at a ^{1}H Larmor frequency of 849.71 MHz equipped with a 1.6 mm triple resonance probe. The MAS frequency was set to 40 kHz and the sample temperature to 50ºC. The 90º pulse length was calibrated to 2 μs. The data for all network samples was acquired using a recently published improved version of the Back-to-Back (BaBa) sequence, BaBa-xy16, for broadband homonuclear DQ recoupling.[22] As noted above, these experiments and analysis was performed by Dr. Walter Chassé.

4.3 RESULTS AND DISCUSSION

Network Structure Analysis. As mentioned in Chapter IV, to ensure that the expected network structures was formed during the polymerization reactions, ^{13}C solid state NMR spectra and IR spectra were recorded for all the samples, and ^{1}H solution state NMR analysis of the same samples was used for chemical structure characterization of the sol fraction. As is apparent from the example shown in Figure 4.3, similar conclusions about the network structure to those found in Chapter IV can be drawn: the conversion of the double bond for all the samples are almost complete (see Table 4.1), and no significant side reactions occurred during in the curing reaction.

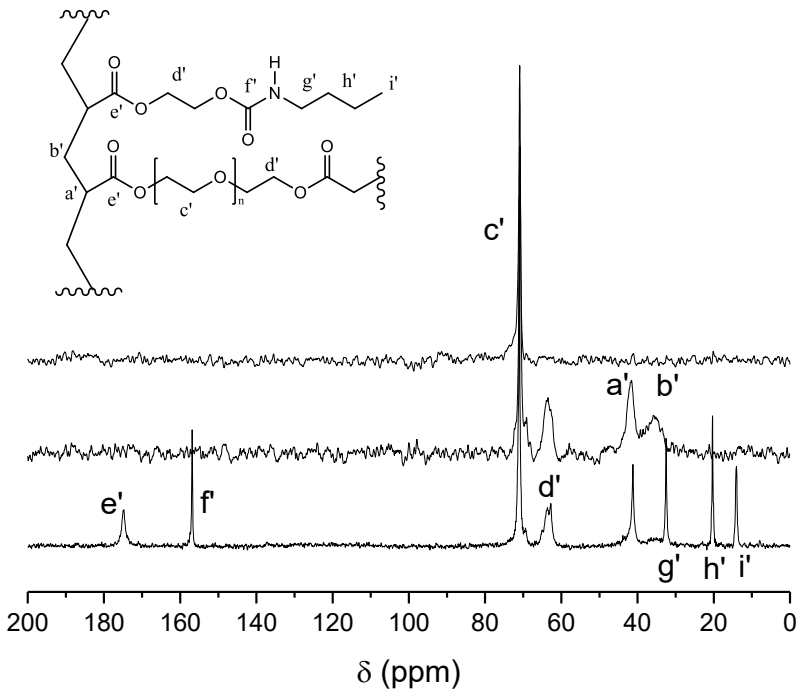

Figure 4.3. ^{13}C MAS spectrum for cured (bottom) sample 9 network, and ^{13}C CP-MAS spectrum for sample 1 with cross-polarization time τ_{cp} at 0.5ms (second), and 10ms (top).

The corresponding chromatographic analyses of hydrolyzed networks also show that the molecular weight distribution (M_w, M_n) of the acrylate backbone chains is a characteristic parameter of UV-cured PEGDA-based networks. The PAA component of the different hydrolysates were

characterized to provide the M_w, M_n and PDI values shown in Table 4.1. PEG was measured with MS detection, assuming equal MS sensitivity; PEG has a M_n value of 488 Da.

Sample No.	Monoacrylate	w_{PEGDA}	Conversion* (%)	PAA		
				M_n (kDa)	PDI	n(PAA)
1	-	1	92±5	16.7	1.6	232
2	HEA	0.9	91±5	9.0	3.2	125
3	HEA	0.7	95±5	7.0	2.1	97
4	HEA	0.5	92±5	13.8	3.7	192
5	HEA	0.3	91±5	17.7	5.7	246
6	HEA	0.1	90±5	36.3	3.6	504
7	BACOEA	0.9	92±5	16.2	2.9	225
8	BACOEA	0.7	93±5	20.2	2.7	281
9	BACOEA	0.5	91±5	13.8	3.0	192
10	BACOEA	0.3	91±5	17.0	3.6	236
11	BACOEA	0.1	89±5	9.9	3.1	138

Table 4.1 The formulation of all the samples used in this study. *The conversion degree is calculated through IR peak around 810cm^{-1} (the acrylate C-H bending mode)

The M_w and M_n of the PAA backbone chains appear to be independent of the concentration of di-functional monomer. In general, these values depend on the polymerization rate and on the bimolecular termination rate[23], which is probably similar for the different samples.

Network Hydrogen Bonding Analyses. Several methods can be used to detect the presence of hydrogen bonding in polymeric networks. Among them, FTIR is the most frequently used due to its easy implementation. As mentioned in previous literature[12, 14], there are essentially two kinds of hydrogen bonding presented in our systems. One is hydrogen bonding between hydroxyl groups (or amide groups in BACOEA-PEGDA networks), the other is the interaction between the hydroxyl groups (or amide group) and carbonyl groups, as illustrated in Figure 4.4. This results in shift of IR peaks corresponding to O-H stretching band (3500 cm^{-1}) and carbonyl stretching band (1730 cm^{-1}), as has been determined in a previous study.[14]

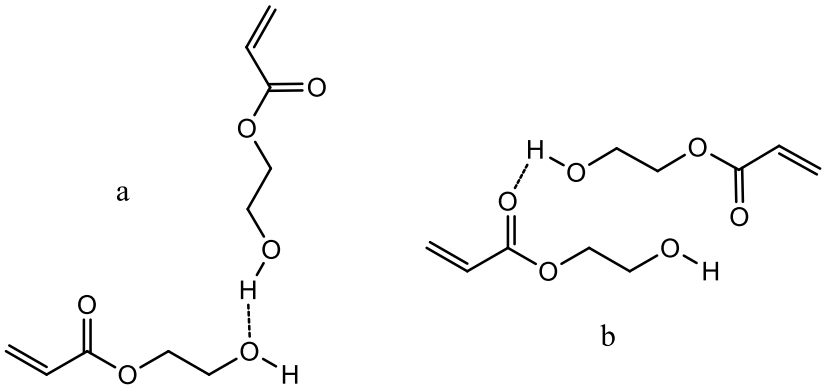

Figure 4.4 Two possible hydrogen bonding in hydroxyalkyl acrylate (HEA)

Figure 4.5 displays the above mentioned two IR bands for HEA-PEGDA networks. As expected, multiple features are visible in both regions. By fitting these two bands, the shoulder peaks are found exactly at the position corresponding to hydrogen bonding induced species as reported previously (3350 cm^{-1} for H-bonded $\upsilon_{str}(O-H)$, 1710 cm^{-1} for H-bonded $\upsilon_{str}(C=O)$) [14]. Hence, the presence of hydrogen bonding in the HEA-PEGDA networks is demonstrated by FTIR analyses.

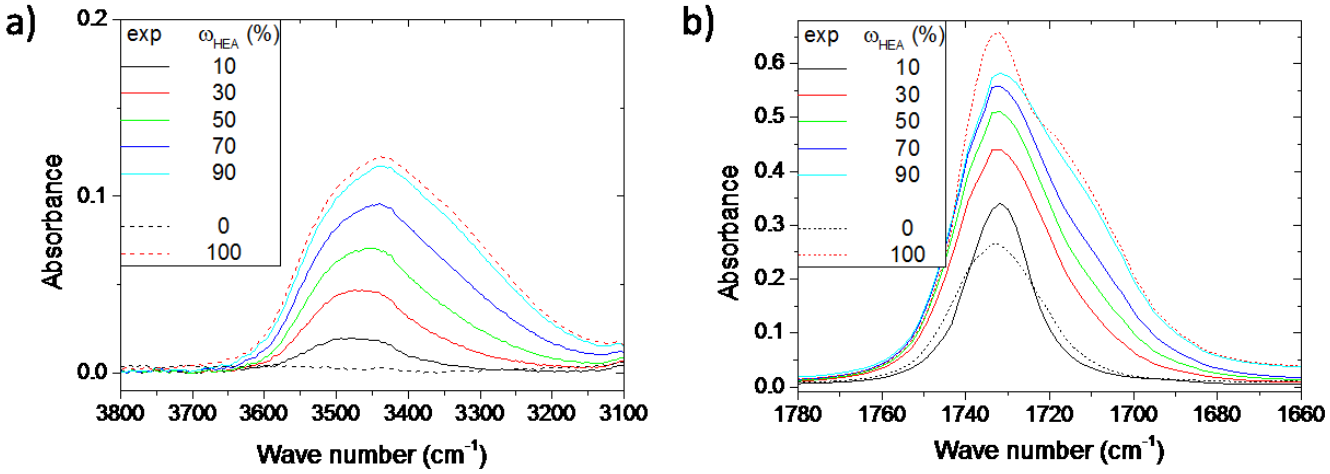

Figure 4.5. IR spectra of HEA-PEGDA networks. (a) O-H stretching band area. (b) carbonyl stretching band area.

In the BACOEA-PEGDA system, similar hydrogen bonding induced IR peak shifts can be observed for N-H stretching and carbonyl stretching modes as reported previously (3370 cm^{-1} for H-bonded $\upsilon_{str}(N-H)$, and 1710 cm^{-1} for H-bonded $\upsilon_{str}(C=O)$). [12] However, detailed analyses of the relative area integrated under these peaks shows different pictures for the two systems. This difference would be further discussed in the next section.

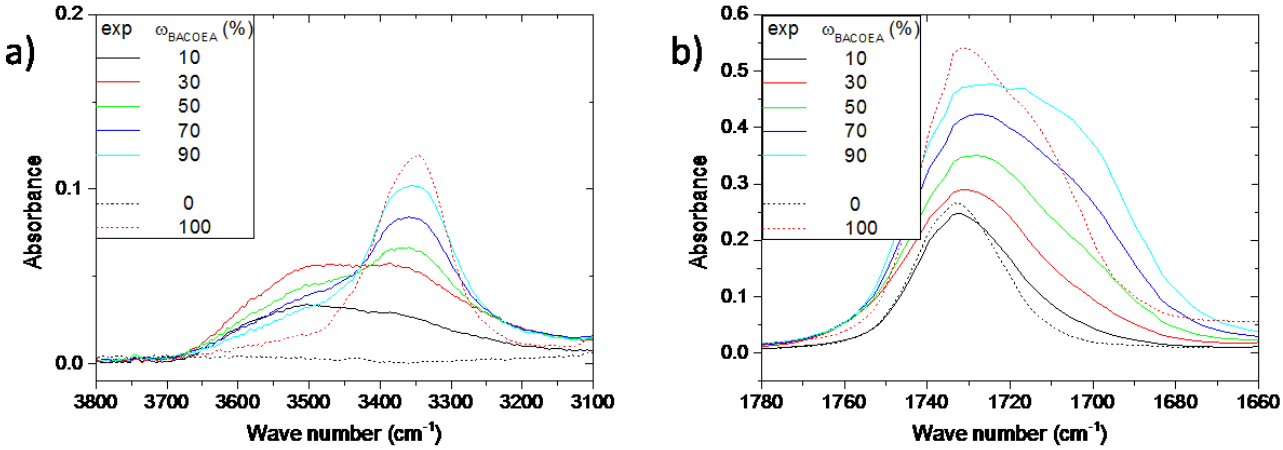

Figure 4.6. IR spectra of BACOEA-PEGDA networks. (a) N-H stretching band area. (b) carbonyl stretching band area.

As routinely used in analyzing the rigid part of materials, the single pulse excitation (SPE) FID experiment is very sensitive to the rigid fraction of the material though dead time of the receiver prevents recording of the initial part of the FID in this analyses. As shown in Figure 4.7, the temperature-dependence of the T_2 relaxation curve for PEGDA-BACOEA networks becomes much more pronounced with increasing copolymer weight ratio (w_{BACOEA}). Indeed, no observable change in the relaxation curve could be found for material with low w_{BACOEA}. Material with high w_{BACOEA} contains an extremely short relaxation components (below 50 μs), and this short relaxation component only disappears at high temperature. Though the relative high T_g values for these networks with high w_{BACOEA} means the anisotropic chain dynamics still influence the T_2 values, when measured at low temperature. However, by comparing to the PEGDA-HA network, the huge differences in relaxation time (a factor of 5 times) between T_2(20 ℃) and T_2(70 ℃) indicates this short component was also induced by hydrogen bonding. A similar situation also occurred for the PEGDA-HEA system.

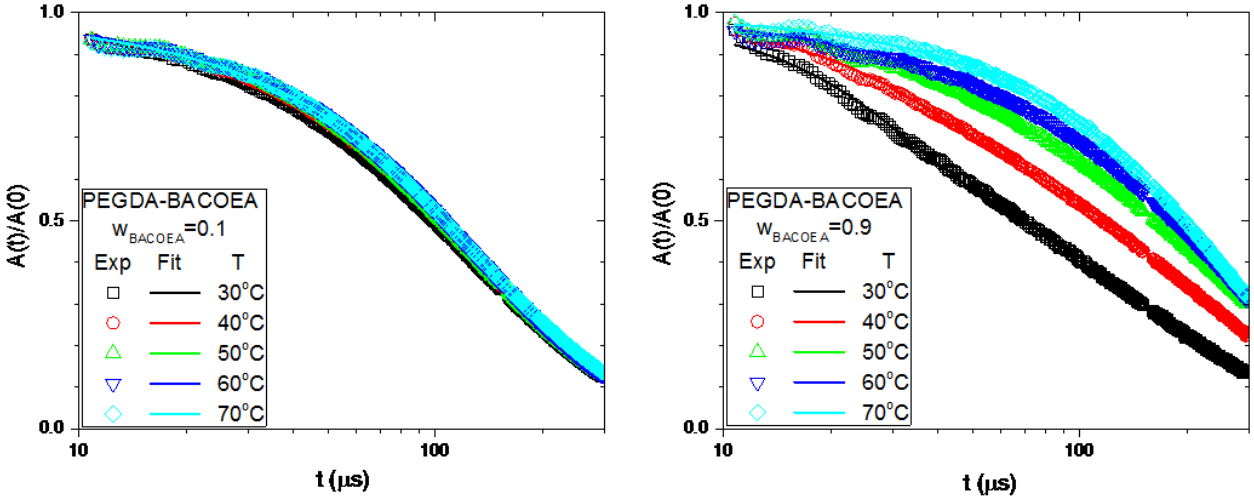

Figure 4.7. Normalized T_2 relaxation decay of PEGDA-BACOEA gels at different temperature. (left: w_{HEA}=0.1, right: w_{HEA}=0.9). The points represent the measured data and the lines are the corresponding fitting.

Figure 4.8 shows SPE FID relaxation profiles for each sample at 70°C. Since these relaxation curves could be fitted with a single component, while the fitted T_2 value does not alter much once the temperature is above 70°C, it is safe to say that these relaxation profiles are free of any hydrogen-bonding effect and above the high temperature rubbery plateau.[24] The relaxation curves for PEGDA-HEA and PEGDA-BACOEA are quite different for similar copolymer ratio, this may indicate certain differences in their network structure, which will be explored in detail below.

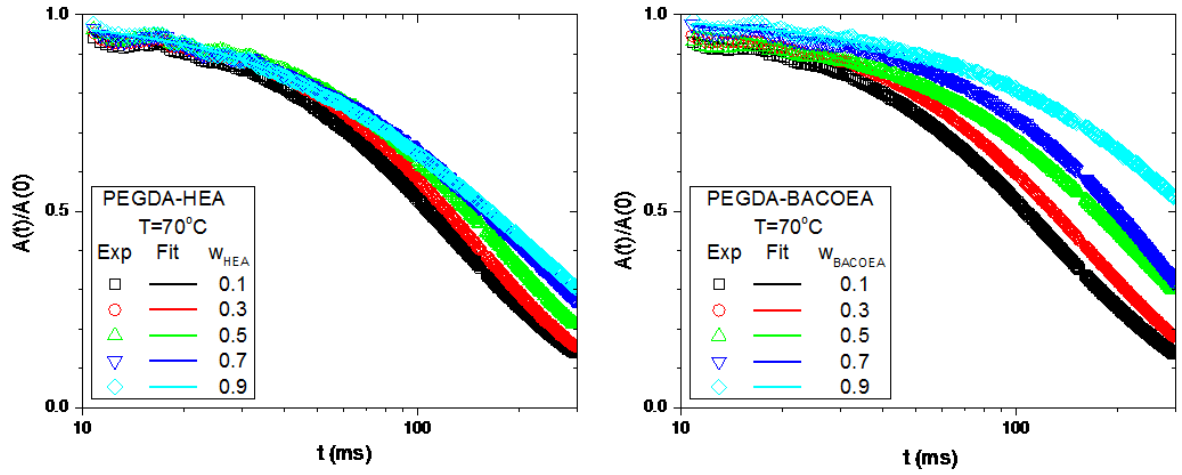

Figure 4.8. Normalized T_2 relaxation decay of PEGDA-HEA gels at 70°C with different w_{HEA} or w_{BACOEA} measured using SPE. The points represent the measured data and the lines are the corresponding fitting.

Hydrogen Bonding Induced Cluster Formation in Networks. To obtain structural information for all the networks used in this study, the reactivity ratio r_1 (for monoacrylate) and r_2 (for PEGDA) were estimated on the basis of the Alfrey-Price $Q - e$ scheme[25]. In this scheme, "Q" is a measure of reactivity arising from resonance stabilization, while "e" is a measure of polarity of the monomer due to the effect of functional groups on the vinyl group. The Q and e values used in this study for HA/HEA/BACOEA (monomer 1), and for PEGDA (monomer 2) are shown in Table 4.2. Since not all the Q and e values are available, several approximation were implemented; the values for glycidyl acrylate, 2-ethylhexyl acrylate and 2-nitrobutyl acrylate were used for PEGDA, HA and BACOEA, respectively[26].

Monomer 1	Q_1	e_1	r_1	Monomer 2	Q_2	e_2	r_2
HA	0.37	+0.24	0.99	PEGDA	0.48	+1.28	0.34
HEA	0.75	+0.65	2.35	PEGDA	0.48	+1.28	0.29
BACOEA	0.69	+1.09	1.77	PEGDA	0.48	+1.28	0.55

Table 4.2. Reference Q, e values for monomers used in this study, and the calculated relativity ratios r in the corresponding copolymerization process.

Hence, the reactivity ratio r, which is the ratio between k_{11} (the rate constant for polymerization between species 1) and k_{12} (the rate constant for polymerization between species 1 and species 2) could also be calculated as following,

$$r_1 = Q_1 \exp(-e_1(e_1 - e_2))/Q_2$$

$$r_2 = Q_2 \exp(-e_2(e_2 - e_1))/Q_1$$

In this calculation, we assume that free and pendant double bonds have equal reactivity. The accuracy of this assumption degrades at extremely low and high levels of conversion.[27]

As shown in Table 4.2, the theoretically calculated reaction rate parameters for the radical polymerization suggest strong preference for copolymerization over polymerization between HEAs could be found in the PEGDA-HEA system, due to the large r_1 value in this process. It also implies a potential formation of HEA clusters. While the other two systems may have a relative milder clustering in comparison to the PEGDA-HEA network.

Detailed analyses of IR spectra also indicates the formation of HEA clusters in case of the PEGDA-HEA network. By fitting these features shown in Figure 4.5 and Figure 4.6 (see example in Figure 4.9), the relative ratio between free and hydrogen bonded species can be estimated by comparing

the relative area under each component. As shown in Table 4.3, as compared to the relative unchanged ratio between free O-H and hydrogen bonded O-H with increasing ω_{HEA} for PEGDA-HEA networks, its counterpart for PEGDA-BACOEA networks decreases dramatically with increasing BACOEA content. Since it is statistically more favorable to have more hydrogen bonded O-H (namely, more HEA are presented near HEA) when increasing ω_{HEA} in the network. The formation of HEA clusters can keep the ratio between free O-H species and hydrogen bonded O-H species relative unchanged, since this cluster forming mechanism favors the hydrogen bonded O-H even when ω_{HEA} is relatively low in the initial formulation, which in turn keeps the ratio between the number of monomers in the core (hydrogen bonded O-H) and outer layers (free O-H) of the HEA cluster stable. This situation would persist until a threshold of ω_{HEA} is reached, in which the statistical probability of HEA encountering itself becomes so large that the effect of clustering is no longer visible.

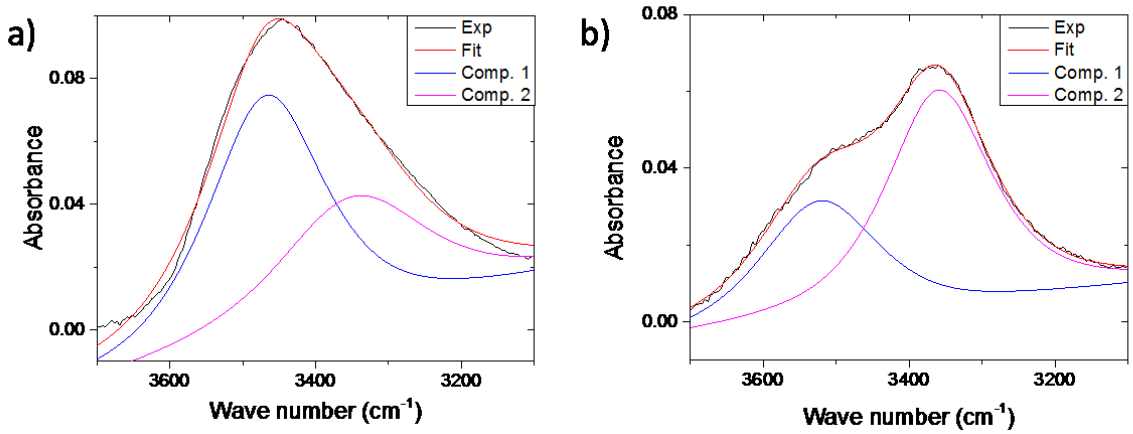

Figure 4.9. IR spectral fitting of O-H (N-H) stretching band for sample 4 (PEGDA:HEA=50:50) and samples 9 (PEGDA:BACOEA=50:50)

As it can be sensitive to ^{1}H-^{1}H proximities in the solid state, the ^{1}H-^{1}H DQ-SQ correlation NMR was used to investigate the potential clustering formation in these polymeric networks. In a DQ-SQ correlation spectrum dipolar coupled nuclei with chemical shifts f_1 and f_2 are excited to form double quantum coherences using a double quantum excitation pulse sequence block such as Back-to-Back (BABA) based C7 sequence.[28] The double quantum coherences evolve with the sum frequency of the two coupled nuclei (f_1+f_2) during the evolution period t_2 and are then converted back to single quantum coherence using the same sequence phase shifted by 90° with respect to the excitation block. These single quantum coherences evolve at the respective frequencies f_1 and

f_2 for each nucleus during the detection period t_2, This gives rise to cross peaks at $(f_1 + f_2, f_1)$ and $(f_1 + f_2, f_2)$ in a two dimensional spectrum. The selective observation of spatially proximal ^{1}H nuclei leads to less overlap of the spectral peaks making assignment easier.

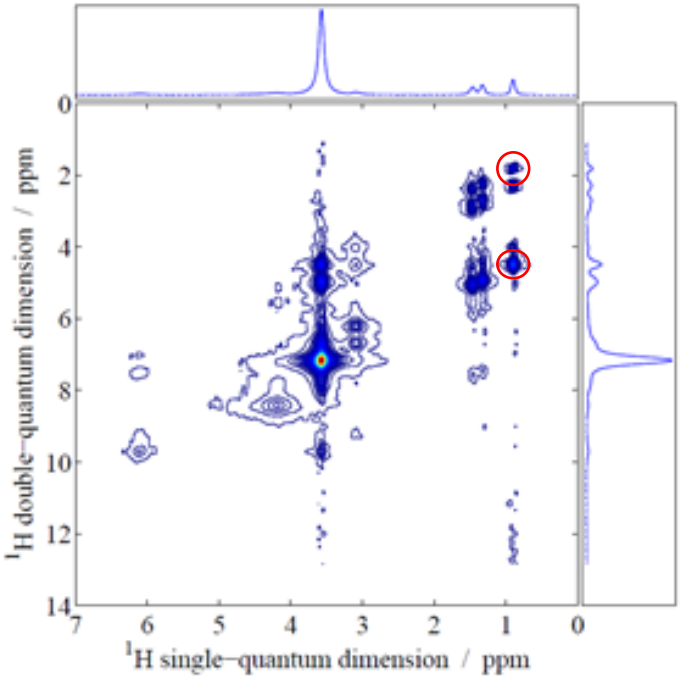

Figure 4.10. DQ-SQ correlation spectrum of PEGDA-BACOEA (w_{BACOEA}=50%) at 80°C.

As shown in Figure 4.10, in PEGDA-BACOEA network with w_{BACOEA}=50%, the crosspeak (0.9 ppm, 4.6 ppm) between PEG units and BACOEA shows a stronger intensity compared to autopeak (0.9 ppm, 1.8 ppm) of BACOEA itself. This indicates that there is no preference for clustering during curing for this network. Note that PEGDA and BACOEA were well mixed in the formulation. However, it is not the case in PEGDA-HEA system. As shown in Figure 4.11, the stronger autopeak (1.7 ppm, 3.4 ppm) of HEA in comparison to its crosspeak (1.7 ppm, 5.4 ppm) to PEG suggested a preferred presence of HEA chain besides HEA chain, which would result in the formation of HEA cluster in the network.

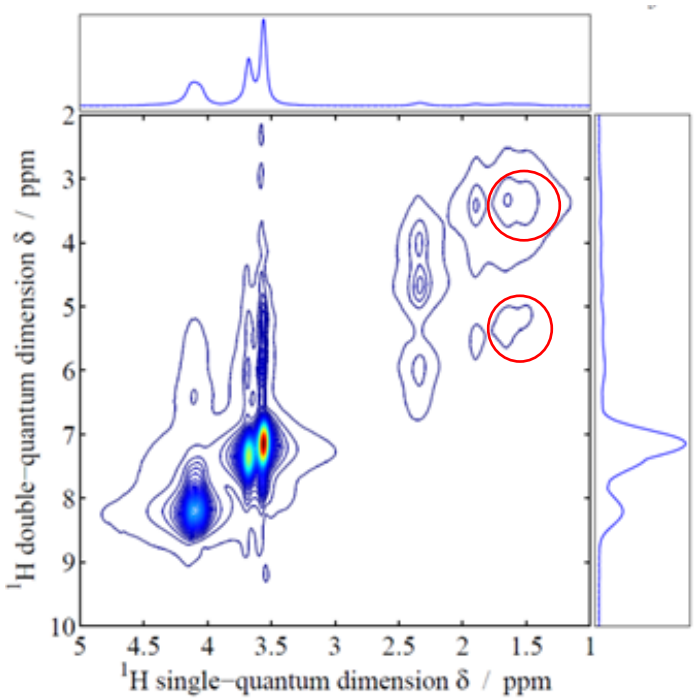

Figure 4.11. DQ-SQ correlation spectrum of PEGDA-HEA (w_{HEA}=50%) at 80°C.

On the other hand, PEGDA-HA also shows a similar situation as PEGDA-BACOEA (autopeak (1.4 ppm, 2.8 ppm), cross peak (1.4 ppm, 5.1 ppm) in Figure 4.12).

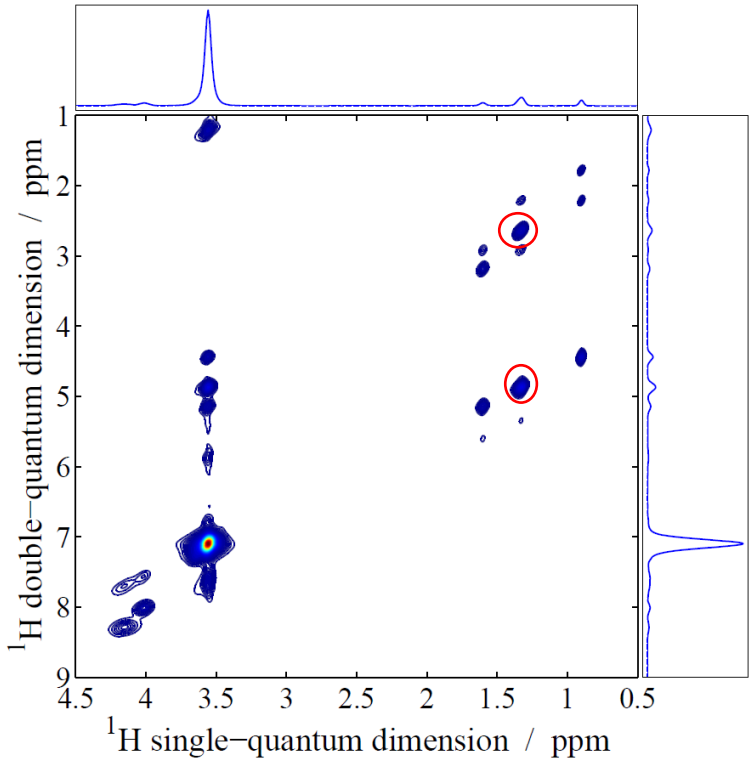

Figure 4.12. DQ-SQ correlation spectrum of PEGDA-HA (w_{HA}=50%) at 80°C

Since the formation of clusters occurs during the curing stage this is good evidence for possible pre-organization induced by hydrogen bonding. For PEGDA-BACOEA networks, the effect was weaker than for PEGDA-HEA networks at low content, according to the IR analyses of these networks. This is possibly because N-H tends to form H-bonds with C=O groups while PEGDA also contains such groups in its structure. As also shown in DQ-SQ NMR analyses, the distinctive correlation pattern in PEGDA-HEA networks, as compared to PEGDA-BACOEA and PEGDA-HA networks when ω_{PEGDA} is high, indicates a different curing mechanism possibly involving pre-organization of the monoacrylate during sample preparation stage. These data are consistent with the theoretically calculated reaction rate presented previously. It should also be mentioned that high homo-polymerization reaction rates (k_{11}) would also favor the formation of clustering. However, as mentioned in several previous studies[12, 14], the relative larger k_{11} (as calculated in Q-e scheme) is also a direct outcome of the presence of H-bonding in the network.

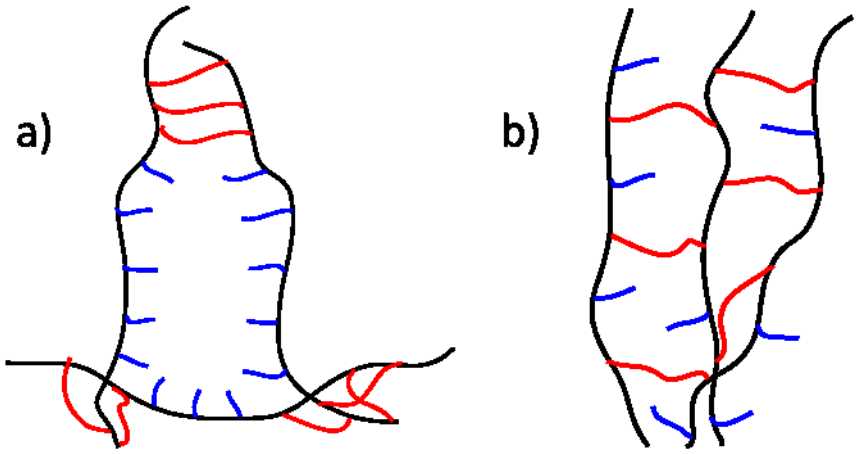

Figure 4.13. The proposed porous structure of the networks in this study (a: PEGDA-HEA; b:PEGDA-HA (or PEGDA-BACOEA), black: polyacrylate backbone bond; red: PEGDA crosslink; blue: monoacrylate (HEA/BACOEA/HA))

As suggested in Figure 4.13, the corresponding network generated by pre-organization of monoacrylate may potentially have a different pore size distribution, which would effectively alter the diffusion pattern of small solute in this network comparing to the network without monoarylate pre-organization. The effect of this structural arrangement would be further exploited in detail in the next chapter.

Effect of Hydrogen-Bond on Molecular mass of network chains. As mentioned in the previous chapter, the mean molar mass of network chains between chemical crosslinks and trapped chain entanglements, M_{c+e}, can be separately determined by both dynamic mechanical analysis (DMA) and NMR T_2 relaxometry analyses. However, due to the relatively high T_g values for samples with high monoacrylate ratio in this case, NMR approach cannot be used to evaluate M_{c+e} in this scenario, hence, M_{c+e} for all the samples in this study were only calculated from DMA data. For details of the calculation see Chapter III. Figure 4.14 shows the storage modulus E' for all the samples across a temperature range from -50 to 100°C

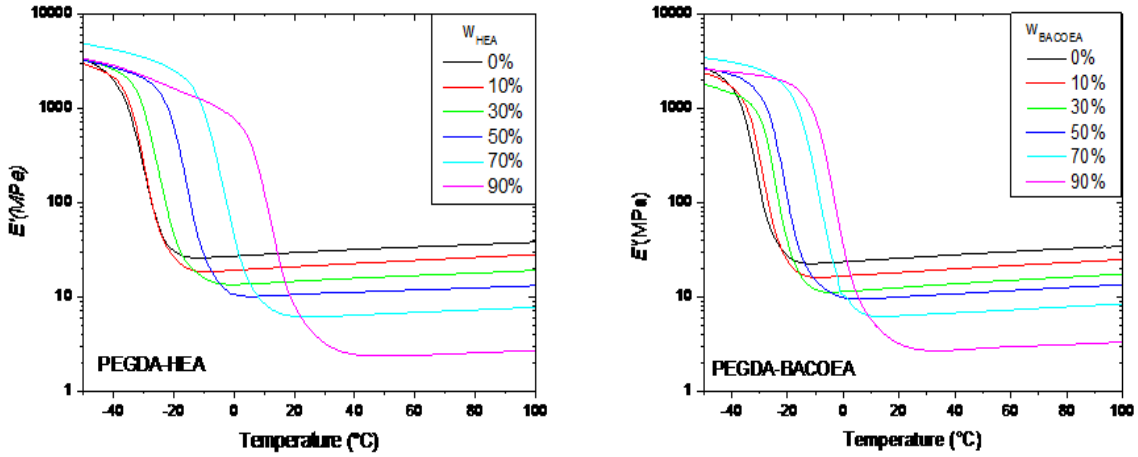

Figure 4.14. Storage modulus, *E'*, of cured acrylate networks (left: PEGDA-HEA; right: PEGDA-BACOEA, measured by DMA with increasing ω_{HEA} or ω_{BACOEA}.

As shown in Figure 4.15, a similar changing pattern in M_{c+e} can be found for all three network series when increasing the monoacrylate weight percentage in the initial curing formulation. This implies the same network behavior described in the previous chapter. The zip-like (or alternating comb-like) polyacrylate pattern does not change significantly when altering the monoacrylate used in the formulation.

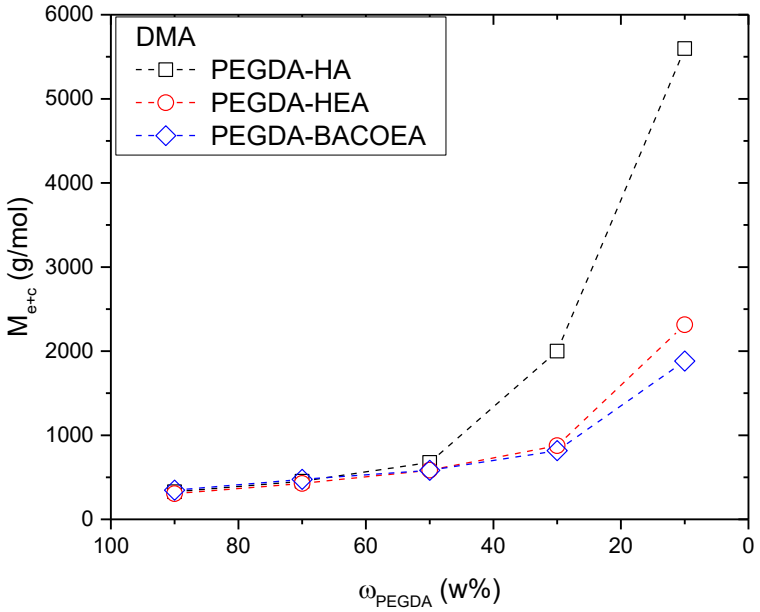

Figure 4.15. Mean molar mass between crosslinks and trapped chain entanglements, M_{c+e}, as a function of HA weight fraction, ω_{HA}, obtained by evaluating of experimental results.

Mono-acrylate	ω_{PEGDA}	IR[1]				DMA		NMR	
		O-H (N-H) stretching band int. fraction		C=O stretching band int. fraction		Storage Modulus at 70°C (MPa)	M_{e+c} (DMA) (g/mol)	FID	
		Free	H-bond induced	Free	H-bond induced			$T_{2,avg}$ (30°C) (μs)	$T_{2,avg}$ (70°C) (μs)
HEA	0.9	0.62	0.38	0.98	0.02	25.1	306.0	141.2	150.8
HEA	0.7	0.65	0.35	0.90	0.10	17.3	426.2	113.6	169.2
HEA	0.5	0.60	0.40	0.82	0.18	12.0	583.7	70.0	198.0
HEA	0.3	0.55	0.45	0.78	0.22	7.0	876.1	49.2	225.9
HEA	0.1	0.51	0.49	0.68	0.32	2.5	2314.8	43.0	227.4
BACOEA	0.9	0.57	0.43	0.90	0.10	22.1	346.9	140.8	146.4
BACOEA	0.7	0.50	0.50	0.81	0.19	15.5	474.9	142.8	180.4
BACOEA	0.5	0.41	0.59	0.73	0.27	12.0	583.4	87.4	255.2
BACOEA	0.3	0.32	0.68	0.62	0.38	7.5	817.5	79.7	268.7
BACOEA	0.1	0.25	0.75	0.51	0.49	3.0	1881.9	66.4	469.2

Table 4.3. Results of networks characterized by FTIR, T_2 relaxometry and mechanical analyses.

[1] For PEGDA-HEA networks, the free O-H stretching band is at *c.*3500 cm^{-1}, the H-bonded feature is at *c.*3350 cm^{-1}, the free C=O stretching band is observed *c.*1730 cm^{-1}, the H-bonded at *c.*1710 cm^{-1}. For PEGDA-BACOEA, the free N-H stretching band is observed *c.*3520 cm^{-1}, and the H-bonded feature *c.*3370 cm^{-1}.

The weaker decrease in M_{c+e} for samples with lower ω_{PEGDA} in PEGDA-HEA and PEGDA-BACOEA networks can be attributed to the formation of hydrogen bonding as discussed previously. To a certain extent H-bonding would restrict the polymer chain's movement, and act as a physical 'crosslink' in the network.

4.4 CONCLUSIONS

In this study, three different networks formed from different monoacrylates were synthesized via UV-initiated photo-polymerization. Their corresponding structures and polymer chain dynamics were investigated via FTIR, DMTA, LF ^{1}H NMR relaxometry and HF ^{1}H NMR DQ-SQ correlation spectroscopy.

The theoretically calculated reaction rate ratio of copolymerization indicates a cluster formation in system like PEGDA-HEA, this prediction is consistent with the observation in FTIR and DQ-SQ NMR correlation spectra. Hence, we propose that the H-bonding induces the pre-organization of the monoacrylate during the sample preparation. This is the direct observation of the occurrence of H-bonding induced pre-organization in UV-curing process. At the same time, it was also found that some deviation in the networks made from monoacrylates with urethane-type H-bonding (e.g. BACOEA) when ω_{PEGDA} is high in the formulation. Since previous studies provided indirect evidence for monoacrylate pre-organization in similar monoacrylates, this discrepancy may be explained as arising from the interaction between PEGDA and BACOEA, due to the presence of a similar functional group in PEGDA that is involved in the formation of H-bonds. This observation clearly demonstrates the important role of hydrogen bonding type in the occurrence of monoacrylate pre-organization during UV initiated photo-polymerization processes.

References:

1. R. Barbucci, Hydrogels biological properties and applications. (Springer,, Milan, 2009), pp. xi, 197 p.
2. N. Garylord, U. S. P. Office, Ed. Oxygen-permeable contact lens composition, methods and article of manufacture (Polycon Laboratories, United States, 1974).
3. N. Garylord, U. S. P. Office, Ed. Method for correcting visual defects, compositions and articles of manufacture useful therein (Syntex (U.S.A.) Inc., United States, 1978).
4. A. A. F. Birdsall, J. K.; Jones, D. P.; Polmanteer, K. E., U. S. P. Office, Ed. (Dow Corning Corporation, United States, 1978).
5. D. D. Mitchell, U. S. P. Office, Ed. (Dow Corning Corporation, United States, 1984).
6. J. M. Weissman, H. B. Sunkara, A. S. Tse, S. A. Asher, Thermally switchable periodicities and diffraction from mesoscopically ordered materials. Science 274, 959 (Nov 8, 1996).
7. T. R. Hoare, D. S. Kohane, Hydrogels in drug delivery: Progress and challenges. Polymer 49, 1993 (Apr 15, 2008).
8. X. J. Liao, G. S. Chen, M. Jiang, Hydrogels locked by molecular recognition aiming at responsiveness and functionality. Polym Chem-Uk 4, 1733 (2013).
9. C. Decker, K. Moussa, Real-Time Kinetic-Study of Laser-Induced Polymerization. Macromolecules 22, 4455 (Dec, 1989).
10. C. Decker, K. Moussa, A New Class of Highly Reactive Acrylic-Monomers .2. Light-Induced Copolymerization with Difunctional Oligomers. Makromol Chem 192, 507 (Mar, 1991).
11. K. Moussa, C. Decker, Light-Induced Polymerization of New Highly Reactive Acrylic-Monomers. J Polym Sci Pol Chem 31, 2197 (Aug, 1993).
12. J. F. G. A. Jansen, A. A. Dias, M. Dorschu, B. Coussens, Fast monomers: Factors affecting the inherent reactivity of acrylate monomers in photoinitiated acrylate polymerization. Macromolecules 36, 3861 (Jun 3, 2003).
13. J. F. G. A. Jansen, A. A. Dias, M. Dorschu, B. Coussens, Effect of preorganization due to hydrogen bonding on the rate of photoinitiated acrylate polymerization. Photoinitiated Polymerization 847, 127 (2003).
14. T. Y. Lee, T. M. Roper, E. S. Jonsson, C. A. Guymon, C. E. Hoyle, Influence of hydrogen bonding on photopolymerization rate of hydroxyalkyl acrylates. Macromolecules 37, 3659 (May 18, 2004).
15. H. Kilambi, J. W. Stansbury, C. N. Bowman, Deconvoluting the impact of intermolecular and intramolecular interactions on the polymerization kinetics of ultrarapid mono(meth)acrylates. Macromolecules 40, 47 (Jan 9, 2007).
16. I. Ando, T. Asakura, Solid state NMR of polymers. Studies in physical and theoretical chemistry (Elsevier, Amsterdam ; New York, 1998), pp. xvi, 1000 p.
17. C. Brosseau, A. Guillermo, J. P. Cohenaddad, Nuclear-Magnetic-Resonance Approach to Properties of Poly(Ethylene Oxide) Poly(Methyl Methacrylate) Blends .1. Chain Dynamics and Free-Volume. Polymer 33, 2076 (1992).
18. M. Andreis, J. L. Koenig, Application of Nmr to Crosslinked Polymer Systems. Advances in Polymer Science 89, 69 (1989).
19. V. M. Litvinov, A. A. Dias, Analysis of network structure of UV-cured acrylates by H-1 NMR relaxation, C-13 NMR spectroscopy, and dynamic mechanical experiments. Macromolecules 34, 4051 (2001).
20. R. Graf, D. E. Demco, S. Hafner, H. W. Spiess, Selective residual dipolar couplings in cross-linked elastomers by H-1 double-quantum NMR spectroscopy. Solid state nuclear magnetic resonance 12, 139 (Sep, 1998).

21. J. Gottwald, D. E. Demco, R. Graf, H. W. Spiess, High-Resolution Double-Quantum Nmr-Spectroscopy of Homonuclear Spin Pairs and Proton Connectivities in Solids. Chem Phys Lett 243, 314 (Sep 15, 1995).
22. K. Saalwachter, Robust NMR Approaches for the Determination of Homonuclear Dipole-Dipole Coupling Constants in Studies of Solid Materials and Biomolecules. Chemphyschem : a European journal of chemical physics and physical chemistry 14, 3000 (Sep 16, 2013).
23. J. A. Burdick, T. M. Lovestead, K. S. Anseth, Kinetic chain lengths in highly cross-linked networks formed by the photoinitiated polymerization of divinyl monomers: A gel permeation chromatography investigation. Biomacromolecules 4, 149 (Jan-Feb, 2003).
24. K. Matyjaszewski et al., Polymer science a comprehensive reference. (Elsevier, Amsterdam, 2012), pp. 10 vols.
25. G. G. Odian, Principles of polymerization. (Wiley-Interscience, Hoboken, N.J., ed. 4th, 2004), pp. xxiv, 812 p.
26. J. Brandrup, E. H. Immergut, E. A. Grulke, Polymer handbook, 4th edition. (Wiley, New York ; Chichester, ed. 4th, 2004).
27. J. G. Kloosterboer, G. F. C. M. Lijten, H. M. J. Boots, Network Formation by Chain Crosslinking Photopolymerization and Some Applications in Electronics. Makromol Chem-M Symp 24, 223 (Jan, 1989).
28. K. Saalwachter, Proton multiple-quantum NMR for the study of chain dynamics and structural constraints in polymeric soft materials. Prog Nucl Mag Res Sp 51, 1 (Aug 30, 2007).

Chapter V

Spectroscopic Analyses of H-bonding Effect on Drug Diffusion inside Hydrogel Matrices

5.1 INTRODUCTION:

Hydrogels for controlled drug delivery have received increased attention due to their potential in drug eluting contact lenses and in the pharmaceutical field, because of the anticipated biocompatibility of this class of materials. In most controlled drug delivery systems (DDS), several effects play significant roles in determining the overall drug release rate of the system, e.g. drug diffusion, polymer swelling and polymer degradation. Based on release mechanisms, DDS could be further categorized into diffusion-controlled systems, solvent-activated systems, chemically controlled systems and magnetically controlled systems. Among them, the diffusion-controlled system is currently one of most popular devices used in the pharmaceutical industry.[1] As shown in the **Figure 5.1**, two DDS types, reservoir system and monolithic system, are classified under the diffusion-controlled category. In a reservoir system, a drug core is present in powdered or liquid form, and a layer of non-biodegradable polymeric material, through which the drug slowly diffuses, surrounds the core. When the core is saturated, a constant concentration gradient of drug is maintained in the membrane, which results in a zero-order drug release rate. Hence, the diffusion rate of the drug and its release rate into the bloodstream would be governed by the properties of the drug and the polymer membrane. In order to maintain uniformity of drug delivery, the thickness of the polymer must be consistent. There are several problems regarding the implementation of this device. One of them is the difficulty on fabricating reliable membranes, since pinhole defects and cracks in the membrane can lead to a large amount of drug suddenly being released into the bloodstream (known as 'dose dumping'). [2, 3]

The monolithic systems are designed to avoid these problems. In this case, the drug is uniformly distributed throughout the polymer matrix. Therefore, the polymer matrix in this case acts as both a storage medium and a mediator of diffusion. Monolithic devices typically exhibit an initial burst of release from the surface. This release rate will decrease with time as drug that is deeper inside the monolith must diffuse to the surface. Since it has longer distance to travel, and the quadratic relation between distance and time becomes important.[4] By using specially coated wedge, cone, or hemisphere monoliths, it is possible to substantially reverse this geometric factor in order to provide near-zero-order release, however, this kind of shape design significantly increase the difficulty on fabricating such devices.[3]

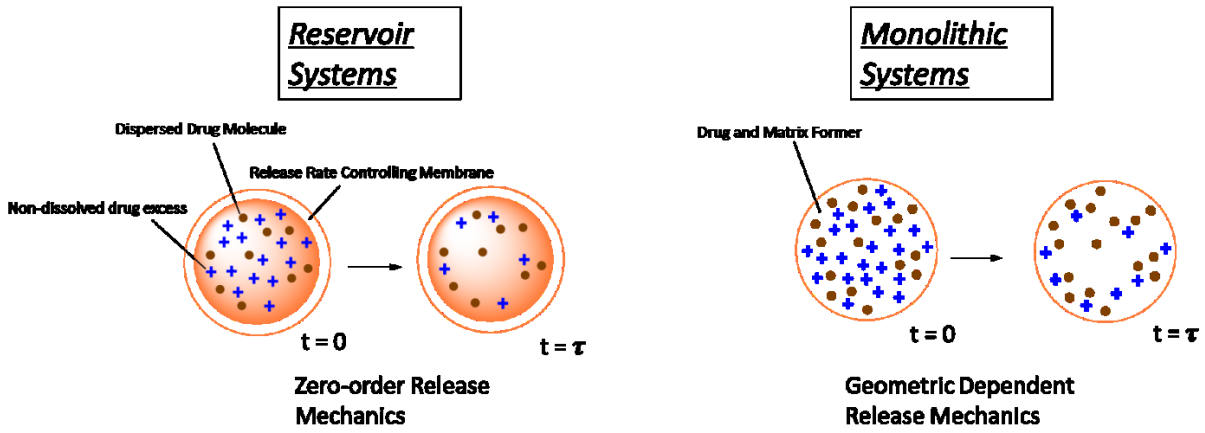

Figure 5.1. Two major types of diffusion-controlled drug delivery vehicles.

There are many reports of studies into the relationship between the drug's diffusion and the hydrogels' structures and physical properties. A mathematical description of mass transport in diffusion-controlled drug delivery systems was given for ideal systems.[4] While fluorescence correlation spectroscopy (FCS) has frequently been used to investigate diffusion processes of small dye molecules inside hydrogels,[5, 6] these results largely deviate from the real situation due to the low solute concentration limit. Meanwhile macroscopic mechanical diffusion analysis[7] also has been regularly implemented in solute diffusion studies. However, a systematic study about the effect of tailored chemical structure of the gel matrix on the diffusivity of small solute within it is still missing, due to rather complicated morphological and topological properties[8] these hydrogel matrices possess.

As one of the most powerful techniques in analyzing materials, NMR is frequently used to extract structural information of molecules using chemical shift specified spectral analyses. NMR relaxometry offers great insight about the molecular dynamics inside the target system. Recently, the development in Pulsed Field Gradient (PFG) makes NMR even an ideal tool to probe self-diffusivity of solutes inside polymeric systems.[9] The basic principle behind the PFG NMR was laid down by E. Stejskal and J. Tanner in 1965.[10] By introducing a pulsed field gradient into the basic spin echo sequence, one can probe the diffusion phenomenon inside the liquid sample by varying one parameter (normally diffusion time or gradient strength) in the Stejskal-Tanner equation. Some additional caution should be taken into account for macromolecular systems, due to the rather complicated evolution of the magnetization.[11, 12] to date the experiment has been

applied into various diffusion studies ranging from small organic molecules to large polymeric nanoparticles.[13]

In a previous study[14], K. Tomić demonstrated the important role that the crosslink density of the gel matrix (M_c) has on the diffusivity of the drug solute (D_{drug}) inside it. It was found that there is still significant interaction between gel matrices and drug solutes even when the calculated mesh size is dramatically larger than the hydrodynamic size of the drug solute. Meanwhile, as suggested by several other studies[5, 15], the presence of hydrogen-bonding in the system can control the diffusion of the solute in certain media including biological systems and polymeric membranes too. Hence, it would be very desirable if this strategy could also be applied into the commercially available hydrogel systems.

In this study, a series of polyacrylate-based hydrogels were synthesized by UV-initiated polymerization. The hydrogen bonding strength in these hydrogels were tailored by varying the monoacrylate copolymer content in the curing formula. Three different monoacrylates were used in this study in order to investigate H-bonding's effect in relation to its position in the side chain of monoacrylate in the network, they are non-H-bonding hexyl acrylate (HA), terminal H-bonding 4-hydroxybutyl acrylate (HBA), and non-terminal bulky H-bonding 2-[[(butylamino)carbonyl]oxy]ethyl acrylate (BACOEA). After confirming the high double bond conversion in these networks by FTIR, they were swollen with a drug analogue (Eosin Y disodium salt) in aqueous solution. Subsequently, these systems were studied by high field ^{1}H NMR diffusometry, low field ^{1}H NMR relaxometry and fluorescence anisotropy measurements. The extracted self-diffusivity of Eosin Y inside these networks from PFG NMR experiments will be discussed in relation to the testing temperature, H-bonding types and the ratio of rigid domain inside the system. The correlation between the H-bonding strength and the diffusivity of Eosin Y inside the network will be discussed, as well as the effect of the bulky side groups on these systems. This is a collaboration work with Dr. Sivaramakrishnan Ramadurai and Prof. Tia Keyes from Dublin City University, all the fluorescence measurement analyses were performed by Dr. Ramadurai.

5.2 EXPERIMENT PART:

Sample Preparation. Polyethylene glycol-700-diacrylate (PEGDA-700), Hexyl acrylate (HA), 4-Hydroxybutyl acrylate (HBA) [1] *(16)*, 2-[[(butylamino)carbonyl]oxy]ethyl acrylate (BACOEA), Photo-initiator: 2,2-Dimethoxy-2-phenylacetophenone (DMPA) was used for synthesis of networks. In this study Eosin Y disodium salt was used as the Drug Analogue to study the diffusion phenomena inside the gel matrices. All the chemicals were obtained from Sigma Aldrich, and used without any further purification.

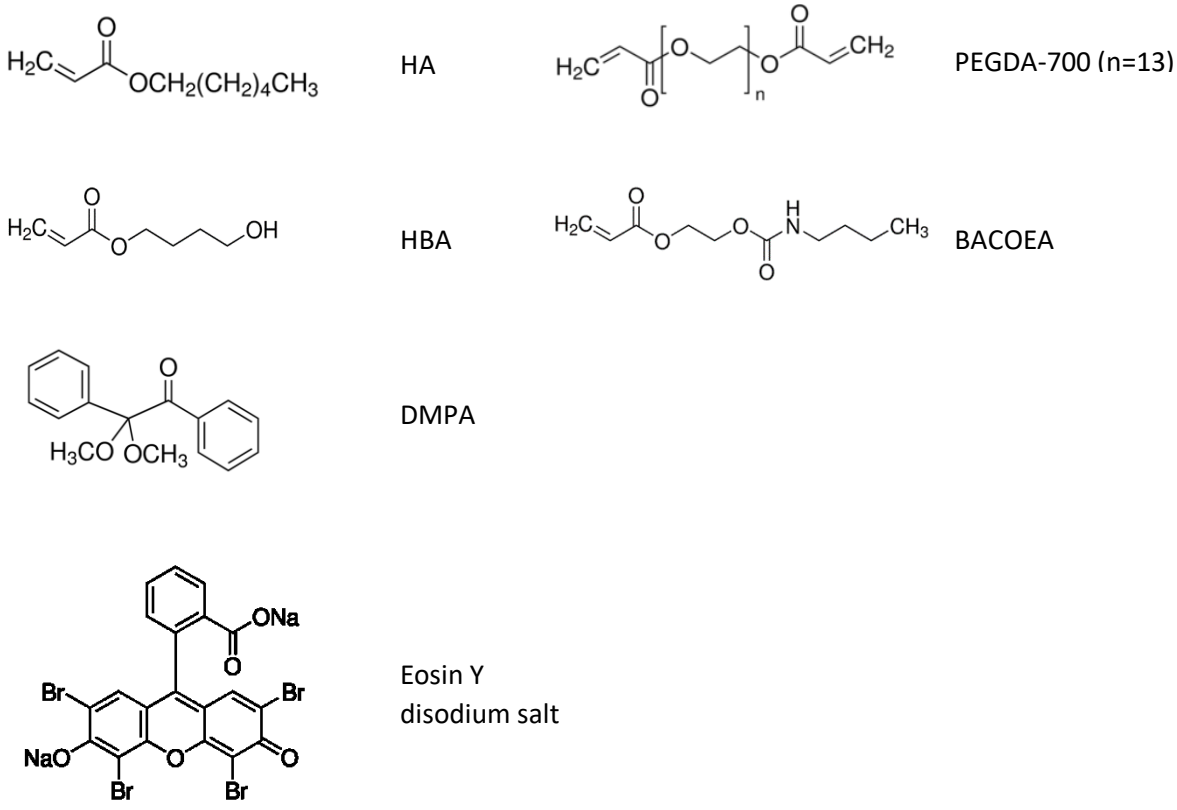

Figure 5.2 Chemical structures of monomers/crosslinks used in the study.

Networks were prepared by UV-curing of the chemicals with the proportion described in **Table 5.1**. (Photo initiator: 10-20 mg 2,2-Dimethoxy-2-phenylacetophenone (DMPA)). The formulation was poured into a petri dish, and then the petri dish was passed through the UV-rig (Heraeus

[1] The reason for using HBA not HEA is to keep similar side chain length of the monoacrylate in the network. It is anticipated that pre-organization of the monoacrylates should be similar, as demonstrated in a previous study, enabling comparisons with the work in the last chapter *(16)*.

Noblelight Fusion UV Inc.'s F300S model, with I300MB irradiator which has a lamp power of 300w/in (120w/cm), 1800 watts total) 30 times. Afterwards the cured film was inverted, and was then passed through the UV-rig a further 30 times. The rim of the resulting film was cut off, and the remaining part with a thickness around 1mm was used for all the tests.

The double bond conversions of the films (which describes the completeness of crosslinking reaction) was measured by FTIR. Results of network characterization are summarized in **Table 5.1**.

Sample No.	Mono-acrylate type	PEGDA:monoacrylate (molar ratio)	Conversion* (%)	EWC (wt%)
1	HA	1:1	92±5	25.8
2	HBA	1:1	91±5	31.1
3	BACOEA	1:1	90±5	29.9

Table 5.1. Sample formulation and results of network characterization

Equilibrium Water Content (EWC). The equilibrium water content (EWC) at room temperature was determined gravimetrically using

$$EWC = 100 * \frac{(W_{wet} - W_{dry})}{W_{wet}} \quad (5.1)$$

After equilibrating samples in water, pieces were removed, lightly blotted to remove excess surface water and then weighed to determine W_{wet}. The dry mass, W_{dry}, was determined after drying samples under vacuum at 80° C for 6 hours (samples reached a constant mass after this time). Measurements for each sample were performed in at least duplicate and calculated EWC varied by less than 1%.

Solid State NMR Analysis of Network Structure. Solid-state magic angle spinning ^{13}C NMR spectra were recorded on a Bruker Avance III 600 MHz spectrometer equipped with a solid standard-bore Magic Angel Spinning probe. 4 mm MAS rotor (80 μL) was used at a spinning rate of 12 kHz. Single pulse excitation (SPE) and cross-polarization (CP) pulse sequences were used in this study. The 90° pulse length was calibrated to 2 μs. The spectra were recorded with two different cross-polarization time values (τ_{cp}) of 0.5 ms and 10 ms, in order to distinguish between rigid and soft part of the material.

^{1}H HRMAS NMR Analysis of Swollen Samples. High resolution magic angle spinning ^{1}H NMR was also implemented in this study to analyze those swollen samples. A Bruker Avance III 600 MHz spectrometer equipped with a HRMAS probe was used to perform this analyses. The test was carried out with a 4 mm HRMAS rotor (12 μL) spinning at 6 kHz. Single pulse excitation (SPE) with a calibrated 90^o pulse length around 8.5 μs was used in this study.

Low Field ^{1}H NMR Relaxometry . The ^{1}H longitudinal magnetization relaxation (T_1 relaxation) and transverse magnetization relaxation (T_2 relaxation) times of these networks were measured on Bruker Minispec MQ20 spectrometer operating at 20 MHz. While inversion recovery pulse sequence was used to analyze T_1 relaxation. The T_2 relaxation decay was measured with the Hahn-echo (HE) pulse sequence (90^o_x—τ_{HE}—180^o_y—τ_{HE}—(acquisition), where $\tau_{HE} \geq 35$ µs) and single pulse excitation (SPE). In the HE experiment, an echo signal is formed after the second pulse in the HE with a maximum at time $t = 2\tau_{HE}$ after the first 90^o pulse. By varying τ_{HE}, the amplitude of the transverse magnetization, $A(t)$, is measured as a function of time t. All the ^{1}H NMR relaxation experiments in this study were performed at 50^{o}C, well above the T_g value of the gels.

^{1}H NMR Diffusometry. All the ^{1}H NMR diffusometry were carried out in 5 mm NMR tubes on a Bruker DRX 500 MHz spectrometer. The spectrometer was equipped with a diffusion probe head which can impose magnetic field gradients up to 1200 G/cm. The temperature was control by SmartCooler, a variable temperature (VT) gas preconditioning unit. The temperature calibration was done with an ethylene glycol sample, whose two proton chemical shifts are temperature dependent. The pulse sequence used in this study is Hahn echo with 1 ms gradient duration and 20 ms diffusion time.

The self-diffusion coefficient measured by the NMR diffusometry was evaluated by Stejskal-Tanner equation[10],

$$\frac{I(G)}{I(0)} = \exp\left[-G^2\gamma^2\delta^2 D\left(\Delta - \frac{\delta}{3}\right)\right] \tag{5.2}$$

Where $I(G)$ and $I(0)$ are the NMR spin echo intensities with different gradient strength, G the gradient strength, γ the gyromagnetic ratio of the nucleus, δ gradient pulse duration, Δ diffusion time. The self-diffusion coefficient D can be obtained by exponentially fitting of the data using Equation (5.2).

Fluorescence anisotropy measurement[2]: 1mg of Eosin Y powder was dissolved in 1 ml of MilliQ H_2O to prepare a 1 mg/ml Eosin Y water solution, this solution was then diluted to a concentration of 25 μM for the fluorescence anisotropy measurements. A small piece of hydrogel [3 cm × 1 cm (l mm thickness)] was soaked in the Eosin Y solution (25 μM) for 3 hours. All the measurements were carried out using fluorescence spectrometer FluoTime 100 (Picoquant GmBH, Germany). Before the measurement, Eosin Y solution was replaced by MilliQ H_2O to minimize the contribution from unbounded molecules. After the system reached its equilibrium, Eosin Y bounded gel matrix was excited by the pulse laser (λ = 450 nm) and the emission was collected via appropriate filter, and the fluorescence lifetime of molecule (τ) of Eosin Y in the gel matrix was recorded. For anisotropy measurements, the sample was excited by vertically polarized pulse laser and the emission components from the sample was detected in both vertical direction (V) and horizontal direction (H). $K(t,V,V)$ and $K(t,V,H)$ denote fluorescence decay kinetics of the dye (Eosin Y) in gel matrix along the vertical direction and horizontal direction, respectively. These two values were recorded under identical experimental conditions (intensity of the excitation laser, acquisition time, detection efficiency, etc.). Similar measurements were also performed for gel matrices soaked in Eosin Y (25 μM) and $LiClO_4$ (47 mM) mixed solution. The obtained curves from both directions were fit to the anisotropy reconvolution model to calculate the rotational diffusion time (φ) and the exponential reconvolution model to calculate the fluorescence lifetime (τ). FluoFit software from Picoquant GmbH, Germany was used for this fitting procedure. The *G*-factor (the instrument sensitivity ratio towards vertically and horizontally polarized light) were close to 1 for all the measurements and the initial anisotropy were in between 0.2 to 0.3. All the fluorescence measurements and analyses were performed by Dr. Sivaramakrishnan Ramadurai.

[2] Note: The relative dilution of Eoin Y in the fluorescence measurement as compared to the NMR diffusometry is a factor of 1/60.

5.3 RESULTS

Network Structure Analysis. As in the previous studies, to ensure that the expected network structures was formed during the polymerization reactions, ^{13}C solid state NMR spectra and IR spectra were recorded for all the samples, and ^{1}H solution state NMR analysis of the same samples was used for chemical structure characterization of the sol fraction in the network. As shown in **Table 5.1**, the conversion of the double bond for all the samples are near complete, and the cured gels also do not contain product originating from any unwanted side reactions during the curing process.

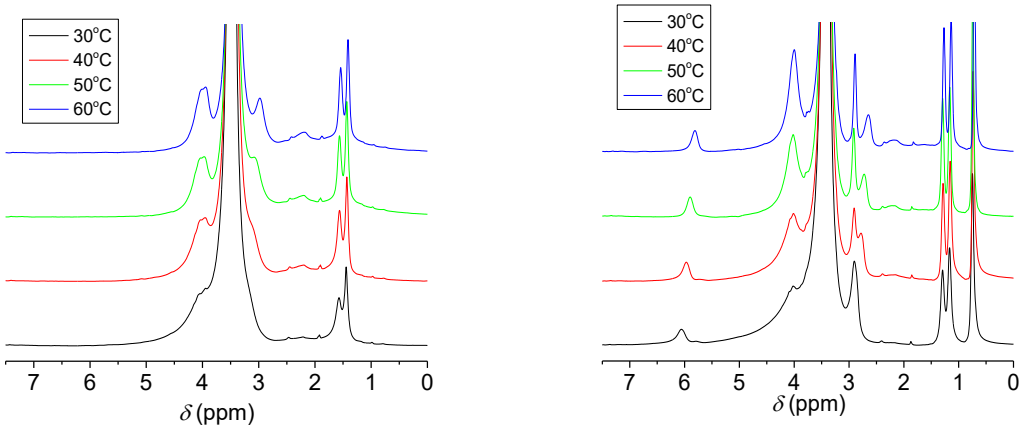

Figure 5.3. SSMAS ^{1}H NMR analyses of samples at different temperatures. (Left to right: PEGDA+HBA. PEGDA+BACOEA).

The temperature dependent gel structure was analyzed using SSMAS NMR, which is sensitive to any structure change in response to the environment change. Due to the relative insensitivity of ^{13}C NMR to the temperature change, ^{1}H NMR is used to analyze the temperature influence on the gel structure as shown in **Figure 5.3**. As been demonstrated in our previous study, the rubbery plateau for all samples was above 60 ºC, hence the terminal repeating PEG unit's δ shifts to high field with increasing PEG chain mobility. However, due to their extremely broad line-shape, the OH chemical shift around 3.09 ppm (for HBA), and the NH chemical shift around 1.82 ppm (for BACOEA) could not be unambiguously analyzed.

Equilibrium Swelling Test. Equilibrium water content for these studied films are reported in **Table 5.1**. Since all the gel formulations are rather similar, the resulted EWC values fall into a similar range with slightly higher water content for H-bonding containing material. The amount of solvent

in the equilibrium swollen network is governed by the molecular weight between crosslinks, the molar volume of the solvent, and the effective Flory χ interaction parameter between the (co)polymer and the solvent.[17] Since the gels are formulated on the similar mass basis of crosslink, the average molecular weight between crosslinks should also be similar, as was demonstrated in Chapter IV. Therefore we expect the water content in this case to be controlled by the effective χ of the copolymer.

^{1}H NMR Relaxometry Analyses. In order to better understand the polymer chain dynamics inside swelling gel matrices, LF NMR relaxometry was used in this study to probe the intermolecular ^{1}H-^{1}H dipolar interactions in the sample. Both T_1 and T_2 were recorded for each sample, by using the fitting procedure described previously, the individual components for gel and drug could be separated, due to the large difference between $T_2(gel)$ and $T_2(drug)$.

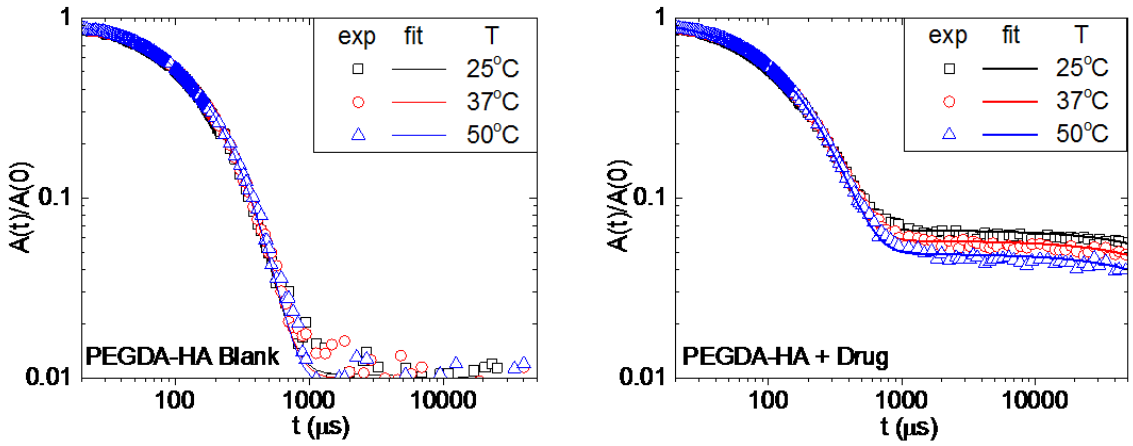

Figure 5.4. Low field ^{1}H NMR relaxometry analysis of sample 1 (PEGDA-HA) swollen in D_2O with and without drug solution.

As shown in **Figure 5.4**, T_2 relaxation profiles for each sample was analyzed at three different temperatures. By swelling the sample in D_2O, no temperature influence in the testing temperature range could be found, hence it is safe to assume that the 'plasticizing' effect[3] of solvent basically lowered the T_g value of the network.[18, 19] The addition of the drug-mimic molecule into the system does not significantly change the polymer dynamics inside the network, as shown by the

[3] The plasticizing effect of solvents in polymeric systems is well documented in literature. Basically, the addition of plasticizer (which is normally a small molecule) into a glassy polymeric system, would decrease the values for T_g and elastic modulus for the blended system, which in turn increase the fluidity/plasticity of the system.

comparison between the relaxation time for the rigid part of networks $T_2(gel)$ (**Table 5.2**), for non-drug-containing and drug-containing samples. Small differences in the rigidity of the swollen network are also apparent from the similar $T_2(gel)$ values.

Sample No.	Composition of Gel Matrix	$T_1(drug)$ (s)	$T_2(drug)$ (s)	$T_2(gel)$ (μs)	
				D_2O	D_2O+Eosin Y
Reference	(Eosin Y in D_2O)	1.10	1.01	-	-
1	HA	0.72	0.30	147.5	141.2
2	HBA	0.25	0.11	135.0	134.7
3	BACOEA	0.78	0.21	158.8	151.2

Table 5.2. $T_1(drug)$, $T_2(drug)$ and $T_2(gel)$ for drug loaded samples analyzed by LF NMR relaxomtery.

As shown in **Table 5.2**, strong restriction on molecular motion imposed by the network on Eosin Y could be observed across all the samples, since both T_1 and T_2 decrease significantly compared to their free-diffusion counterparts. Among them, sample 2 (PEGDA-HBA) has the largest decrease in both relaxation times, which may indicate that this system has the most prominent molecular level interaction between Eosin Y and the network. Meanwhile, for a molecular system which has an isotropic rotational motion, the longitudinal relaxation time (T_1) should have a value close to the transverse relaxation time (T_2), while these two values should be quite different when the system becomes more rigid. Hence, the isotropic rotational motion of the drug in sample 1 and 3, in which there are larger difference between T_1 and T_2, may be largely reduced due to the structural properties in its network as discussed in the previous chapter.

Finally, the fact that there is no difference in the value of $T_2(gel)$ for non-drug-loaded and drug-loaded sample suggest that no chemical reaction occurred during the drug loading procedure which would alter the network dynamics significantly.

^{1}H NMR diffusometry Analyses of Eosin Y. As a way to probe the diffusion coefficient of solute inside the macromolecular matrix, PFG NMR offers great insights about diffusion procedure taking place in the heterogeneous environment.

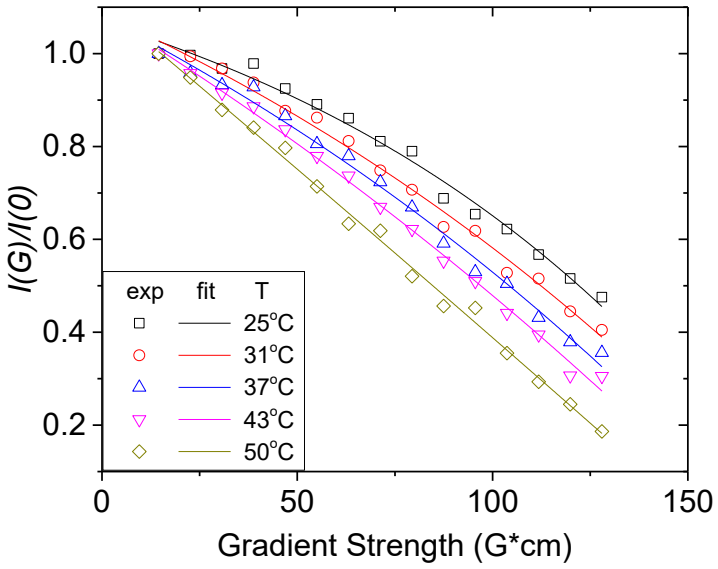

Figure 5.5. PFG NMR diffusion curves of Eosin Y disodium salt in D_2O solution with different temperature.

The temperature dependence of Eosin Y disodium salt's diffusivity was measured in its free state. By comparing to the corresponding D_s(Water) value, the hydrodynamic size of free Eosin Y disodium salt calculated from Stoke-Einstein equation gradually decreases as the temperature increases, which indicates the presence of dimeric/trimeric forms of this drug-mimic in solution. Therefore, the direct implementation of Arrhenius-type analyses as shown in a previous study[14] would be problematic in this instance.

Temperature (°C)	D_s(Eosin Y) (m^2/s)	D_s(Water) (m^2/s)	d_H(Eosin Y) (nm)
25	3.35×10^{-10}	1.80×10^{-9}	0.89
31	4.01×10^{-10}	2.08×10^{-9}	0.85
37	4.68×10^{-10}	2.38×10^{-9}	0.83
43	5.34×10^{-10}	2.68×10^{-9}	0.80
50	6.98×10^{-10}	3.15×10^{-9}	0.72

Table 5.3. Diffusion coefficient of Eosin Y and water in Eosin Y disodium salt D_2O solution (1 mg/ml), and the calculated hydrodynamic size of Eosin Y ($d_H(H_2O)$ = 0.16 nm) at different temperatures. The STD error in this case is *c.*10% for the fitting.

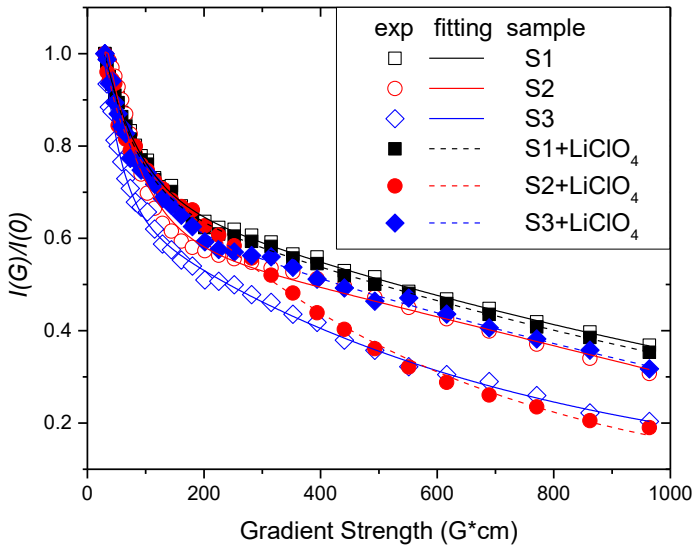

Figure 5.6. PFG NMR diffusion curves of all the samples swollen in Eosin Y disodium salt D_2O solution at 37ºC.

For these reasons, all the PFG NMR measurement on gel samples were carried out at only one temperature (37ºC). As shown in the **Figure 5.6** and **Table 5.4**, for all the hydrogen-bonding containing networks, $D_{EY,2}$ (bounded Eosin Y) has slightly lower values compared to its counterpart in the non-H-bonding-containing gel matrix (PEGDA-HA). However, with the addition of $LiClO_4$, a strong hydrogen bonding disruption agent, this phenomena basically disappeared, and an increase in the value of $D_{EY,2}$ was observed in all the hydrogen-bonding containing materials. A larger increase was found for the sample 2 (PEGDA+HBA), which may indicate stronger H-bonding in this network, This observation is consistent with the results found in NMR relaxometry analyses where larger decrease in T_1 were found for sample 2 (PEGDA-HBA).

Network	$D_{EY,1}$(free) (m^2/s)	Ratio	$D_{EY,2}$(bound) (m^2/s)	Ratio
PEGDA+HA	3.75×10^{-10}	0.36	6.71×10^{-12}	0.64
PEGDA+HA (+ $LiClO_4$)	6.07×10^{-10}	0.34	6.66×10^{-12}	0.66
PEGDA+HBA	3.64×10^{-10}	0.25	3.59×10^{-12}	0.60
PEGDA + HBA (+ $LiClO_4$)	6.12×10^{-10}	0.15	13.0×10^{-12}	0.85
PEGDA+BACOEA	3.55×10^{-10}	0.30	4.16×10^{-12}	0.70
PEGDA + BACOEA (+ $LiClO_4$)	6.06×10^{-10}	0.29	5.45×10^{-12}	0.71

Table 5.4. Diffusion coefficient of Eosin Y in different hydrogel samples at 37ºC. The STD error in this case is *c.*20%.

Fluorescence Spectroscopy Analyses. As one of the most common approaches to analyze the rotational diffusion coefficients of small solutes in large media, fluorescence anisotropy measurements were employed in this study to compare the response of Eosin Y in the three different gel matrices. The information obtained provides details about the local surrounding environment of Eosin Y in the networks, which is anticipated it would help interpret the NMR diffusometry data described in the previous section.

Matrix Gel	Fluorescence Lifetime τ (ns)	Rotational Diffusion time φ (ns)
EosinY solution	1.22 ± 0.01	0.001
PEGDA+HA	3.51 ± 0.11	13.63 ± 0.76
PEGDA+HA (+ $LiClO_4$)	3.61 ± 0.04	12.00 ± 0.80
PEGDA+HBA	3.37 ± 0.12	11.53 ± 0.67
PEGDA+HBA (+ $LiClO_4$)	3.63 ± 0.05	9.20 ± 0.98
PEGDA + BACOEA	3.45 ± 0.05	16.78 ± 2.4
PEGDA + BACOEA (+ $LiClO_4$)	3.48 ± 0.20	12.70 ± 0.77

Table 5.5: Fluorescence lifetime and rotational diffusion time of Eosin Y with and without $LiClO_4$ in different gel matrices. STD: standard deviation estimated from n=2 (n is the number of measurements) .

As expected, the rotational diffusion time (φ) of Eosin Y in solution is fast, and when interacting with different gel matrices, it becomes slower and is significantly different for different gel matrices. On the other hand, the fluorescence lifetime (τ) of Eosin Y also increases 3-fold for all the samples due to these interactions with the networks. However, no significant changes in the τ values were observed for different co-monomers or on addition of the perchlorate H-bonding disruptor. These observations imply that there are other interactions between gel matrices and Eosin Y besides hydrogen bonding which affect the τ value. In the case of sample 1 (PEGDA-HA), the φ value is not significantly different (within experimental error) following the addition of $LiClO_4$. A similar observation was also recorded for fluorescence lifetime, τ, of Eosin Y after adding $LiClO_4$. Since both the fluorescence lifetime and rotational diffusion time of a molecule are very sensitive to the testing environment, and the presence of H-bonding is expected to alter these values. Normally H-bonding-like interactions between dye and gel matrices would be expected to increase φ. In the case of τ, the effect is difficult to predict since H-bonding moves the energies of singlet and triplet excited states, thus affecting the intersystem crossing rate constant with ensuing consequences for fluorescence quantum yield and lifetime. It has been reported as quenching the state[20], which would be the general expectation. However, it may also

extend the lifetime of the excited state[21]. The data shown in Table 5.5 suggest that on adding a H-bond disruptor there is a marginal (at best) increase in τ.

Hence, based on the τ and φ values, it can be concluded that there is no H-bonding-like interaction between Eosin Y and gel matrices for PEGDA-HA. For sample 2 (PEGDA-HBA), after adding $LiClO_4$, a 20% decrease in the φ value was observed. This difference suggests that H-bonding plays a role in the interaction between dye and gel. Meanwhile, Eosin Y has the smallest φ value in sample 2 compared to the other two gel matrices, this indicates that sample 2 has the smallest rotational restriction on Eosin Y. Sample 3 (PEGDA-BACOEA) shows a similar behavior to sample 2, except that its φ value is significantly higher (slower motion) than that of sample 1. Following addition of $LiClO_4$, a 24% decrease in φ was observed. This also indicates the presence of H-bonding. However, given the errors on the measurements and fitting procedure in this case, further discussion about this sample is difficult.

In summary it is highly likely that the dye (Eosin Y) is associated with gel matrices through other interactions besides H-bonding. However, the presence of H-bonding in sample 2 (PEGDA-HBA) and sample 3 (PEGDA-BACOEA) is suggested by the significant changes in φ for Eosin Y in these gel matrices following the addition of $LiClO_4$. The differences in the τ value for Eosin Y between the HBA and BACOEA containing samples, which is clearly significant, may be due to the difference in the structure of these networks, this will be discussed in detail below.

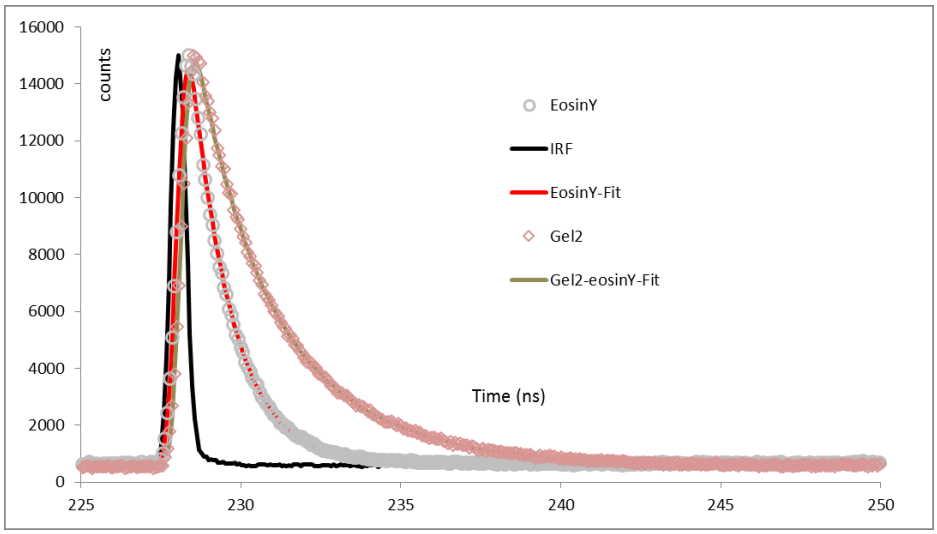

Figure 5.7. Representation of experimental fluorescence lifetime decay curve along with model fit. The black line corresponds to the instrument response function (IRF), the red line to a mono-exponential decay fit of EosinY in solution, the green line is a mono-exponential decay fit of Eosin Y bound to sample 2 gel matrix (PEGDA-HBA).

5.4 DISCUSSION:

Hydrogen bonding effect on average mesh size of the network. As one of parameters critical in describing the nanostructure of a crosslinked hydrogel network, the average network mesh size, ξ plays an important role in determining the solute diffusion coefficient inside the hydrogel matrix[22, 23]. There are several ways to determine ξ, one of which is using the correlation between the hydrogel mesh size and the equilibrium swelling constant to calculate the theoretical value of ξ according to the Flory equation[24]. The average mesh size ξ of a network can be related to the swelling factor (sw) of the sample[24]:

$$\xi = \sqrt{\langle \bar{r}_0^2 \rangle} \sqrt[3]{sw} \tag{5.3}$$

Where $\sqrt{\langle \bar{r}_0^2 \rangle}$ representing the average end-to-end distance of the polymer chains between crosslinks in the absence of swelling water, depends on the number average molecular mass of the chains in the network between crosslinks M_c [24]:

$$\sqrt{\langle \bar{r}_0^2 \rangle} = l \sqrt{2C_n \frac{M_c}{M_r}} \tag{5.4}$$

Where l is the bond length (taken as 1.5 Å), $M_r$the molecular mass of the polymer repeating unit, and C_n the characteristic ratio for PEG (=4.0)[25]. The molecular weight between crosslinks, M_c, was calculated using the Flory equation.[26] This equation was later applied by Lu [27] for evaluation of M_c in PEG based networks:

$$\frac{1}{M_c} = \frac{2}{M_n} - \frac{\left(\frac{\bar{v}}{V_1}\right) \cdot (\ln(1 - v_2) + v_2 + \chi v_2^2)}{v_2^{\frac{1}{3}} - \left(\frac{v_2}{2}\right)} \tag{5.5}$$

Where M_n is the number average molecular weight of the polymer before crosslinking, v_2 the polymer volume fraction in the swollen gel, V_1 the molar volume of the water (18 cm^3/mol), $\bar{v}$ the specific volume of the polymer, and χ the Flory-Huggins polymer-solvent interaction parameter[28]. The calculated values of M_c, $\sqrt{\langle \bar{r}_0^2 \rangle}$, and ξ are given in **Table 5.6**. The calculated average end-to-end distance in this study is not very accurate, since the applicability of the

Equation (5.3) for networks with a small M_c value is questionable due the large deviation of polymer chain behavior from these assumptions made for the calculation[29]. Therefore the value of the mesh size ξ for all the networks used in this study should be taken as an estimate, and only relative comparisons should be made.

Network	M_c (g/mol)	$\sqrt{\langle r_0^2 \rangle}$ (Å)	sw (%)	ξ (Å)
PEGDA + HA	340	11.8	34.8	38.5
PEGDA + HBA	352	12.0	45.1	42.7
PEGDA + BACOEA	349	11.9	42.7	41.7

Table 5.6. The calculated average network mesh size ξ.

As shown in **Table 5.6**, ξ values of the polymeric networks calculated from the equilibrium swelling tests clearly indicate relative larger average mesh sizes in the H-bond containing samples in comparison to the size of the small solute (Eosin Y). However, as mentioned in other study[30], the addition of the copolymer into the system will alter the χ and $\bar{v}$ values, hence, only qualitative comparison between samples can be concluded from this calculation.

Terminal/non-terminal Hydrogen Bond effect on Molecular Diffusion inside Gel Matrices. Two types of networks with different hydrogen bond positions were analyzed in this study. Stronger molecular interactions between the network and the drug-analogue in the network with terminal hydrogen-bond were indicated by NMR relaxometry, NMR diffusometry and fluorescence anisotropy analyses. The distinguishable network behaviors between this two systems might be explained via the accessibility of H-bond group in the network for the drug analogue.

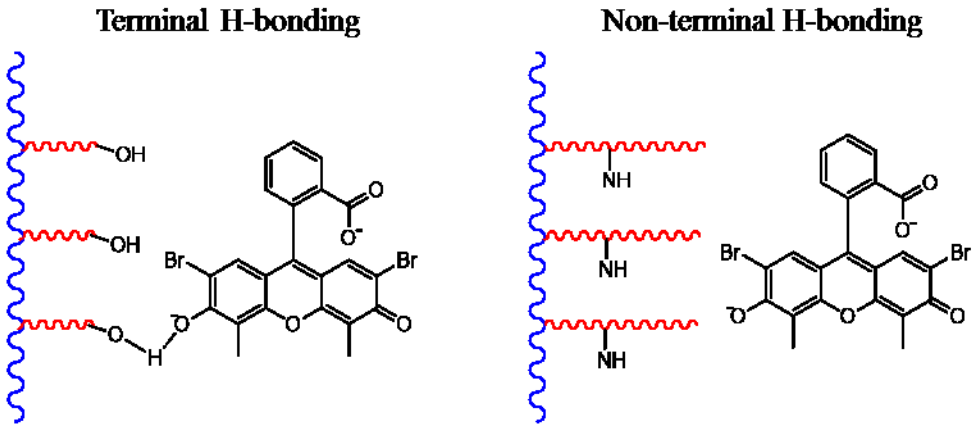

Figure 5.8. The proposed schematic network structures in this study. Left; PEGDA-HBA network, with accessible H-bonding groups. Right; PEGDA-BACOEA network, with non-accessible H-bonding groups.

The mesh size of all the networks (see **Table 5.6**) used in this study should be large enough to allow Eosin Y to freely diffuse. However, due to the rather rigid molecular structure of Eosin Y, the H-bonding interaction between drug mimic and gel networks would depend on the relative distance between them. Since the effective hydrogen bonding length is around 1.7-1.8 Å for OH and NH groups[31, 32], the relatively difficult accessibility of these non-terminal H-bonding group in sample 3 (PEGDA+BACOEA) to Eosin Y molecular, as suggested in **Figure 5.8**, makes the probability of a H-bonding-like interaction between Eosin Y and the gel network in this scenario rather low that in turn renders the H-bonding effect on both network chain dynamics and Eosin Y's diffusivity relatively small. On the other hand, the terminal hydrogen bond group case is free of these geometric hindrances, and can introduce additional restriction on chain mobility in the network, while it also reduces the diffusivities of molecules in the gel matrices by interacting with them as demonstrated in other studies about H-bonding containing materials.[33, 34]

Effect of Network Structure on Molecular Diffusion inside Gel Matrices. As mentioned in the previous chapter, the presence of H-bonding in the network also introduces changes in the network structure by pre-organization of monoacrylate chain during the curing procedure. Compared to the relatively homogeneous distribution of the PEGDA and HA units (or PEGDA and BACOEA units when ω_{BACOEA} is low) for PEGDA-HA gels, the formation of HBA clusters in PEGDA-HBA would be expected to alter the porous structure of the network, and alter the pore size distribution, in a similar fashion to that shown for PEGDA-HEA mentioned in the previous chapter.

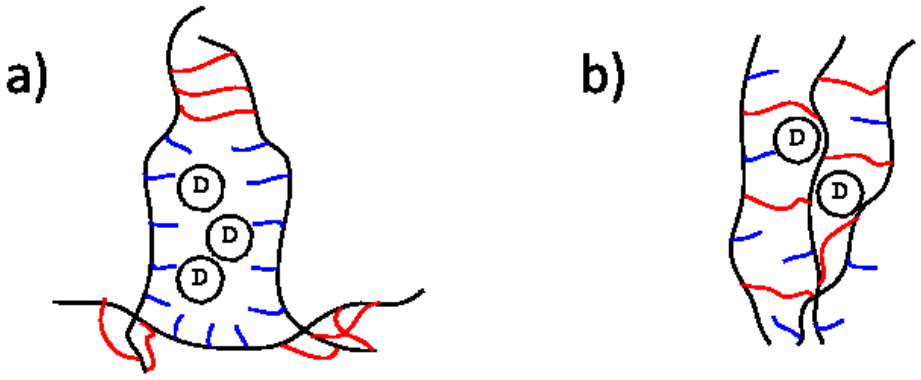

Figure 5.9. The proposed porous structure of the networks in this study (a: PEGDA-HBA; b:PEGDA-HA (or PEGDA-BACOEA), the black circle represents the drug molecule; black line: polyacrylate backbone bond; blue line: monoacrylate; red line: PEGDA.)

As shown schematically in **Figure 5.9**, the separation of densely crosslinked and loosely crosslinked regions increases the possibility of the formation of a network structure with larger mesh size. However, due to the similar molar ratio between crosslinker and monoacrylate, it is unavoidable to simultaneously create regions with smaller mesh size. Therefore, there is no significant difference in the theoretically calculated average mesh size for PEGDA-HBA and PEGDA-BACOEA, only the distribution of the network mesh size would help to illustrate this difference. This interpretation is confirmed by the observations from NMR diffusometry; the introduction of $LiClO_4$, the H-bonding breaker, largely (4-fold) increased $D_{EY,2}$ (translational diffusion coefficient for bounded Eosin Y) in sample 2 (PEGDA-HBA), only moderate increase (20%) was observed for sample 3 (PEGDA-BACOEA). This picture is also broadly consistent with the fluorescence anisotropy analyses.

5.5 CONCLUSIONS:

In this study, three PEGDA-based networks with different copolymers were synthesized by UV-initiated polymerization. These networks were then analyzed by a series of NMR and fluorescence techniques to investigate the H-bonding effect on the small solute diffusion inside the hydrogel networks. A clear hindrance of the solute arising from H-bonding can be found in the PFG NMR analyses of these networks. Besides the obvious interaction between the small solute and the network through H-bonding interactions, different behaviors between networks with terminal hydrogen bonding and ones with non-terminal hydrogen bonding were observed when a H-bonding breaker ($LiClO_4$) was introduced into the networks. This difference was explained from two aspects: the accessibility of H-bond group in the network to the solute and the different network structure caused by the presence of H-bond group during the curing stage (as discussed in Chapter IV). Hence, due to the phenomena mentioned above, we believe it is possible to tailor the drug diffusion process inside hydrogel DDV through the modification of H-bonding. However, the rather complicated effect introduced by H-bonding would require a very careful design of the DDV before any real application.

As mentioned in several studies[5, 35], fluorescence correlation spectroscopy (FCS) as a conventional way to study the diffusion procedure of the small solute in a transparent soft material matrix, could also be utilized in this study to correlated the data generated from NMR in order to give a much more reliable conclusion (this work is currently ongoing). It should also be noted that by varying the diffusion time, Δ, in the PFG NMR analyses, one can also probe the presence of restricted diffusion, since the diffusion coefficient D for small solutes in restricted diffusion is often time-dependent[36].

References:

1. L. T. Fan, S. K. Singh, *Controlled release : a quantitative treatment*. Polymers, properties and applications (Springer-Verlag, Berlin ; New York, 1989), pp. x, 233 p.
2. V. K. Thakur, M. K. Thakur, *Handbook of polymers for pharmaceutical technologies. volume 3. Biodegradable polymers*. pp. online resource.
3. J. Siepmann, R. A. Siegel, M. J. Rathbone, in *Advances in delivery science and technology*. (Springer,, New York, 2012), pp. 1 online resource (xiii, 592 p.).
4. J. Siepmann, F. Siepmann, Modeling of diffusion controlled drug delivery. *J Control Release* **161**, 351 (Jul 20, 2012).
5. S. P. Zustiak, H. Boukari, J. B. Leach, Solute diffusion and interactions in cross-linked poly(ethylene glycol) hydrogels studied by Fluorescence Correlation Spectroscopy. *Soft Matter* **6**, 3609 (2010).
6. S. Koutsopoulos, L. D. Unsworth, Y. Nagai, S. G. Zhang, Controlled release of functional proteins through designer self-assembling peptide nanofiber hydrogel scaffold. *Proceedings of the National Academy of Sciences of the United States of America* **106**, 4623 (Mar 24, 2009).
7. L. C. Dong, A. S. Hoffman, A Novel-Approach for Preparation of Ph-Sensitive Hydrogels for Enteric Drug Delivery. *J Control Release* **15**, 141 (Apr, 1991).
8. J. K. Oh, R. Drumright, D. J. Siegwart, K. Matyjaszewski, The development of microgels/nanogels for drug delivery applications. *Prog Polym Sci* **33**, 448 (Apr, 2008).
9. V. M. Litvinov, Diffusivity of Water Molecules in Amorphous Phase of Nylon-6 Fibers. *Macromolecules* **48**, 4748 (Jul 14, 2015).
10. E. O. Stejskal, J. E. Tanner, Spin Diffusion Measurements: Spin Echoes in the Presence of a Time-Dependent Field Gradient. *J Chem Phys* **42**, 288 (1965).
11. A. Jerschow, N. Muller, Suppression of convection artifacts in stimulated-echo diffusion experiments. Double-stimulated-echo experiments. *J Magn Reson* **125**, 372 (Apr, 1997).
12. G. H. Sorland, D. Aksnes, Artefacts and pitfalls in diffusion measurements by NMR. *Magnetic Resonance in Chemistry* **40**, S139 (Dec, 2002).
13. K. I. Momot, P. W. Kuchel, PFG NMR diffusion experiments for complex systems. *Concept Magn Reson A* **28A**, 249 (Jul, 2006).
14. K. Tomic, W. S. Veeman, M. Boerakker, V. M. Litvinov, A. A. Dias, Lateral and rotational mobility of some drug molecules in a poly(ethylene glycol) diacrylate hydrogel and the effect of drug-cyclodextrin complexation. *Journal of pharmaceutical sciences* **97**, 3245 (Aug, 2008).
15. H. S. Park, J. M. Sung, T. H. Chang, Hydrogen bonding effect on probe diffusion in semidilute polymer solutions: Polymer chain structure dependence. *Macromolecules* **29**, 3216 (Apr 22, 1996).
16. T. Y. Lee, T. M. Roper, E. S. Jonsson, C. A. Guymon, C. E. Hoyle, Influence of hydrogen bonding on photopolymerization rate of hydroxyalkyl acrylates. *Macromolecules* **37**, 3659 (May 18, 2004).
17. P. J. Flory, Statistical Mechanics of Swelling of Network Structures. *J Chem Phys* **18**, 108 (1950).
18. Y. I. Matveev, V. Y. Grinberg, V. B. Tolstoguzov, The plasticizing effect of water on proteins, polysaccharides and their mixtures. Glassy state of biopolymers, food and seeds. *Food Hydrocolloid* **14**, 425 (Sep, 2000).
19. P. Blasi, S. S. D'Souza, F. Selmin, P. P. DeLuca, Plasticizing effect of water on poly(lactide-co-glycolide). *J Control Release* **108**, 1 (Nov 2, 2005).
20. K. Dobek, J. Karolczak, The Influence of Temperature on C153 Steady-State Absorption and Fluorescence Kinetics in Hydrogen Bonding Solvents. *J Fluoresc* **22**, 1647 (Nov, 2012).
21. K.-L. Han, G.-J. Zhao, Wiley InterScience (Online service). (Wiley-Blackwell,, Oxford, 2010), pp. 1 online resource (2 v. (xxiv, C26, 907 p.)).
22. N. A. Peppas, Y. Huang, M. Torres-Lugo, J. H. Ward, J. Zhang, Physicochemical, foundations and structural design of hydrogels in medicine and biology. *Annu Rev Biomed Eng* **2**, 9 (2000).

23. C. C. Lin, A. T. Metters, Hydrogels in controlled release formulations: Network design and mathematical modeling. *Adv Drug Deliver Rev* **58**, 1379 (Nov 30, 2006).
24. T. Canal, N. A. Peppas, Correlation between Mesh Size and Equilibrium Degree of Swelling of Polymeric Networks. *J Biomed Mater Res* **23**, 1183 (Oct, 1989).
25. D. L. Gilbert, T. Okano, T. Miyata, S. W. Kim, Macromolecular Diffusion through Collagen Membranes. *Int J Pharmaceut* **47**, 79 (Nov, 1988).
26. P. J. Flory, *Principles of polymer chemistry*. The George Fisher Baker non-resident lectureship in chemistry at Cornell University (Cornell University Press, Ithaca,, 1953), pp. 672 p.
27. S. X. Lu, K. S. Anseth, Release behavior of high molecular weight solutes from poly(ethylene glycol)-based degradable networks. *Macromolecules* **33**, 2509 (Apr 4, 2000).
28. E. W. Merrill, K. A. Dennison, C. Sung, Partitioning and Diffusion of Solutes in Hydrogels of Poly(Ethylene Oxide). *Biomaterials* **14**, 1117 (Dec, 1993).
29. M. B. Mellott, K. Searcy, M. V. Pishko, Release of protein from highly cross-linked hydrogels of poly(ethylene glycol) diacrylate fabricated by UV polymerization. *Biomaterials* **22**, 929 (May, 2001).
30. D. A. Carr, N. A. Peppas, Molecular Structure of Physiologically-Responsive Hydrogels Controls Diffusive Behavior. *Macromolecular bioscience* **9**, 497 (May 13, 2009).
31. S. J. Grabowski, Hydrogen bonding strength - measures based on geometric and topological parameters. *J Phys Org Chem* **17**, 18 (Jan, 2004).
32. S. J. Grabowski, A new measure of hydrogen bonding strength - ab initio and atoms in molecules studies. *Chem Phys Lett* **338**, 361 (Apr 27, 2001).
33. J. T. Su, P. B. Duncan, A. Momaya, A. Jutila, D. Needham, The effect of hydrogen bonding on the diffusion of water in n-alkanes and n-alcohols measured with a novel single microdroplet method. *J Chem Phys* **132**, (Jan 28, 2010).
34. P. V. Desai, T. J. Raub, M. J. Blanco, How hydrogen bonds impact P-glycoprotein transport and permeability. *Bioorg Med Chem Lett* **22**, 6540 (Nov 1, 2012).
35. T. Lebold, C. Jung, J. Michaelis, C. Brauchle, Nanostructured Silica Materials As Drug-Delivery Systems for Doxorubicin: Single Molecule and Cellular Studies. *Nano Lett* **9**, 2877 (Aug, 2009).
36. G. H. Sørland, *Dynamic pulsed-field-gradient NMR*. Springer Series in Chemical Physics, , pp. 1 online resource (xiii, 354 pages).

Chapter VI

Oxygen Permeability Study of Silicone-based Hydrogels

6.1 Introduction:

Oxygen permeability is an important consideration for contact lens materials because the lens would otherwise act as a barrier to the delivery of oxygen to the avascular tissue of the cornea.

The materials used in contact lenses, reviewed by Nicolson in 2001[1], have evolved to satisfy transport and modulus requirements of lenses. Although initially made from glass in 1936, the first commercially produced lenses were lathed from poly(methyl methacrylate) (PMMA, 0.13 Barrer). Soft hydrogel contact lenses were introduced in the 1970s based on poly(2-hydroxyethyl methacrylate) (HEMA) and other hydrophilic polymers. Although not intrinsically oxygen permeable, these polymers swell with water which gives the material moderate oxygen permeability. Previous studies have shown an exponential relationship between the Dk and water content[2, 3]. Typical HEMA lenses contain 38% water for a Dk around 8 Barrer, while a high-water-content material can achieve around 43 Barrer (78% water).

Hydrogel materials that rely on water for providing oxygen transport are intrinsically limited by the Dk of water at around 80 Barrer [4] and by the practical limitation of the fragility of high-water-content hydrogels. Hence they cannot meet the demand for long-term wear. Materials with higher intrinsic Dk such as siloxane polymers are also used both in rigid and soft designs, but unless made in small diameters would suffer from adhering to the cornea.[1] Furthermore the high mobility of the siloxane made it difficult to permanently modify the surface to make it more wettable and lipophobic [5].

The late 1970's saw the first patents on silicone hydrogels, copolymers of hydrophilic monomers with monomers containing a siloxane group, which in addition to high oxygen permeability featured high enough hydraulic permeability to prevent adhesion. One example silicone moiety is tris-(trimethylsiloxysilyl-) (TRIS), a branched structure (see Figure 6.1), while others are based on linear polydimethylsiloxane (PDMS). Modern silicone hydrogel lenses can achieve Dk's above the upper limit for water, in excess of 100 Barrer.

PDMS owes its high oxygen permeability, of around 600 Barrer [6, 7] to high chain mobility and fast oxygen *diffusivity* (long and wide-angle Si-O bonds lead to a flexible backbone) as evidenced by its T_g of -125ºC [8] being among the lowest of all polymers. Another organosilicon polymer,

poly[1-(trimethylsilyl)-1-propyne] (PTMSP) has a Dk an order of magnitude higher around 6,700 Barrer and a T_g above 250ºC [9] because of its backbone rigidity and massive free volume (*solubility*).

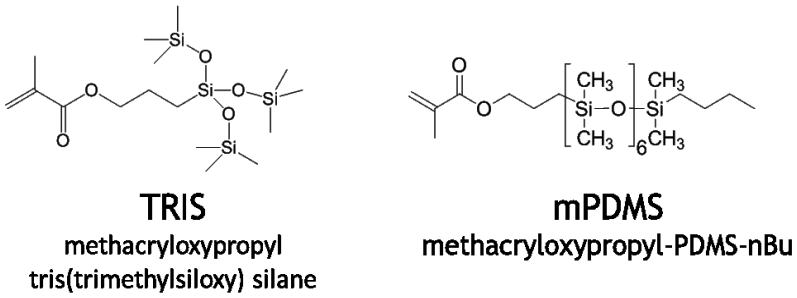

Figure 6.1. Structures of representative silicone monomers. Left: TRIS, a branched siloxane. Right: mPDMS, a linear siloxane.

In order to inform the design of better-performing materials, a mechanistic understanding of oxygen transport through TRIS- and mPDMS-containing silicone hydrogels is required. Performance is sensitive to both the intrinsic properties of the silicone material, as well as to the morphology of the composite material. Differences in morphology can occur due to differences in spatial distribution, but also due to differences in the local environment that might make a monomer behave differently when copolymerized into a network versus that of the pure material.

In this work transient oxygen permeability measurements on model silicone hydrogel materials using a gas-to-gas coulometric method to assess overall differences in diffusivity and permeability are presented. NMR relaxometry was used to gain insight into the mobility of species in the composite with chemical specificity, and to semi-quantitatively compare the relative solubility of oxygen, giving a much more nuanced picture of oxygen transport in these materials. This work is a collaboration with DSM Resolve and DSM Material Science (MSC) Division. Dr. Meredith Wiseman and Dr. Micheal Seitz from DSM MSC performed the O_2 transient measurements and corresponding analyses, and contributed significantly to the discussion.

6.2 Background:

O_2 permeability in hydrogel materials

Gas permeation in amorphous polymers is rather straightforward for small gas penetrants (*e.g.* O_2, N_2). When polymer segmental dynamics are fast, the material can be treated as a liquid solvent and the solubility can be described using Henry's law of solubility,[10]

$$C = k_H p \tag{6.1}$$

where C is the gas concentration in the polymer, k_H is the Henry's law constant, and p is the gas pressure in contact with the polymer.

Assuming all the oxygen on the eye side of the lens is consumed (see **Figure 6.2**), the flux is proportional to the transmissibility Dk/L of the lens under constant partial gas pressure of O_2, with D the diffusion coefficient of oxygen through the lens, k the solubility of oxygen in the lens, and L the lens thickness. Because the thickness of a lens varies with its refractive power, the industry uses the material parameter of oxygen permeability Dk, the product of diffusivity and solubility, typically expressed in units of Barrers [1 Barrer = 10^{-11} (cm^3 O_2) cm cm^{-2} s^{-1} $mmHg^{-1}$].

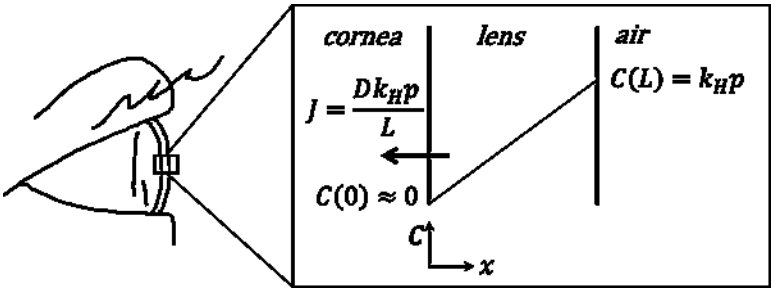

Figure 6.2. Simple treatment of oxygen transport across contact lens of thickness L. The oxygen concentration at the outer edge is the Henry's law solubility constant k_H times the partial pressure of oxygen in the atmosphere p, and zero at the inner edge. The flux through the material is therefore the diffusion coefficient D of oxygen through the lens material times the concentration gradient $k_H p/L$.

In glassy materials, on the other hand, the presence of voids and the possibility of adsorption leads to different dynamics. Several models[11] have been proposed to explain the large deviation in the gas sorption in glassy polymers. Among these, the most successful one is the dual sorption mode model initially proposed by Matthes[12]. In this approach it is assumed that, along with a continuous chain matrix, a polymer consists of so-called microvoids (holes), which are frozen in the matrix.

These discrete microvoids are the reason behind the non-equilibrium thermodynamic state of glassy polymers.[13] Hence, the sorption model for the whole system can be written as a combination between a normal gas sorption mode (Henry's law based) arising from the continuous chain matrix and a Langmuir adsorption mode arising from microvoids, as the following,[14, 15]

$$C = k_H p + \frac{C_L' b p}{1 + b p} \tag{6.2}$$

Where b is the Langmuir affinity parameter and C_L' is the hole saturation constant or Langmuir sorption capacity, which can be further written as,

$$C_L' = \left[\frac{V_g - V_l}{V_g}\right] \rho^* \tag{6.3}$$

where V_g and V_l are the polymer specific volumes in the glassy and hypothetical rubbery states respectively, ρ^* is the molar density of the condensed penetrant.

For a completely mobile system, the Henry form should be valid and Equation (6.2) defines the boundary condition for the situation depicted in **Figure 6.2**. Assuming one-dimensional Fickean diffusion with a constant diffusion coefficient D, at steady-state the concentration profile becomes linear and the flux J through the material is

$$J = \frac{D k_H p}{L} \tag{6.4}$$

Oxygen permeability measurements

The oxygen permeability (Dk) of contact lens materials can be determined by several methods. The most common one is the polarographic method, in which the lens is placed on an electrode at which oxygen passing through the lens is reduced producing a current proportional to the flux. In the coulometric method, oxygen passing through the lens is transferred by a carrier gas to a coulometric sensor. Stokes diaphragm cells have also been used for flat membranes[16]. In the polarographic and coulometric methods, the concentration on one side is known (based on equilibrating with air or oxygen) and the concentration at the other side is assumed to be zero, so the permeability can be simply determined from the flux and sample thickness at steady-state.

All these methods can be adapted to have at least one face of the sample in contact with liquid[17] (water or an electrolyte solution), which helps maintain hydration of a hydrogel sample but which introduces a mass-transfer boundary layer at the sample surface. The overall resistance is therefore the sum of the sample plus the resistance of all boundary layers:

$$\left(\frac{L}{Dk}\right)_{effective} = \left(\frac{L}{Dk}\right)_{sample} + \sum R_{boundary\ layers} \tag{6.5}$$

where the resistance R is the inverse of transmissibility. Since (silicone) hydrogels with higher oxygen transmissibility was developed in the contact lens industry. The design of high-Dk materials which are tough enough to be manufactured into thin lenses has always been the ultimate goal in this field/industry. On the other hand, the thickness of the material is also directly related to the boundary layer resistance of the material which will significantly affect the measured Dk value. This can be corrected by measuring a series of samples with varying thickness in which case the permeability can be determined from the slope as seen in Equation (6.5). Samples can also be stacked to create a series in thickness, although this introduces stagnant layers in between the samples. The boundary layer thickness is sensitive to the flow profile in the chamber and can be reduced by increasing stir speed. If the stirring and chamber geometry are well-controlled, the boundary layer resistance should be the same across measurements and can be successfully accounted for by characterizing it once using a thickness series of high-transmissibility samples and then correcting subsequent measurements accordingly[18].

Transient measurements

Transient measurements can be used to get further information about the diffusion coefficient of oxygen in the sample material. Assuming one-dimensional Fickean diffusion, the concentration $C = f(x,t)$ of oxygen in the sample may be described by

$$\frac{\partial C}{\partial t} = D\frac{\partial^2 c}{\partial x^2} \tag{6.6}$$

with boundary conditions $C(0,t) = kp$, $c(L,t) = 0$ and initial condition $C(x,0) = 0$ which can be solved by separation of variables to derive an expression for the flux at the sample edge:

$$J(L,t) = \frac{Dkp}{L}\left[1 + 2\sum_{n=1}^{\infty}(-1)^n e^{-(n\pi)^2 \frac{t}{L^2/D}}\right] \tag{6.7}$$

Various methods can then be used to fit transient flux measurements to this expression. The simplest is to measure the time at which a defined fraction of the steady-state flux is reached, however this is limited in accuracy [19]. One can fit the expression above directly, but the alternating series converges very slowly at small times which complicates implementation of a fitting algorithm (see Chhabra 2008 for one possible approach[20]). The integral form [21] converges giving a more tractable result, so a common approach is to integrate the signal as follows to define a characteristic time that can be related to the diffusivity:

$$t_c = \int_0^{\infty}\left(1 - \frac{J(L,t)}{J(L,\infty)}\right)dt = \frac{L^2}{6D} \tag{6.8}$$

This method requires the initial time ($t = 0$) to be well-defined.

While the effect of boundary layers on the steady-state measurement is relatively well understood in the field of transient measurements, the influence on the transient behavior is hampered by the non-existence of a simple closed-form solution in the multiple-layer case. Numerical methods can be used but do not yield easily translatable insight into the sensitivity of the response to the presence of various boundary layers. Chhabra et al present an analytical solution for the flux of the same general form as Equation (6.8) with coefficients and eigenvalues dependent on the ratio of diffusional resistance of the combined sample and boundary layer[11] to that of the mass transfer boundary layer. Wichterlová et al. following the method outlined in Linek's work[22], present another equation taking into account the ratio if diffusional resistance ($R = L/Dk$) as well as diffusional capacities ($C = Lk$) [23], which then lead to corrections in the definition of the characteristic time of Equation (6.9). To understand the effect of boundary layer on the characteristic time (t_c), it can expressed in the form

$$\frac{6t_c}{L^2/D} = (1+\alpha)^2 + 3(\beta - \alpha^2)\left(1 - \frac{\frac{2}{3}}{1+\frac{1}{\alpha}}\right) \tag{6.9}$$

where $\alpha = R_{BL}/R_{lens}$ and $\beta = (L^2/D)_{BL}/(L^2/D)_{sample}$. α is the ratio of diffusional resistance of the boundary layer versus the sample and should be minimized by experimental design (high stir speed, thick samples) but will be larger for thin, high-permeability samples such as silicone hydrogel contact lenses. β is the ratio of the diffusion timescales in the boundary layer versus the sample. While this can also be minimized by using thick samples and high stir speed, it also depends on the relative diffusion coefficients in water vs. the sample which will be discussed below.

Diffusivities of commercial contact lens samples from transient measurements in the literature are presented in **Figure 6.3**. The Chhabra dataset[11] accounts for the presence of the boundary layer in computing the diffusivity, while datasets from the group of Compañ [16, 24-26] do not. Instead these authors present an overall effective diffusivity and argue that the resistance of the boundary layer is small as demonstrated by stacking experiments [25, 27]. Literature values for the diffusivity and permeability for oxygen in water and in PDMS rubber are included for referencing.

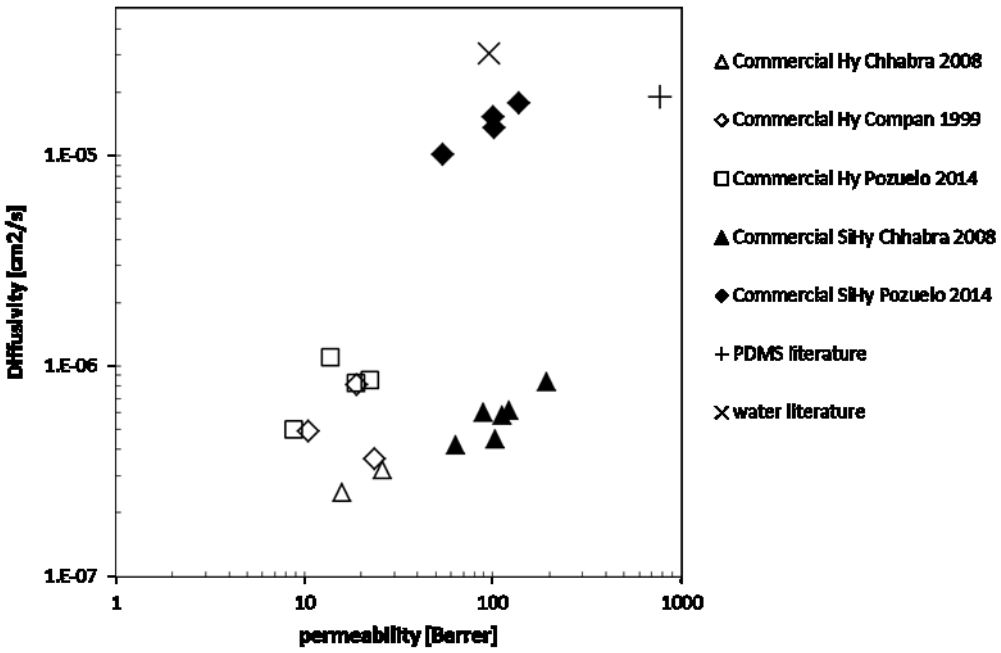

Figure 6.3. Diffusivity of O_2 inside the commercial hydrogels (open symbols) and silicone hydrogel reported in different literature studies.

As is evident from **Figure 6.3**, there is general agreement on the permeability of these materials as consistent with other studies, with silicone hydrogels almost an order of magnitude more oxygen permeable than conventional hydrogels. For diffusivity however, for which the measurement

technique by transient experiments is less well established, the scatter is much larger. All studies report diffusivities for (silicone) hydrogels less than that of pure water. For commercial HEMA based hydrogel (Hy) samples, where the boundary layer effect is expected to be minimal, the three published datasets are consistent in order of magnitude if not in ranking of particular materials. For commercial silicone hydrogel materials, the two available datasets differ by more than an order of magnitude despite containing many of the same products. Additionally perplexing is that the dataset of Pozuelo which does not take boundary resistance into account, shows the larger diffusion coefficient values relative to the dataset of Chhabra which does, contrary to expectation.

Given the lack of consistency in literature studies using transient measurements to determine oxygen diffusivity in liquid setups, alternative methodologies should be considered for gaining insight into these parameters. Pozuelo et al. presented a molecular simulation approach which although remarkably yielded diffusivities in the same order of magnitude as measurements on commercial materials, assumed detailed knowledge of the composition of the (Si)Hy and homogeneity on length-scales larger than that of the simulation. Recent reports on the morphology of model silicone hydrogel materials indicate that this may not be the case with compositional heterogeneity on the length-scale of 10 nm. Compañ et al. have recently used NMR methods to assess oxygen diffusivity and solubility.[28]

Nuclear Magnetic Resonances Relaxometry

Although several techniques (e.g. gravimetric methods) are available to experimentally determine the solubility coefficients of gas in polymer systems, they are not applicable for highly hydrated systems. As an alternative method, the paramagnetic effect of O_2 on the NMR T_1 relaxation rate of hosting molecules has been used as an indicator of the presence of O_2[29]. As demonstrated in a previous study[30], low field NMR T_1 relaxometry analysis, a non-destructive method, can be used to determine the relative difference of the O_2 solubility in polymeric films. In this study we demonstrated that this approach is capable of probing the oxygen solubility in silicone hydrogel materials. By examining T_1 of materials at different temperatures, differences in chain dynamics could also be assessed.

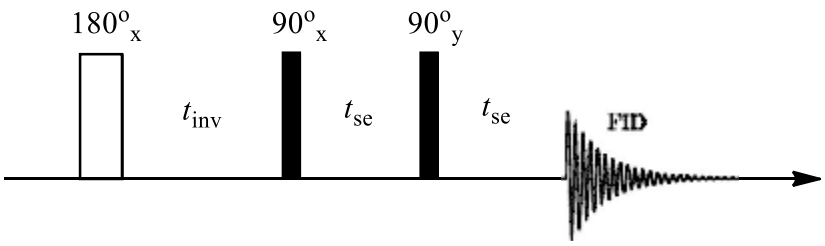

Figure 6.4. Inversion recovery pulse sequence with a solid echo for signal detection. t_{se} was 10 μs.

In this study, the time constant T_1 was determined by fitting the recovery curve measured using the inversion recovery approach (pulse sequence see **Figure 6.4**) with the following exponential function:

$$A(t_{inv}) = A(0)\left[1 - 2e^{-t_{inv}/T_1}\right] \tag{6.10}$$

Every sample was analyzed under two conditions; dry and in its equilibrium-swelling state in H_2O. For the sake of determining the influence of O_2 on the spin-lattice relaxation time of the system, in each case, sample was measured in both dry N_2 and dry air. Due to its paramagnetic nature, the presence of oxygen molecules causes a decrease in the nominal T_1 value for the whole system[31, 32]. Hence, the contribution of oxygen molecules to the nominal T_1, T_1^{Oxygen}, can be determined by using following equation,

$$\frac{1}{T_1^{Oxygen}} = \frac{1}{T_1^{Air}} - \frac{1}{T_1^{Nitrogen}} \tag{6.11}$$

where T_1^{Air} and $T_1^{Nitrogen}$ are measured longitudinal relaxation time of sample under air and nitrogen atmosphere, respectively. This equation is applicable in the case of fast spin-diffusion through the sample volume, slow spin-diffusion in the system would result in a multi-component relaxation decay, which would complicate the interpretation. A single exponential function was used successfully to fit all the recovery curves in this study.

In the case of systems whose O_2 solubility governed by Henry's law (e.g. liquid solution), this method can be used to quantitatively compare O_2 (S_{O_2}) between different systems [33] Hence, the solubility S_{O_2} of Henry's Law governed systems can be quantitatively compared via the following equation:

$$\frac{T_1^{Oxygen}(B)}{T_1^{Oxygen}(A)} = \frac{S_{O_2}(A)}{S_{O_2}(B)} \tag{6.12}$$

However, for systems which have more complicated O_2 solubility model, or for which the effect of polymer chain mobility could no longer be ignored, certain modification should be applied into this proportional relationship since the T_1^{Oxygen} is not only dependent on S_{O_2}.

6.3 Material and Methods:

Materials:

Dimethylacrylamide (DMA), (3-methacryloxypropyl)tris(trimethylsiloxy) silane (TRIS) and the crosslink: Triethylene glycol dimethacrylate (TEGDMA) was purchased from Sigma Aldrich, and Methacryloxypropyl-PDMS-nBu (mPDMS, MW ~ 1500 Da) was purchased from TCI. All materials were used as received

A model series of SiHy were prepared from compositions listed in Table 6.1. TRIS was used as a silicone source at 60 wt% on a dry formulation basis to form TRIS60. A sample containing mPDMS as a silicone source was prepared at an equivalent atomic silicon content on a dry formulation basis, called PDMS54. The crosslink content was held constant in all cases, and the ratio between DMA and silicone monomer was chosen according to the standard formulation used for commercial silicon contact lenses. Formulations were mixed at room temperature until they appeared homogeneous.

Compositions	Sample Names		
	DMA	TRIS60	PDMS54
DMA (wt%)	93.8	33.8	40.2
TRIS silicone monomer (wt%)	-	60.0	-
mPDMS silicone monomer (wt%)	-	-	53.6
TEGDMA (wt%)	5.2	5.2	5.2
Si (wt%)	0	15.9	16.0

Table 6.1. Dry composition of the gel materials used in this study.[1]

Film Preparation

A mold was created using Teflon tubing as a spacer between 2.5mm glass and a polyethylene plate (80×80×3 mm). The mold was held together on three sides by small binder clips, forming a tight seal. Approximately 3 mL of formulation was dispensed into the mold by syringe and immediately cured with a microwave H-bulb curing lamp. During the 5 min curing step, samples heat from

[1] All formulations contained 1 wt% Darocure 1173 as photoinitiator and were mixed with 20 parts of a non-reactive alcohol to 100 parts formulation on weight basis.

room temperature to ~60 °C. The mold is then opened and the Teflon spacer removed. If the mold did not open easily, the PE plate was slightly warmed with a heat gun to ~60°C to allow easy opening. After cure, films were placed in isopropanol/water mixture (1:5) in aluminum trays at least overnight to release the film from the glass and wash out the sol fraction. Films were then transferred to fresh mix solution in plastic cups for another day. Finally, the film is stored in deionized water.

Equilibrium Water Content (EWC)

The equilibrium water content (EWC) at room temperature was determined gravimetrically using

$$EWC = 100 * \frac{(W_{wet} - W_{dry})}{W_{wet}} \tag{6.13}$$

After equilibrating samples in water, pieces were removed, lightly blotted to remove excess surface water and then weighed to determine W_{wet}. The dry mass, W_{dry}, was determined after drying samples under vacuum at 80° C for 6 hours (samples reached a constant mass after this time). Measurements for each sample were performed in at least duplicate and the calculated EWC varied by less than 1%.

Dynamic Mechanical Thermal Analysis (DMTA)

Dynamic-Mechanical Thermal Analysis (DMTA) was used to characterize the temperature-dependent mechanical properties of the dried samples. 5mm x 15mm samples were cut out of the hydrogel films and the thickness measured with a calibrated micrometer. The storage (E') and loss (E'') moduli of dry samples were measured in tension as a function of temperature on a TA DMA Q800 Analyzer at a frequency of 1Hz over a temperature range of -90ºC to at least 150ºC with a heating speed of 3ºC/min.

Oxygen Permeability and Diffusivity

Transient measurements of oxygen flux through hydrogel films were fit to yield the steady-state permeability as well as the diffusivity of oxygen through the material. A gas-to-gas coulometric method was used to record the flux using a Mocon OX-TRAN 2/10 instrument suited to testing highly permeable materials. In this setup a flat hydrogel sample, free of pinholes and of uniform thickness around 700 µm, is equilibrated in water then glued between two aluminum sheets with

a circular opening of 0.28 cm^2. The samples are equilibrated at 34ºC between two tightly-sealed chambers purged with humidified (90% RH) nitrogen gas. Gas flowing through the inner chamber is brought to a coulometric sensor generating an electrical current proportional to the amount of oxygen in the carrier gas. Once all remaining oxygen was purged from the system, the gas in the outer chamber was replaced with humidified oxygen and the flux through the sample was recorded as a function of time. This work was carried out by Dr. Meredith Wiseman and Dr. Micheal Seitz in DSM Material Science Division in Geleen, the Netherlands, all the data fitting and analyses were also performed by them.

^{1}H NMR T_2 Relaxometry

^{1}H NMR relaxation measurements were performed for static samples using a low field Bruker Minispec MQ20 spectrometer with a ^{1}H resonance frequency of 19.65 MHz. Samples were measured at 37ºC in the dry state and after hydration in D_2O. The decay of the transverse magnetization relaxation (T_2 decay) for dried samples was recorded using 90° pulse excitation (SPE). Since the dead time of spectrometer receiver was 9 μs, the signal amplitude was not recorded during this time. The SPE and Hahn-echo pulse sequence were used for recording T_2 decay for swollen samples. The echo time was varied from 70 μs to 400 ms. Data points which were acquired with these two methods, were sequentially combined in the time domain from 90 to 120 ms. All T_2 decays were analyzed using a linear combination of a Gaussian and two exponential functions:

$$A(t) = A(0)^{short} \exp\left[-\left(t/T_2^{short}\right)^2\right] + A(0)^{intermediate} \exp\left[-\left(t/T_2^{intermediate}\right)\right] + A(0)^{long} \exp\left[-\left(t/T_2^{long}\right)\right] \quad (6.14)$$

where indexes 'short', 'intermediate' and 'long' correspond to relaxation component with short, intermediate and long decay time. More detailed discussion of NMR experiments and data analysis were provided previously[34, 35].

^{29}Si Magic Angle Spinning (MAS) Solid State NMR

High-resolution ^{29}Si NMR experiments were performed on Varian Inova NMR spectrometer VNMRS 400 (9.4 T) spectrometer using 6 mm HXY probe head. Poly(dimethylsiloxane) was used as an external reference for ^{29}Si nuclei. ^{29}Si NMR spectra were recorded using direct polarization

Hahn-echo method with different echo times. High power ^{1}H decoupling and magic angle spinning frequency of 2.5 kHz were used. Spectra were recorded at 37ºC for dry samples and those swollen in H_2O.

Low Field ^{1}H NMR T_1 Relaxometry:

Sample Preparation: Samples were dried in the oven under vacuum for 3 days beforehand. After drying, the gel sample was cut into suitable size, and put into a degassed 10 mm NMR tube. The tube was later put under vacuum for 3 hours, and filled with dry N_2 or dry air for 1 hour before measurement.

In the case of the swollen sample, the gel was immersed into DEMI water for 3 days. After it reached its equilibrium swelling state, the sample was cut into suitable size, and put into a degassed 10 mm NMR tube. The dissolved gas in the sample tube was exchanged before measurement by 3 cycles of freezing in liquid nitrogen, placing under vacuum for 10 min, and filling with dry N_2 or dry air.

^1H T_1 Relaxometry Analyses: Low resolution ^{1}H NMR T_1 relaxation experiments were performed on a Bruker Minispec MQ-20 spectrometer on static samples. The operating frequency of this instrument was at 19.65 MHz, ^{1}H resonance. The length of 90º pulse was around 2.8 μs, and the dead time was 9 μs. A BVT-2000 temperature control apparatus was used to regulate the temperature with a deviation no larger than 0.1 ºC. The temperature gradient within the sample volume was less than 1 ºC. The temperature at the sample position was measured separately using a RTD sensor Pt100 with a diameter of 0.2 mm inserted in the middle of the standard sample tube filled with liquid PDMS.

PFG NMR analyses of water self-diffusion in hydrogels:

Sample Preparation: the gels were immersed into DEMI water for 3 days. After it reached its equilibrium swelling state, the sample was cut into suitable size, and put into a degassed 10 mm NMR tube.

PFG NMR analyses: PFG NMR experiments were also carried out on a Bruker Minispec MQ-20 spectrometer on static samples. The z-gradient in the probe was $2.22 T/m$, and Pulsed Field Gradient Stimulated Echo (PFGSTE)[36] approach was used for the measurements. The gradient

pulse width (δ) was 2 *ms*, and the diffusion time was 20 *ms*. During tests, the gradient strength of the probe was increased from 1% to 50% in 40 steps.

All the data points was fitted with Stejskal-Tanner equation[37],

$$\frac{S(TE)}{S_0} = e^{-\gamma^2\delta^2 g^2 D(\Delta-\frac{\delta}{3})} \tag{6.15}$$

where S_0 is the signal intensity without the diffusion weighting, $S(TE)$ is the signal with the gradient, γ is the gyromagnetic ratio, g is the strength of the gradient pulse, D is the diffusion coefficient, δ is the duration of the pulse, Δ is the diffusion time. In the case that there are multiple diffusion components presented in the system, the equation (6.15) should be rewritten as

$$\frac{S(TE)}{S_0} = \sum_{i=1}^{n} A_i e^{-\gamma^2\delta^2 g^2 D_i(\Delta-\frac{\delta}{3})} \tag{6.16}$$

where $\sum_{i=1}^{n} A_i = 1$. Hence, the corresponding diffusion coefficient D_i can be extracted and compared through different networks.

6.4 Results and Discussion:

As mentioned in the ongoing publication[38] by Seitz, significant morphological heterogeneity is present in the Si-based samples, which is the direct result of the clear phase separation between silicon and hydrocarbon domains. Figure 6.5 shows an AFM image of a cryo-microtomed PDMS54 dry sample, in which the variations in phase angle occur on a length scale below 20 nm and appear more globular than elongated. It is expected that the softer domains correspond to areas enriched in silicone. Here, it is necessary to consider the influence of morphological heterogeneity over sample's oxygen permeability during the following analyses.

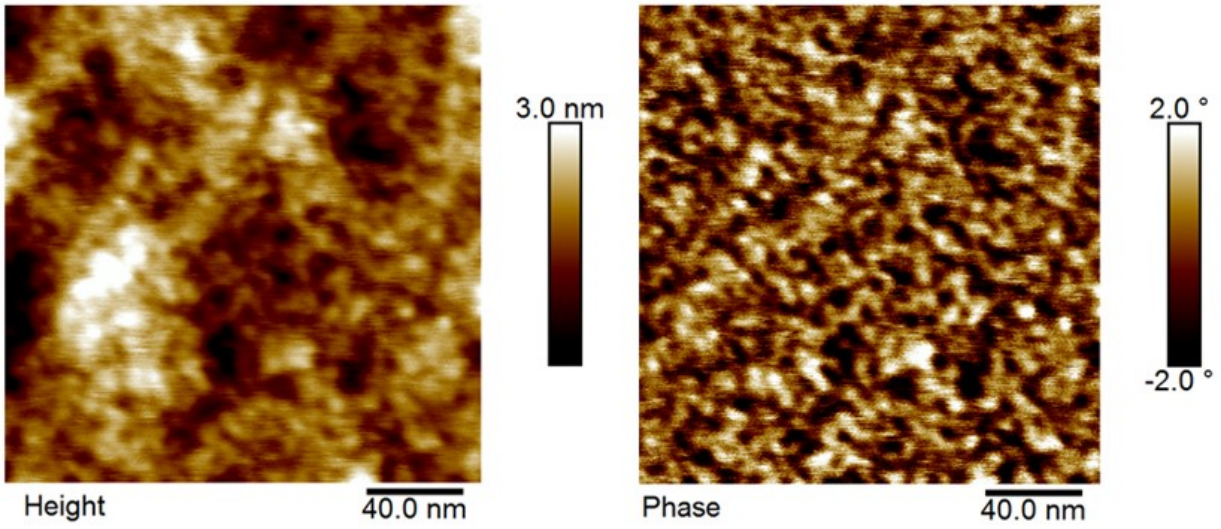

Figure 6.5. Tapping mode AFM phase images of dry PDMS54 sample. Dark regions in the phase images are interpreted to be the softer, silicone-rich domains. (Left: height image; Right: phase image)

Water Equilibrium Swelling Tests

Equilibrium water content values for the films studied are reported in **Table 6.2**. The DMA hydrogel takes up the most water, while the silicone hydrogels' take-up are substantially less. The PDMS54 gel takes up more water than TRIS60.

The equilibrium amount of solvent in a swollen network is governed by the molecular weight between crosslinks, the molar volume of the solvent, and the effective Flory χ interaction parameter between the (co)polymer and the solvent [39]. Since the gels are formulated on the same mass basis of crosslinker, the average molecular weight between crosslinks should be very similar, assuming similar copolymerization kinetics. Therefore we expect the water content in this case to be controlled by the effective χ of the copolymer.

Because the silicone-containing materials in this study were formulated on an equivalent atomic silicon content on a dry formulation basis, the overall mass fraction of TRIS and PDMS is different and so in turn is the amount of DMA added to complete the formulation, with the PDMS54 sample containing slightly more. Because the TRIS and PDMS monomers are similarly apolar and unlikely to contribute groups that enhance water solubility, it is reasonable to ascribe the hydrophilicity contribution to the DMA monomer. Indeed, in these examples the water uptake is proportional to the amount of DMA monomer in the formulation. It is also well known that the morphological heterogeneity also would result in deviation of the EWC values from the prediction of the classical Flory-Rehner theory.[40]

Sample	Si (wt%)	DMA in dry formulation [wt%]	EWC [wt%]
DMA	0	93.8	82.3
TRIS60	15.9	33.8	28.6
PDMS54	16	40.1	36.7

Table 6.2. Equilibrium water content of different samples.

It is important to note that although formulated on an equivalent silicone basis, because TRIS60 and PDMS54 samples swell to different water contents, the silicone content will be slightly different in the swollen materials on a wet basis. Therefore this difference should be taken into account when making any comparisons between the two samples before extrapolating to the intrinsic properties of each silicone monomer.

Dynamic Mechanical Thermal Analysis (DMTA)

As a traditional approach to analyze polymeric materials, DMTA offers insight into T_g of the tested material. Figure 6.6 shows the storage moduli, loss moduli and $Tan\delta$ of all three samples. The corresponding T_g values, extracted from the peak in the loss moduli, are shown in Table 6.3.

DMA sample has the highest T_g around 144.5 ºC, while the TRIS60 sample has a lower T_g (74.2 ºC) compared to the PDMS54 sample (86.2 ºC), this may be due to different chain mobility, as shown in the ^{29}Si NMR and ^{1}H NMR T_2 relaxation analyses, see below.

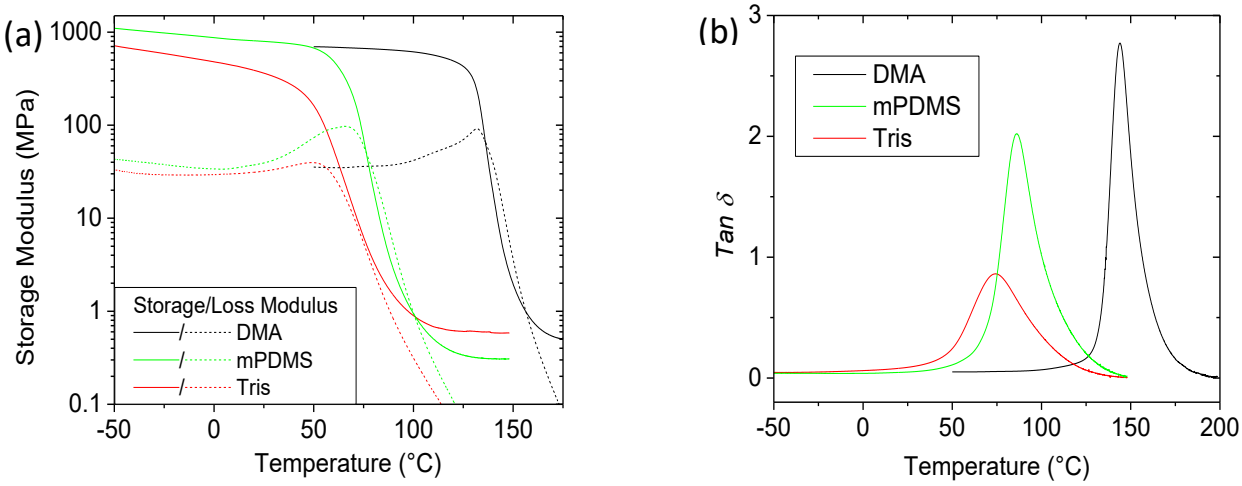

Figure 6.6. (a) Storage moduli and loss moduli of all the dry samples; (b) $Tan\delta$ of corresponding sample.

Sample	T_g/ ºC
DMA	144.5
PDMS54	86.1
TRIS60	74.2

Table 6.3. T_g values for all the samples from DMTA analyses.

Oxygen transport parameters from flux measurements

Transient oxygen flux measurements were used to determine the permeability and diffusivity in the silicone hydrogel samples. The evolution of the flux over time are shown in Figure 6.7. The fitting of the transient data was performed after a non-dimensionalization process, which is routinely used for systems described by differential equations. These data fittings capture the permeation behavior of O_2 in these hydrogels reasonably well.

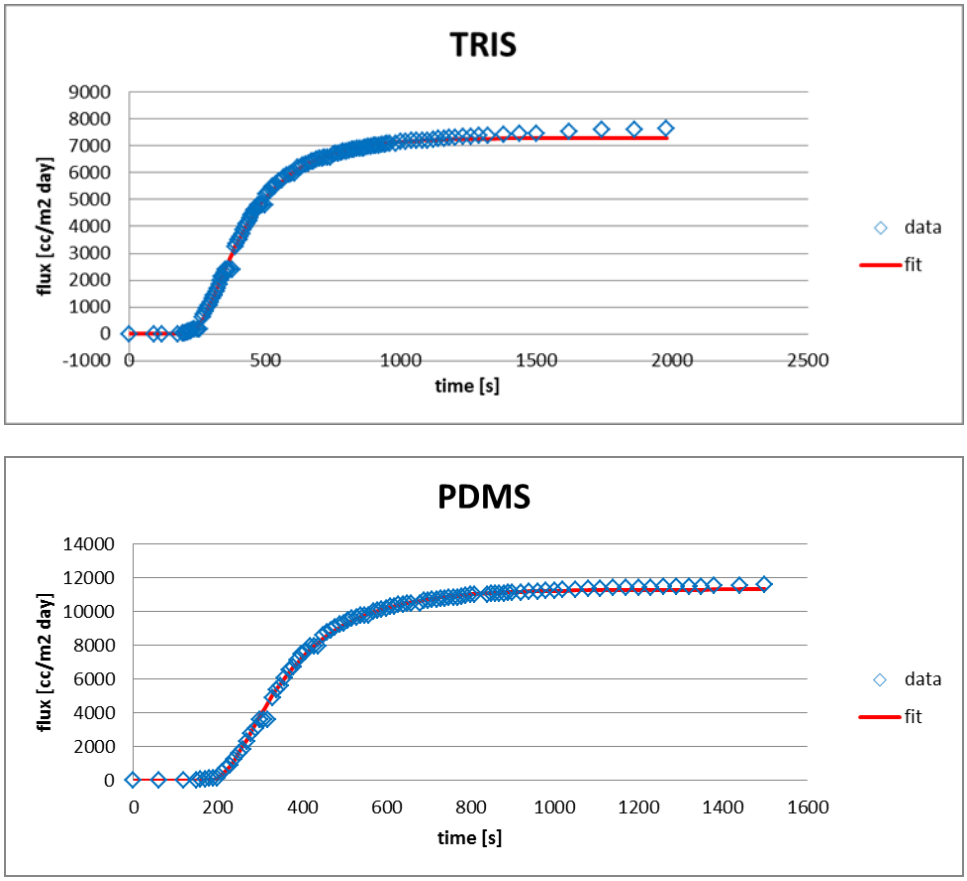

Figure 6.7. Oxygen flux evolution in silicone hydrogels, after the permeant gas was switched from nitrogen to oxygen, at 37°C

Most other studies investigating hydrogel transport properties involve the immersion of samples in liquid water to ensure equilibrium hydration of the sample. However, as discussed earlier, this introduces a stagnant boundary layer at the surface of the sample that complicates analysis of both transient and steady-state measurements. In this work we use a gas-to-gas method which eliminates boundary layers at the expense of possibly dehydrating the samples. Despite using humidified gas, the DMA sample (EWC 82.3%) did not maintain hydration. As the permeability of conventional

hydrogels is very sensitive to their water content, the results for DMA are not presented here. In a separate experiment the relative humidity was varied from 40% to 95% and the permeability of TRIS60 sample was found to be relatively insensitive (data not shown). With actual relative humidity of 91.1% and 95.5% recorded during measurement for the TRIS60 and PDMS54 sample respectively, we anticipate a slight dehydration but only a secondary effect on transport properties.

The oxygen permeability and diffusivity from the model fits are reported in **Table 6.4**. The permeability values are generally of the same order as water, and much higher than hydrogels of the same water content (5-7 Barrer according to the model of #Morgan 1998). The PDMS54 sample had a higher permeability than the TRIS60 sample. Since the PDMS54 sample has a lower silicone content in the hydrated state than the TRIS60, we may attribute this to the better efficiency of mPDMS monomer than TRIS monomer on increasing the oxygen permeability of hydrogels. However, the morphological differences between the two samples may play a role, as suggested by previous similar studies.[41]

Sample	P (Barrer)	D (m^2/s)
TRIS60	75	2.5×10^{-10}
PDMS54	114	2.8×10^{-10}

Table 6.4. oxygen permeability and diffusivity of silicone hydrogel samples

Despite this difference in permeability, the diffusivities measured by this technique for TRIS60 and PDMS54 samples are not very different. This suggests that the better performance of the PDMS54 may be related to solubility or free volume, rather than rate-dependent diffusivity limitations. It is also notable that the diffusivities of the silicone hydrogel samples are an order of magnitude lower than those of both water and pure PDMS, indicating that the transport of oxygen through the composite material is reduced.

NMR diffusometry analyses of H_2O self-diffusivity inside hydrogels

NMR diffusometry is frequently used to probe translational diffusion of small molecules inside certain medium (e.g. porous material, solvent). Through analyzing the water dynamics inside the gel matrices, one can gain information about the polymer chain dynamics in the swollen gel and the role water plays in the O_2 transportation mechanism. It is immediately apparent from Figure 6.8 that there is a significant difference in the diffusion between the two samples, which nominally differ only in the identity of the Si monomer.

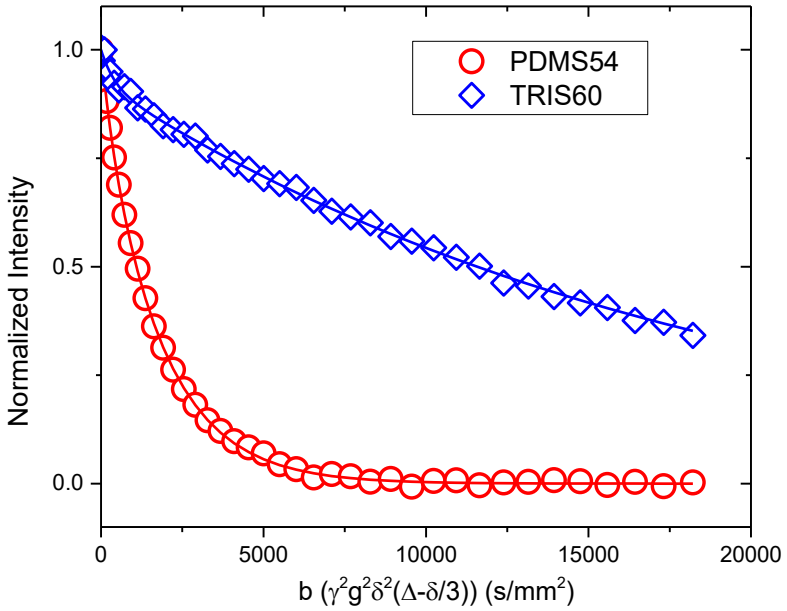

Figure 6.8. PFG-NMR echo attenuation as a function of b ($b = (\gamma g \delta)^2(\Delta - \delta/3)$) for the swollen gels at 37°C.

By fitting the data with the Stejskal-Tanner equation, two diffusion coefficients, for water (D_{H_2O}) assigned to that inside and that on the surface of gel, were extracted. As found in previous studies[42, 43], the water self-diffusion coefficient inside the hydrogel is slower than its free water counterpart ($D_{H_2O}(35℃) = 2.9 \times 10^{-9} m^2 s^{-1}$), due to the interaction with the gel matrix. Note the experimental temperature was 37 ℃ for the current study. As mentioned previously, fast dehydration made it not possible to record reliable data for DMA, hence only diffusion data for PDMS54 and TRIS60 samples are shown in **Table 6.5**. It was found that with increasing water content, the water diffusion rate increases and approaches its free water counterpart. This result is consistent with the

previous observation.[44] It is likely that the mobility of polymer chains and the morphological properties of the gels contribute to this large contrast in D_{H_2O} between the two materials. While the O_2 diffusion in PDMS54 is slightly faster than it in TRIS60 as shown in the previous section, D_{H_2O} in PDMS54 is 10 times higher than in TRIS60. Though these values are more or less of the same magnitude, such a huge difference demonstrates clear differences in the dominant O_2 transport mechanisms for these two gel networks.

Sample	Equilibrium swelling degree (%)	$D_{H_2O,1}$ (m^2/s) (gel water)	Ratio of component 1 (%)	$D_{H_2O,2}$ (m^2/s) (surface water)	Ratio of component 2 (%)
PDMS54	36.74	56.0×10^{-11}	91.1	2.9×10^{-9}	8.9
TRIS60	28.55	5.3×10^{-11}	92.2	2.5×10^{-9}	7.8

Table 6.5. Self-diffusion coefficients of H_2O in different hydrogel at 37°C.

^{1}H NMR T_2 relaxometry

To gain insight into the structure of these materials as it relates to small molecule transport, solid-state ^{1}H NMR T_2 relaxometry was used to probe the mobility of different populations in the samples. The spin-spin relaxation timescale of highly mobile populations is generally long, while rigid, glassy materials relax on a short timescale. An up to three components curve fitting of the transverse magnetization relaxation after a Hahn Echo pulse sequence was used for dry (**Table 6.6**) and hydrated (**Table 6.7**) samples.

Sample	Rigid	Mobile
	T_2^{1H} / μs	T_2^{1H} / μs
	% H atoms	% H atoms
TRIS60	**15**	**78**
	58	42
PDMS54	**20**	**337**
	50	50
DMA	**13**	
	100	

Table 6.6. Relaxation time of each component and its corresponding ratio for every sample in their dry state from the fitting of Hahn Echo experiments.

In the dry state the DMA sample exhibits only one relaxation time which is short and indicative of a glassy material. Upon hydration the ^{1}H nuclei become much more mobile. Two populations of ^{1}H can be distinguished with slightly different relaxation times, possibly related to network heterogeneity and defects such as dangling chain ends[45].

Among the silicone hydrogel samples, multiple T_2 times can be observed even in the dry state. The rigid population (15 - 20 μs) is assigned to a DMA-rich phase based on the similarity in T_2 relaxation time with the DMA sample (13 μs). The longer T_2 population is assigned to a silicone-rich phase as its mobility is higher and it only appears in the silicone-containing samples. The T_2 relaxation of the mobile (silicone) phase is longer for the PDMS54 sample than the TRIS60 sample, indicating the ^{1}H in dry PDMS54 are significantly more mobile than those in TRIS60.

Upon hydration the ^{1}H mobilities generally increase, with the exception of a rigid population (22 μs, 25%) that remains in the TRIS60 sample. This is consistent with the observation in DMTA, in

which the PDMS54 sample is fully rubbery at room temperature while the TRIS60 sample is still undergoing the glass transition. (Data is not shown)

Three populations with different mobilities are observed in the hydrated state for the silicone-containing samples. These cannot be unambiguously assigned to different components of the hydrogel. That said, the times are generally longer for the PDMS54 sample indicating higher mobility. Excluding the sparsely populated highly mobile fraction, the T_2 times of the silicone hydrogels are generally shorter than the conventional hydrogel, indicating that the addition of the silicone co-monomer seems to add constraints, either in the form of phase separation or barriers to chain rotation.

Sample	Rigid	*Rigid domain diameter*	Semi-rigid	Mobile	Highly Mobile	Extremely Mobile
	T_2^{1H} / µs		**T_2^{1H} / µs**	**T_2^{1H} / µs**	**T_2^{1H} / ms**	**T_2^{1H} / ms**
	% H atoms	*[nm]*	% H atoms	% H atoms	% H atoms	% H atoms
TRIS60	**22**	*2.9 ± 0.2*		**117**	**1.9**	
	25			74	1.7	
PDMS54			**74**	**311**		**80**
			40	54		5.9
DMA			**119**	**614**		
			41	59		

Table 6.7. Relaxation time of each component and its corresponding ratio for every samples in their swollen state in D_2O from the fitting of Hahn Echo experiments.

Note that the relaxation times observed here are population averages over the entire sample. Because ^1H are present in the various co-monomers in roughly the same amounts, ^1H NMR does not allow us to directly compare the mobilities of the silicone monomers. For this we rely on ^{29}Si NMR which gives us chemical specificity.

^{29}Si MAS-SSNMR Analyses

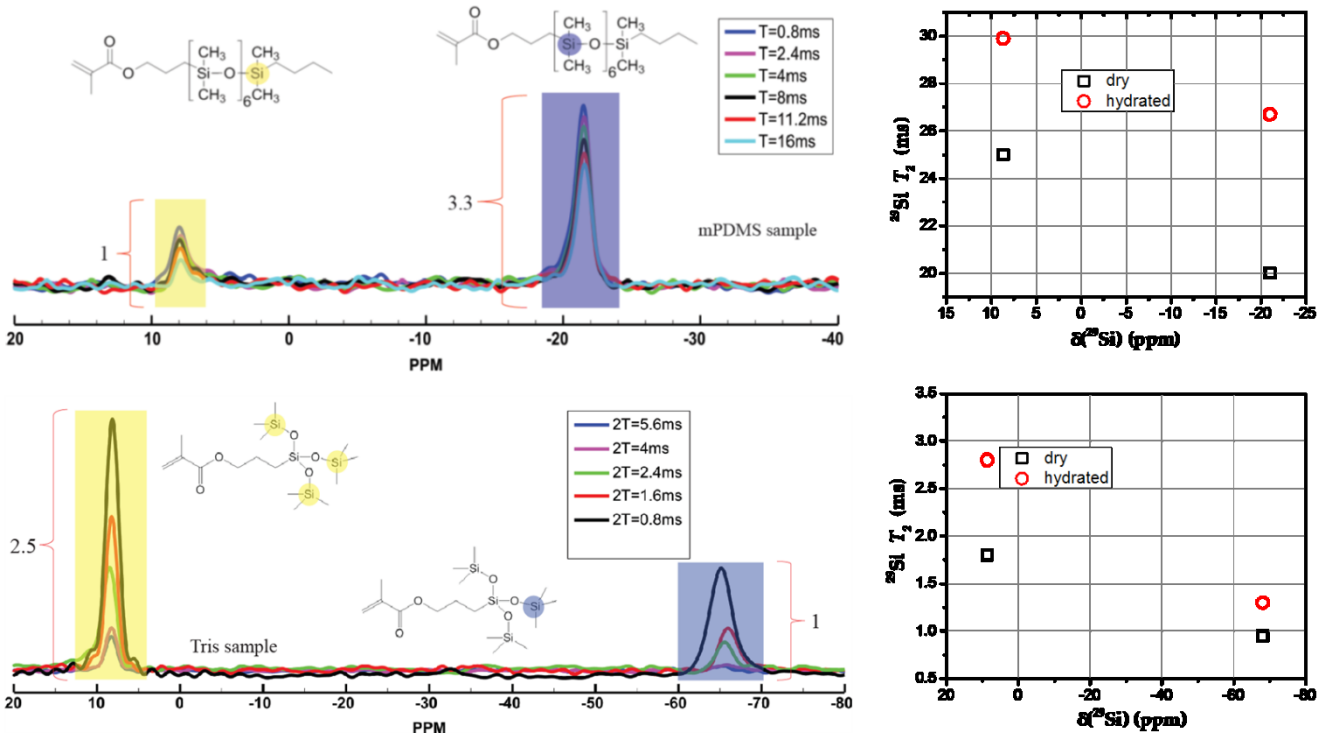

Figure 6.9. (Left) ^{29}Si NMR spectra recorded at magic angle spinning frequency of 2500 Hz. The peaks are clearly assigned and the red numbers besides the peaks indicate relative amounts of various types of Si in the materials. (Right) T_2 relaxation times for the chemically different silicone atoms. Note the different time scales for the PDMS54 and TRIS60 samples.

Solid state NMR is an atomic scale, element-specific probe that is able to identify local coordination environments, usually via the isotropic chemical shift, so it provides a way to directly probe the dynamics of silicone-based polymer chain.(46) Appreciable chemical shift anisotropy (CSA) and relatively small heteronuclear and homonuclear dipolar coupling associated with ^{29}Si nuclei makes it a perfect probe to investigate network structure. The spectral response is extremely sensitive to the chemical and geometrical environment and any small deviation will be manifested in the resonance frequency. The ^{29}Si T_2 relaxation also provides a tool to probe the mobility of Si atoms within the network structure.

From the silicone NMR relaxation experiments, it is clear that the Si in TRIS60 are much less mobile than those in PDMS54 sample which may contribute to the lower *Dk* of the TRIS60 sample. After hydration, the Si mobility increases for all samples although the mobility of the Si in the TRIS60 samples increases the most.

Note that, as argued in several previous publications[47-49], higher torsional mobility of the polymer backbone should result in a larger self-diffusion coefficient of the penetrant. Hence, as also demonstrated in the NMR diffusometry and ^{1}H NMR T_2 relaxometry study, the difference in D_{H_2O} inside the gel system may be caused by the larger mobility of mPDMS chain in comparison to the TRIS compound.

Low Field ^{1}H NMR T_1 relaxometry

As mentioned before, the T_1 relaxation of the network induced by paramagnetic O_2 molecules can be independently separated from other spin relaxation mechanism (e.g. dipolar interaction relaxation). Hence, one can use the difference in T_1 relaxation between systems with and without O_2 to evaluate the O_2 solubility inside the network.

(a) Water (liquid solvent) and linear PDMS (rubbery polymer)

Two reference samples (water and linear PDMS) were tested at room temperature. Since the O_2 solvation mechanism is governed by Henry's law in cases of rubbery PDMS and liquid H_2O, it is possible to compare O_2 solubility between this two systems by examining the contribution of oxygen to the T_1 relaxation time. As shown in Figure 6.10, a clear difference between the T_1 contributions from O_2 in these two media can be observed, indicating that the O_2 solubility in water is significantly lower (T_1 contribution longer) than that in PDMS (approximately 1/10, see Table 6.8). This is in a good agreement with previous studies[50].

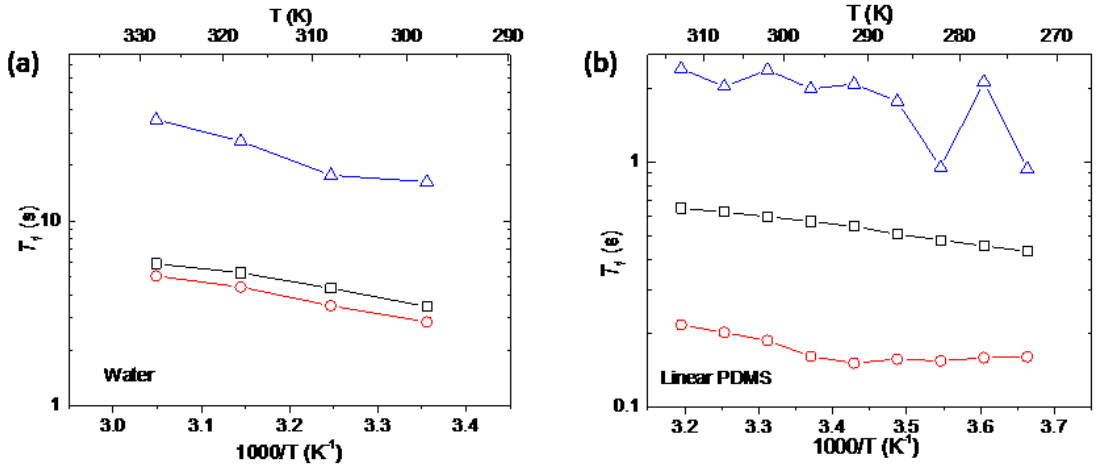

Figure 6.10. Temperature dependence of proton T_1 relaxation time of water (a) and linear PDMS (b) under dry nitrogen (black) and dry air (red). Contribution of paramagnetic oxygen (T_1^{Oxygen}) to T_1 relaxation of films under air is shown by blue points.

For both samples the apparent O_2 contribution to T_1 relaxation time increases with increasing temperature, indicating that the solubility of O_2 decreases. This is consistent with previous studies of O_2 solubility in systems governed by Henry's law at room temperature.[50-55]

Sample	Apparent T_1 contribution of O_2 at 37°C (s)
H_2O	21.4
Linear PDMS	2.4

Table 6.8. Apparent T_1 contribution of O_2 for reference samples at 37°C

(b) Dry (Silicone) Hydrogel Samples

A series of measurements were performed on dry samples. At low temperatures (below T_g of PDMS), all molecular mobility is frozen out of the system and the paramagnetic O_2 contribution should dominate changes in T_1 relaxation. The low temperature analyses (see Figure 6.11) shows a large difference in apparent T_1 contribution from O_2 for Si-based samples (PDMS54 and TRIS60)

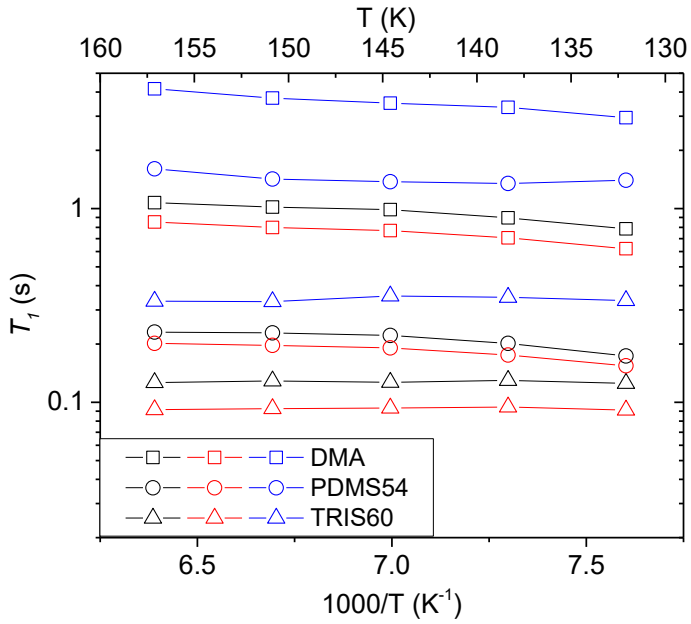

Figure 6.11. Temperature dependence of proton T_1 relaxation time of different dry samples in cryogenic temperature ($T \ll T_g$) under dry nitrogen (black) and dry air (red). Contribution of paramagnetic oxygen (T_1^{Oxygen}) to T_1 relaxation of films under air is shown by blue points.

and conventional crosslinked hydrogel (DMA). At these low temperatures, all components are below T_g (glassy), a dual sorption model should be used to describe solubility instead of Henry's law's form (eqn. 6.2). As mentioned in previous publications[33, 56], in this very low temperature range, the differences in spin-lattice relaxation time which reflect the O_2 solubility inside the network are mainly related to two factors; the excessive specific volume in the network (Langmuir mode), and the Henry's law constant (normal gas sorption mode). Since C_L' in Eqn. (6.3) normally

increases with decreasing temperature before it reaches its constant maximum plateau[57] where $V_g \gg V_l$, the Langmuir mode, which is closely related to the existence of non-equilibrium excess volume in glassy polymers[58], becomes more prominent at lower temperature.

By assuming most of polymer chains are frozen below this temperature and Henry's law constant is similar for O_2 in all the networks, the excessive specific volume in TRIS60 sample can be extracted at approximately 10 times (see Table 6.9) to that of the DMA sample. Hence, more free volume is available in silicon-based hydrogel (PDMS54 and TRIS60) to accommodate O_2 molecules. This is consistent with the previous observations in glassy polymer where the Langmuir mode dominates the O_2 solvation mechanism.

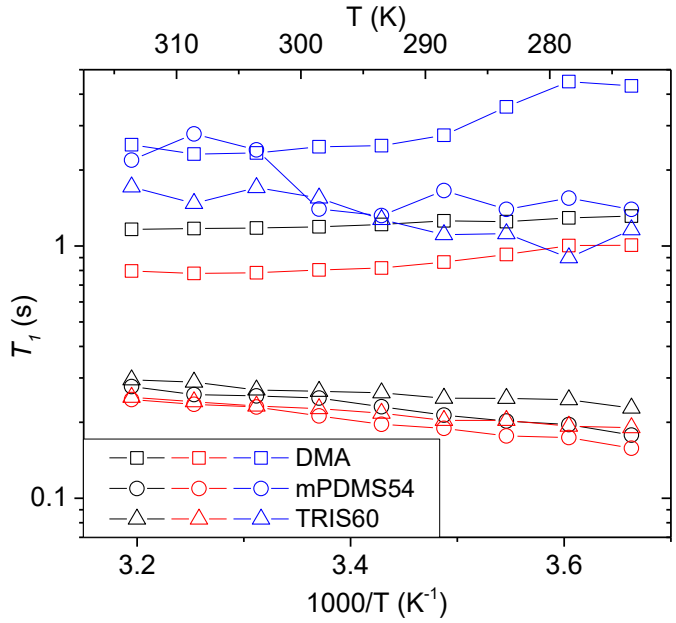

Figure 6.12. Temperature dependence of proton T_1 relaxation time of dry samples around room temperature ($T < T_g$) under dry nitrogen (black) and dry air (red). Contribution of paramagnetic oxygen (T_1^{Oxygen}) to T_1 relaxation of films under air is shown by blue points.

However, the situation is more complicated for glassy polymers at room temperature, since the C_L' value would be reduced significantly upon increasing the temperature to near T_g, leave the Henry mode in this dual modal system cannot be ignored. Meanwhile, for the dry samples at room temperature, although the DMTA results indicate that the copolymer backbones for all the samples are under T_g, silicone side branches are still mobile as indicated by the T_2 relaxation results.

Therefore some domains within the silicone-containing samples are rubbery and the normal gas sorption (Henry mode) into these domain is presumably not negligible. Nevertheless, some information still can be extracted from this test. As shown in Figure 6.12, different temperature dependences can be observed for T_1^{Oxygen} in the room temperature range for different polymers. While the solubility of O_2 decreases with the elevated temperature in TRIS60 and mPDMS54 samples, the opposite occurred for the DMA sample. This could be explained by different sorption enthalpy ΔH_S of O_2 in polyacrylamide- and silicone-based systems. The solubility of a penetrant in a glassy polymer is typically written as van't Hoff relationship[59]:

$$S = S_0 \, exp\left[-\frac{\Delta \, H_s}{RT}\right] \tag{6.17}$$

where S_0 is a constant and $\Delta \, H_s$ is the partial molar enthalpy of sorption , which could be written as following[55],

$$\Delta H_s = \Delta H_{condensation} + \Delta H_{mixing} \tag{6.18}$$

The first term represents the thermodynamic process in which the gaseous penetrant condenses into a phase with large density, while the latter accounts for the formation of a molecular scale gap in the polymer of sufficient size to accommodate the penetrant molecule.[60] Normally, ΔH_s of O_2 gas in hydrocarbon-based systems is slightly larger than zero[61], which results in increasing S_{O_2}, as shown in the case of DMA hydrogel and other hydrocarbon systems[30, 55, 62]. However, the reverse has been reported in the case of the Si-based-hydrogel/O_2 system. As observed previously[53, 54, 60, 63, 64], S_{O_2} in Si-based polymer system decreased slightly upon increasing the temperature. This is consistent with our study, which in turn means ΔH_s of O_2 in these system are negative. Since no special interaction of O_2 in silicone based gel was reported previously, one explanation for it can be that the positive contribution from ΔH_{mixing} of O_2 in the Si-phase of these silicone-based polymer systems is relatively smaller as compared to its hydrocarbon-based counterpart, this results in the sum of these two terms being negative. This means that the formation of spatial gap in silicone based hydrogels is much easier compared to its conventional counterpart.

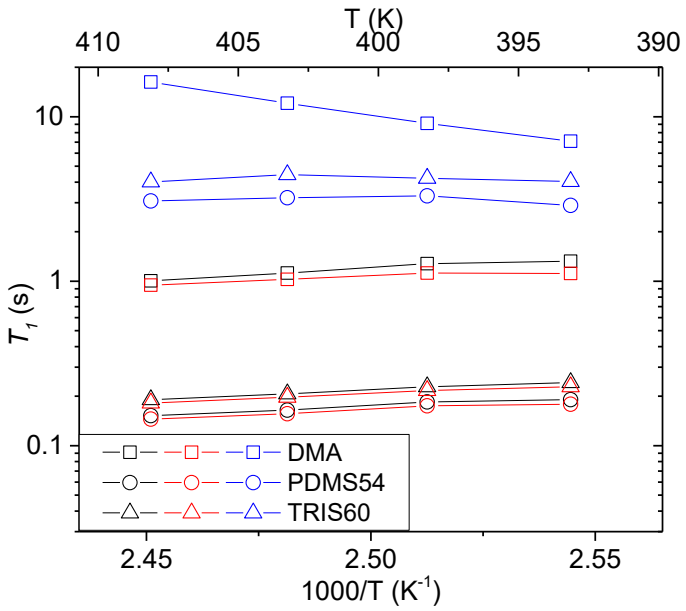

Figure 6.13. Temperature dependence of proton T_1 relaxation time of dry samples in the high temperature range (T around the T_g value of DMA and above T_g values of TRIS60, PDMS54) under dry nitrogen (black) and dry air (red). Contribution of paramagnetic oxygen (T_1^{Oxygen}) to T_1 relaxation of films under air is shown by blue triangle points.

Finally, as shown in Figure 6.13, a significant decrease in O_2 solubility can be observed in DMA and TRIS60 system when the temperature was elevated above its T_g. This decrease is in a good agreement with the prediction of dual sorption mode model[65], since the C_L' in Eqn. (6.3) would equal to zero in the rubbery state, basically eliminating the Langmuir sorption contribution. However, only moderate decreases were observed in PDMS54. The additional Langmuir sorption mode is largely caused by the presence of non-equilibrium excess free volume resulting from the inability of the polymer chains to undergo conformation rearrangement sufficiently rapidly to attain equilibrium. Hence this result suggests that a rather small non-equilibrium excess free volume is present in PDMS54, and polymer chain mobility plays a more important role in determining the O_2 solubility in this case. These data also shows that PDMS54 is more effective than TRIS60 at increasing the oxygen solubility of the hydrogels when only the Henry mode is present. Assuming water acts as a plasticizer and the Henry O_2 solvation mechanism dominates in the swollen system, this result for rubbery samples can be strongly correlated to the transient data on swollen samples, where swollen PDMS54 has a higher O_2 solubility value.

T_1 relaxation also probes local chain mobility although it is not as sensitive as T_2. The slightly longer T_1 relaxation times for dry sample at room temperature for the mPDMS sample compared to the Tris sample means a higher chain mobility in mPDMS at room temperature, this is consistent with the observation in T_2 analyses and ^{29}Si NMR.

Sample	Apparent T_1 contribution of O_2 at -130ºC (s)	Apparent T_1 contribution of O_2 at 37ºC (s)	Apparent T_1 contribution of O_2 at 130ºC (s)
DMA	3.5	2.2	12.1
PDMS54	1.4	2.1	3.2
TRIS60	0.34	1.7	4.4

Table 6.9. Apparent T_1 contribution of O_2 for different dry samples at -130 ºC, 37ºC and 130 ºC.

(c) Hydrated Samples

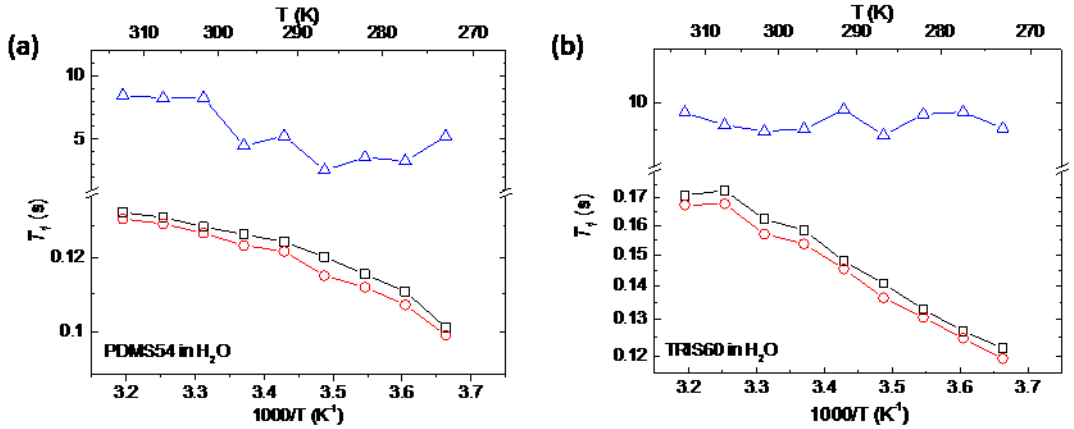

Figure 6.15. Temperature dependence of proton T_1 relaxation time of different swollen samples under dry nitrogen (black) and dry air (red). Contribution of paramagnetic oxygen (T_1^{Oxygen}) to T_1 relaxation of films under air is shown by blue triangle points.

Samples in their equilibrium swelling states were also analyzed using this method. However, due to the extremely large equilibrium swelling degree in DMA sample (82.31%), fast dehydration was unavoidable during the test which rendered the results unreliable. Hence, only the data for the PDMS54 and TRIS60 samples are shown in **Table 6.10**.

Sample	Equilibrium swelling degree (%)	Experimental T_1 contribution of O_2 at 37°C (s)
PDMS54	36.74	7.5
TRIS60	28.55	6.2

Table 6.10. Experimental T_1 contribution of O_2 for different swollen samples at 37°C.

In silicone-based hydrogel, due to the large heterogeneity presented inside the system, the variability of water uptake could be found in different domains. Normally, the hydrophilic part (e.g. DMA based domain) should swell more than the hydrophobic part (e.g. silicon-based domain), so additional specific volume could be created upon swelling, which would increase the O_2 solubility of the material. On the other hand, because of the competition for the adsorbing site between O_2 and H_2O, the number of available adsorbing sites for O_2 should decrease. The overall O_2 solubility in these gels should be determined by the combined effect of the two phenomena. As shown in Table 6.10, hydration causes an overall decrease of O_2 solubility in all the samples, this means the adsorbing site competing mechanism plays a bigger role in determining the overall O_2 solubility in the swollen material compared to the specific volume effect.

The hydrated TRIS sample has a slightly higher S_{O_2} compared to hydrated mPDMS sample, which is inconsistent with the observation in the transient measurements. As mentioned in several previous publication[49], the oxygen solubility in conventional hydrogels correlate with their equilibrium swelling water content, which is not this case for silicone-based hydrogels. As expected, this discrepancy could also be found in our study as TRIS60 has a lower equilibrium swelling degree compared to the PDMS54 sample.

Meanwhile, by comparing the raw T_1 data, the increase of local chain mobility after hydration can be found in both TRIS and mPDMS containing samples, and the former has a larger chain mobility increase. This is consistent with the observation in T_2 analyses and ^{29}Si NMR. On the other hand, the polymer chain mobility of these samples increases upon hydration this may indicate again that water acting as a plasticizer in the hydrogel system when specific condition fulfilled as mentioned in previous studies.[66]

Permeability of O_2 in Silicone-based hydrogel

As pointed out in a previous study [Seitz 2016][38], the rather complicated morphological properties of silicone-based hydrogels mean that the O_2 permeation process involve multiple stages, which renders direct interpretation of the permeability of the material very difficult. Even in the case of traditional polymeric material, the presence of different morphological domains with varied rigidity already has been shown to play a major role on determining the overall diffusivity of small solutes.[67] However, by comparing the macroscopic transient data and the microscopic NMR data, some knowledge could still be extracted from the data about the oxygen permeability inside the organosilicon hydrogel.

a) O_2 Diffusivity

Transient measurements yield a very similar $D_s(O_2)$ for both the PDMS54 and TRIS60 samples. However, a rather large difference in water self-diffusion coefficient $D_s(H_2O)$ between TRIS and mPDMS samples, with PDMS54 possessing a substantially higher one, can be found between these two samples. As mentioned in several previous studies[44, 68], O_2 transport mechanism in hydrogels can be divided into three main processes, diffusion of oxygen in polymer phase ($D_{O_2}(gel)$), diffusion of oxygen in water ($D_{O_2}(water)$) and diffusion of oxygen between the water and polymer phase ($D_{O_2}(InPh)$). Normally, due to the rather fast diffusion of water molecules in gel matrices, $D_{O_2}(water)$ is the determining factor for O_2 diffusivity in gel matrices, as particularly in the case of PDMS54. However, the scenario for TRIS60 is rather different according to all the analyses done so far. The faster-than-water O_2 diffusion in this gel matrix indicates that the $D_{O_2}(gel)$ plays the major role in determining the total O_2 diffusivity rather than $D_{O_2}(water)$. The large increase in $D_{O_2}(gel)$ may involve the so-called diffusion jump phenomenon, in which O_2 molecules jump between nearby silicon domain through the minimum energy path, as illustrated in the work by Seitz in 2016[38] and other works[26, 69].

b) O_2 Solubility

The transient oxygen flux measurement suggests that the PDMS54 has a higher oxygen solubility than the TRIS60. However the T_1 NMR relaxometry data indicates a similar O_2 solubility value, even a slightly higher O_2 solubility was observed for TRIS60. While these findings may appear

contradictory, this discrepancy may arise from different phenomena being probed by these two methods.

The transient measurement relies on accurate determination of the diffusion coefficient of oxygen in the material, which is sensitive to the morphology of the system. As shown in the previous work [38], this can be quite complicated and would rely on realistic spatial modelling, which is far from trivial. In addition to being sensitive to the total amount of silicone-rich versus more water-rich domains, which is logically related to solubility, the rate at which oxygen permeates the material will be sensitive to the connectivity of domains in the material, and the tortuosity or overall path length that the permeant ends up following. While a full analysis is beyond the scope of this work, preliminary SAXS scattering patterns of TRIS- and PDMS- containing hydrogels show different features suggest that at the very least that the morphologies are not equivalent.

NMR relaxometry is sensitive to the molecular level interactions between paramagnetic triplet oxygen and ^{1}H nuclei in the hydrogel systems. Due to differences in intrinsic chain dynamics in these materials in the hydrated state at eye temperature, as seen from T_2 relaxation experiments, direct comparison between these apparent T_1 relaxation contributions and the overall concentration of oxygen is probably not appropriate.

Despite these limitations, some comparisons in terms of solubility can still be made between the two silicone monomers using these techniques. When dry samples are heated above T_g, thus exhibiting only Henry mode of gas sorption, the solubility in the mPDMS containing material is higher than in the TRIS-containing sample, and both of these are higher than pure DMA. Considering the copolymer as a mixture of DMA and silicone monomer, and assuming the DMA behaves similarly in both copolymers, we suggest that PDMS54 has higher intrinsic oxygen solubility than TRIS60. This is counterintuitive on the surface, since TRIS is much more bulky monomer. Hence the reason behind this discrepancy may lay behind the morphological difference (e.g. domain size and distribution) between the two materials, which is the focus of an ongoing study.

6.5 Conclusions:

O_2 permeability in silicone hydrogel was analyzed with a combination of two different techniques; transient measurements analyses and NMR T_1 relaxometry analyses. These results are discussed with other studies on these systems like mechanical tests and NMR T_2 relaxation tests which offer us some information about polymer chain dynamics in the network. It was found that it is difficult to successfully apply these methods in isolation due to the combination of morphological and chain dynamics effects, the application of multiple techniques is shown to lead to a more comprehensive picture of the materials that enables a more fair comparison.

As shown in the previous study[38], phase-separation occurs in silicone-based hydrogels, which complicates physical interpretation of their behavior. The O_2 permeation process in these materials involves multiple stages. Besides the transportation of O_2 in different phases (Si-phase or polymer/water phase), the interfacial O_2 diffusion also complicates the whole analyses. Morphological inhomogeneity and so-called stagnant boundary layer issues render direct use of transient measurement data problematic. However, by implementing complimentary NMR analyses, a better understanding of O_2 solubility inside the inhomogeneous system could be achieved.

NMR T_1 relaxometry analysis is capable of making direct comparison of O_2 solubility in different systems under certain condition (Henry law governing systems), as in the case of water and linear PDMS. Although it is sensitive to polymer chain dynamics, some detailed information, e.g. excessive specific volume of the system, can still be extracted with careful analyses of the data. On the other hand, transient measurement analysis offers direct insight into the O_2 permeability and diffusivity process, though it is also subject to several experimental errors. It is shown here that qualitative comparison between different materials on these issues can still be drawn with careful analyses. The approaches are in some way complementary and may, through careful sample preparation and measurement, yield more detailed insights into O_2 transport, which may lead in time to the design of higher oxygen permeable (Dk/L) materials. Detailed characterization of the morphological heterogeneity in composite silicone hydrogels will also be necessary for such advances.

References

1. P. C. Nicolson, J. Vogt, Soft contact lens polymers: an evolution. *Biomaterials* **22**, 3273 (Dec, 2001).
2. J. E. Rasson, I. Fatt, Oxygen Flux through a Soft Contact-Lens on the Eye. *Am J Optom Phys Opt* **59**, 203 (1982).
3. L. Alvord *et al.*, Oxygen permeability of a new type of high Dk soft contact lens material. *Optometry Vision Sci* **75**, 30 (Jan, 1998).
4. M. Rosenfield, *Optometry science techniques and clinical management*. (Butterworth Heinemann Elsevier, Edinburgh, ed. 2nd, 2009), pp. 555 S.
5. B. Tighe, in *Silicone hydrogels: the rebirth of continuous wear contact lenses,* B. Heinemann, Ed. (Oxford, 2000), pp. 1-21.
6. A. W. Lloyd, R. G. Faragher, S. P. Denyer, Ocular biomaterials and implants. *Biomaterials* **22**, 769 (Apr, 2001).
7. C. T. Laurencin, Y. Khan, *Regenerative engineering*. (Taylor & Francis, Boca Raton, 2013), pp. 417 S.
8. J. C. Lotters, W. Olthuis, P. H. Veltink, P. Bergveld, The mechanical properties of the rubber elastic polymer polydimethylsiloxane for sensor applications. *J Micromech Microeng* **7**, 145 (Sep, 1997).
9. Y. Ichiraku, S. A. Stern, T. Nakagawa, An Investigation of the High Gas-Permeability of Poly (1-Trimethylsilyl-1-Propyne). *J Membrane Sci* **34**, 5 (Nov 1, 1987).
10. J. Crank, *The mathematics of diffusion*. (Clarendon Press, Oxford, Eng, ed. 2d, 1975), pp. viii, 414 p.
11. S. A. Stern, Polymers for Gas Separations - the Next Decade. *J Membrane Sci* **94**, 1 (Sep 19, 1994).
12. V. Stannett, The transport of gases in synthetic polymeric membranes — an historic perspective. *J Membrane Sci* **3**, 97 (1978).
13. W. R. Vieth, *Membrane systems : analysis and design : applications in biotechnology, biomedicine, and polymer science*. (Hanser Publishers ; Distributed in the U.S.A. by Oxford University Press, Munich ; New York, 1988), pp. xv, 360 p.
14. F. G. Kerry, *Industrial gas handbook : gas separation and purification*. (CRC Press, Boca Raton, FL, 2007), pp. 521 p.
15. R. T. Chern, W. J. Koros, E. S. Sanders, S. H. Chen, H. B. Hopfenberg, Implications of the Dual-Mode Sorption and Transport Models for Mixed Gas Permeation. *Acs Sym Ser* **223**, 47 (1983).
16. G. Erdodi, J. P. Kennedy, Water-swollen highly oxygen permeable membranes: Analytical technique and syntheses. *J Polym Sci Pol Chem* **43**, 3491 (Aug 15, 2005).
17. C. F. Morgan, N. A. Brennan, L. Alvord, Comparison of the coulometric and polarographic measurement of a high-Dk hydrogel. *Optometry Vision Sci* **78**, 19 (Jan, 2001).
18. M. Chhabra, J. M. Prausnitz, C. J. Radke, A single-lens polarographic measurement of oxygen permeability (Dk) for hypertransmissible soft contact lenses. *Biomaterials* **28**, 4331 (Oct, 2007).
19. M. C. Kimble, R. E. White, Y. M. Tsou, R. N. Beaver, Estimation of the Diffusion-Coefficient and Solubility for a Gas Diffusing through a Membrane. *J Electrochem Soc* **137**, 2510 (Aug, 1990).
20. M. Chhabra, J. M. Prausnitz, C. J. Radke, Polarographic method for measuring oxygen diffusivity and solubility in water-saturated polymer films: Application to hypertransmissible soft contact lenses. *Ind Eng Chem Res* **47**, 3540 (May 21, 2008).
21. S. Aiba, M. Ohashi, S. Y. Huang, Rapid Determination of Oxygen Permeability of Polymer Membranes. *Ind Eng Chem Fund* **7**, 497 (1968).
22. V. Linek, V. Vacek, J. Sinkule, Check for Consistency of Experimental-Determination of Transient Characteristics of Oxygen Probes with Significant Liquid-Film Resistance. *Biotechnol Bioeng* **25**, 1195 (1983).

23. J. Wichterlova, K. Wichterle, J. Michalek, Determination of permeability and diffusivity of oxygen in polymers by polarographic method with inert gas. *Polymer* **46**, 9974 (Nov 14, 2005).
24. V. Compan, A. Ribes, R. DiazCalleja, E. Riande, Permeability of co-extruded linear low-density polyethylene films to oxygen and carbon dioxide as determined by electrochemical techniques. *Polymer* **37**, 2243 (May, 1996).
25. V. Compan, M. L. Lopez, A. Andrio, A. Lopez-Alemany, M. F. Refojo, Determination of the oxygen transmissibility and permeability of hydrogel contact lenses. *J Appl Polym Sci* **72**, 321 (Apr 18, 1999).
26. J. Pozuelo, V. Compan, J. M. Gonzalez-Meijome, M. Gonzalez, S. Molla, Oxygen and ionic transport in hydrogel and silicone-hydrogel contact lens materials: An experimental and theoretical study. *J Membrane Sci* **452**, 62 (Feb 15, 2014).
27. J. M. Gonzalez-Meijome, V. Compan-Moreno, E. Riande, Determination of oxygen permeability in soft contact lenses using a polarographic method: Estimation of relevant physiological parameters. *Ind Eng Chem Res* **47**, 3619 (May 21, 2008).
28. V. Compan *et al.*, Determination of Oxygen Permeability in Acrylic-Based Hydrogels by Proton NMR Spectroscopy and Imaging. *Macromol Chem Phys* **215**, 624 (Apr, 2014).
29. J. Cavanagh, *Protein NMR spectroscopy : principles and practice*. (Academic Press, Amsterdam ; Boston, ed. 2nd, 2007), pp. xxv, 885 p.
30. V. M. Litvinov, O. Persyn, V. Miri, J. M. Lefebvre, Morphology, Phase Composition, and Molecular Mobility in Polyamide Films in Relation to Oxygen Permeability. *Macromolecules* **43**, 7668 (Sep 28, 2010).
31. Fukushim.E, E. A. Uehling, Nuclear-Spin-Diffusion Relaxation to a Finite Density of Paramagnetic Impurity Ions. *Phys Rev* **173**, 366 (1968).
32. R. Kimmich, A. Peters, K. H. Spohn, Solubility of Oxygen in Lecithin Bilayers and Other Hydrocarbon Lamellae as a Probe for Free-Volume and Transport-Properties. *J Membrane Sci* **9**, 313 (1981).
33. D. Capitani, C. Derosa, A. Ferrando, A. Grassi, A. L. Segre, Polymorphism in Syndiotactic Polystyrene - a H-1-Nmr Relaxation Study. *Macromolecules* **25**, 3874 (Jul 20, 1992).
34. V. M. Litvinov, Strain-induced phenomena in amorphous and semicrystalline elastomers. Solid state H-1 NMR T-2 relaxation under uniaxial compression. *Macromolecules* **34**, 8468 (Nov 20, 2001).
35. V. M. Litvinov, EPDM/PP thermoplastic vulcanizates as studied by proton NMR relaxation: Phase composition, molecular mobility, network structure in the rubbery phase, and network heterogeneity. *Macromolecules* **39**, 8727 (2006).
36. R. M. Cotts, M. J. R. Hoch, T. Sun, J. T. Markert, Pulsed Field Gradient Stimulated Echo Methods for Improved Nmr Diffusion Measurements in Heterogeneous Systems. *J Magn Reson* **83**, 252 (Jun 15, 1989).
37. E. O. Stejskal, J. E. Tanner, Spin Diffusion Measurements: Spin Echoes in the Presence of a Time‐Dependent Field Gradient. *The Journal of Chemical Physics* **42**, 288 (1965).
38. M. E. W. Seitz, M. E.; Hilker, I.; Loos, J.; Tian, M; Goswami, M.; Litvinov, V. M., Morphology of Model Silicone Hydrogels: A multi-pronged approach to characterization. *Private Communication, Artilce in Press*, (2016).
39. P. J. Flory, J. Rehner, Statistical Mechanics of Cross‐Linked Polymer Networks II. Swelling. *The Journal of Chemical Physics* **11**, 521 (1943).
40. T. Hino, J. M. Prausnitz, Swelling equilibria for heterogeneous polyacrylamide gels. *J Appl Polym Sci* **62**, 1635 (Dec 5, 1996).
41. C. Joly, S. Goizet, J. C. Schrotter, J. Sanchez, M. Escoubes, Sol-gel polyimide-silica composite membrane: gas transport properties. *J Membrane Sci* **130**, 63 (Jul 23, 1997).

42. P. Y. Ghi, D. J. T. Hill, A. K. Whittaker, PFG-NMR measurements of the self-diffusion coefficients of water in equilibrium poly(HEMA-co-THFMA) hydrogels. *Biomacromolecules* **3**, 554 (May-Jun, 2002).
43. E. Davies *et al.*, Dynamics of water in agar gels studied using low and high resolution 1H NMR spectroscopy. *Int J Food Sci Tech* **45**, 2502 (Dec, 2010).
44. D. T. Beruto, R. Botter, Role of the water matric potential (Psi(M)) and of equilibrium water content (EWC) on the water self-diffusion coefficient and on the oxygen permeability in hydrogel contact lenses. *Biomaterials* **25**, 2877 (Jun, 2004).
45. V. M. Litvinov, A. A. Dias, Analysis of network structure of UV cured acrylates by H-1 NMR relaxation, C-13 NMR spectroscopy and dynamic mechanical experiments. *Abstr Pap Am Chem S* **221**, U442 (Apr 1, 2001).
46. L. J. Mathias, *Solid state NMR of polymers*. (Plenum Press, New York, 1991), pp. ix, 408 p.
47. T. H. Kim, W. J. Koros, G. R. Husk, K. C. Obrien, Relationship between Gas Separation Properties and Chemical-Structure in a Series of Aromatic Polyimides. *J Membrane Sci* **37**, 45 (Apr, 1988).
48. S. Dumitriu, *Polymeric biomaterials*. (Dekker, New York, 1994), pp. x, 845 p.
49. T. Chirila, *Biomaterials and regenerative medicine in ophthalmology*. Woodhead publishing in materials (CRC Press ;Woodhead, Boca Raton, Oxford, 2010), pp. xi, 540 p.
50. R. Battino, T. R. Rettich, T. Tominaga, The Solubility of Oxygen and Ozone in Liquids. *J Phys Chem Ref Data* **12**, 163 (1983).
51. J. Staudinger, P. V. Roberts, A critical compilation of Henry's law constant temperature dependence relations for organic compounds in dilute aqueous solutions. *Chemosphere* **44**, 561 (Aug, 2001).
52. R. F. Weiss, The solubility of nitrogen, oxygen and argon in water and seawater. *Deep Sea Research and Oceanographic Abstracts* **17**, 721 (1970).
53. J. E. Mark, *Polymer data handbook*. (Oxford University Press, New York, 1999), pp. xi, 1018 p.
54. I. G. Economou, Z. A. Makrodimitri, G. M. Kontogeorgis, A. Tihic, Solubility of gases and solvents in silicon polymers: molecular simulation and equation of state modeling. *Mol Simulat* **33**, 851 (2007).
55. K. F. Ghosal, F., Gas separation using polymer membranes: an overview. *Polym. Adv. Technol.* **5**, 673 (November 1994, 1994).
56. D. Capitani, A. L. Segre, A. Grassi, S. Sykora, Pulsed H-1-Nmr Relaxation in Crystalline Syndiotactic Polystyrene. *Macromolecules* **24**, 623 (Jan 21, 1991).
57. W. J. Koros, D. R. Paul, Observations Concerning the Temperature-Dependence of the Langmuir Sorption Capacity of Glassy-Polymers. *J Polym Sci Pol Phys* **19**, 1655 (1981).
58. H. Hachisuka, Y. Tsujita, A. Takizawa, T. Kinoshita, Co2 Sorption Properties and Enthalpy Relaxation in Alternating Copoly(Vinylidene Cyanide Vinyl Acetate)S. *Polymer* **29**, 2050 (Nov, 1988).
59. L. M. Robeson, W. F. Burgoyne, M. Langsam, A. C. Savoca, C. F. Tien, High-Performance Polymers for Membrane Separation. *Polymer* **35**, 4970 (1994).
60. B. D. Freeman. (Pergamon Press, Oxford ; New York, 1992).
61. N. P. Cheremisinoff, *Handbook of polymer science and technology*. (M. Dekker, New York, 1989), pp. v. <1-4 >.
62. R. Paterson *et al.*, IUPAC-NIST solubility data series 70. Solubility of gases in glassy polymers. *J Phys Chem Ref Data* **28**, 1255 (Sep-Oct, 1999).
63. G. Allen, J. C. Bevington, *Comprehensive polymer science : the synthesis, characterization, reactions & applications of polymers*. (Pergamon Press, Oxford, England ; New York, ed. 1st, 1989).
64. M. E. Cox, B. Dunn, Oxygen Diffusion in Poly(Dimethyl Siloxane) Using Fluorescence Quenching .1. Measurement Technique and Analysis. *J Polym Sci Pol Chem* **24**, 621 (Apr, 1986).

65. W. J. Koros, R. T. Chern, V. Stannett, H. B. Hopfenberg, A Model for Permeation of Mixed Gases and Vapors in Glassy-Polymers. *J Polym Sci Pol Phys* **19**, 1513 (1981).
66. D. Capitani, V. Crescenzi, A. A. De Angelis, A. L. Segre, Water in hydrogels. An NMR study of water/polymer interactions in weakly cross-linked chitosan networks. *Macromolecules* **34**, 4136 (Jun 5, 2001).
67. V. M. Litvinov, Diffusivity of Water Molecules in Amorphous Phase of Nylon-6 Fibers. *Macromolecules* **48**, 4748 (Jul 14, 2015).
68. S. A. M. Vanstroebiezen, F. M. Everaerts, L. J. J. Janssen, R. A. Tacken, Diffusion-Coefficients of Oxygen, Hydrogen-Peroxide and Glucose in a Hydrogel. *Anal Chim Acta* **273**, 553 (Feb 15, 1993).
69. V. Compan *et al.*, A potentiostatic study of oxygen transport through poly (2-ethoxyethyl methacrylate-co-2,3-dihydroxypropylmethacrylate) hydrogel membranes. *Biomaterials* **26**, 3783 (Jun, 2005).

Summary

A series of polyacrylate/polyamide hydrogels were analyzed by a combination of NMR, thermal, mechanical and optical characterization techniques. The chemical structure and polymer chain dynamic information of these hydrogels were correlated with their macroscopic mechanical and thermal properties. Several important factors in designing hydrogel were studied throughout this thesis. The corresponding conclusions of these studies can be summarized as following,

1. Topological constraints have significant impact on polymer dynamics in the network, as demonstrated by different polymer chain behavior between networks with zip-like junction topology and the one with point-like junction topology. Therefore, the "short-chain-abnormality" in crosslink density calculation of polyacrylate network should be taken into account when designing new hydrogels. Some correction to the classical rubber elasticity theory should be introduced in order to prevent the overestimation of the chain mobility.
2. Hydrogen bonding induced preorganization indeed occurs during the UV curing procedure as shown by the clustering of hydrogen bonding containing of monoacrylate in the copolymer network. However, the type of hydrogen bonding would largely affect the clustering formation in these networks.
3. Diffusion of small solute in networks containing hydrogen bonding is large reduced due to the interaction between hydrogen bonding and the small solute. While hydrogen bonding induced network structure change also plays an important role in determining the small solute's translational and rotational diffusion inside the network.
4. Silicone based hydrogel possesses great O_2 permeability. This is normally attributed to the extremely large excessive specific volume of this type of hydrogels. Unlike conventional mechanic transient measurements, NMR is capable of directly probing the O_2 solubility inside the network. These observation of O_2 solubility is in a good agreement with large excessive specific volume of these Silicone based hydrogel. On the other hand, the morphological heterogeneity also plays an important role on transporting O_2 through the gel material.